

**A PETROGRAPHIC AND GEOCHRONOLOGICAL
ASSESSMENT OF THE AILERON METAMORPHICS,
MOUNT BOOTHBY AREA, CENTRAL AUSTRALIA.**

Mark Eastlake, BSc (University of Newcastle)

Presented to the Department of Earth and Planetary Sciences,
Division of Environmental and Life Sciences,
in Partial Fulfilment of the Requirements for the Degree of:

Honours, BSc

Macquarie University, Sydney

June, 2013

**MACQUARIE
UNIVERSITY**



STATEMENT OF ORIGINALITY

All the work submitted in this thesis is the original work of the author except where otherwise acknowledged. No part of this thesis has previously been submitted to any other university or institution.

Signed – Mark Andrew Saywell Eastlake

Dated

ACKNOWLEDGMENTS

I would like to begin by acknowledging staff of the School of Environmental and Life Sciences at the University of Newcastle who nurtured my interests in geology during my undergraduate study there. In particular Silvia Frisia, Greg Hancock, Bill Landenberger, and Glen Phillips are greatly thanked for their enthusiasm for teaching geology, and their support and understanding.

I am grateful to my primary supervisor Nathan Daczko for giving me the opportunity to study some fascinating Australian geology. His enthusiasm and energy has been a constant source of motivation during the study. I consider myself fortunate to have been able to study under such a knowledgeable and generous person.

Norm Pearson is thanked for regularly affording me his time to discuss various aspects of geochronology and his advice on evaluating geochemical data. Geoffrey Clarke, Sandra Piazzolo and Bruce Schaefer are thanked for their supervision during fieldwork. Sarah Fitzjohn is thanked for her assistance and companionship during field work. A special mention goes to Dale and Maria who always made sure we were well fed during fieldwork.

Staff at the Geochemical Analysis Unit (GAU), Macquarie University, are acknowledge for their assistance at various stages of the study. The following people are specifically thanked for their individual contributions to the research:

- Manal Bebbington – preparation of polished thin-sections
- Steve Craven – assistance during zircon separation and grain mount preparation
- Kevin Grant – assistance with SEM imaging
- Yoann Gréau – assistance with Hf-isotope data acquisition
- Will Powell – assistance with U–Pb data acquisition

Finally, I wish to thank my family, both immediate and extended, for their complete support throughout my Honours year.

ABSTRACT

The Aileron Metamorphics form kilometre-scale enclaves of granulite facies metasedimentary rock in voluminous megacrystic granitoid (Boothby Orthogneiss) in the SE Reynolds Range, Arunta Region, central Australia. Early tectono-stratigraphic reconstructions of the Arunta Region isolated the Aileron Metamorphics from the regional stratigraphy on the basis of metamorphic grade and post-depositional history. A revised chrono-stratigraphic framework of the Arunta Region permits correlation of the Aileron Metamorphics with regional sedimentary packages (Lander or Reynolds packages).

U-Pb geochronology of detrital zircon limits sediment deposition to after 1846 Ma. Sillimanite-cordierite assemblages indicate granulite facies conditions prevailed during foliation development accompanying N-S directed shortening that produced moderately (39°) east plunging, tight folds (D1) in the Aileron Metamorphics prior to granitoid emplacement. Magmatic zircon growth during crystallisation of the Boothby Orthogneiss protolith is dated at 1801 ± 8 Ma, coeval with the Stafford Event (1810–1800 Ma), although limiting factors on this age are discussed. Hf-isotope values indicate significant contributions of recycled crust to local magma production, and equate Hf-isotope signatures of Stafford Event granitoids in the adjacent Anmatjira Range. The intrusive relationship of the Boothby Orthogneiss with the Aileron Metamorphics determines the Aileron Metamorphics are high-grade Lander Package equivalents. Subsequent NNE–SSW oriented deformation (D2) produced WNW–ESE striking upright folds that plunge 43° to the east in paragneiss and a penetrative gneissosity in orthogneiss. D3 structures are associated with NNE–SSW striking shear bands and crenulations that overprint D1 and D2 structures.

A static sillimanite overprint of D1–D3 microstructures accompanied partial melting in both igneous and sedimentary protoliths. Two populations of low-Th/U rim domains on detrital protolith zircon separated from post-D3 diatexite record HT metamorphism during the 1590–1560 Ma Chewings Orogeny. A late period of metamorphic zircon growth is recorded at 1531 ± 3 Ma by a population of highly concordant low-Th/U rim domains, which suggest the current duration of the Chewings Orogeny in the SE Reynolds Range requires revision.

Palaeozoic reactivation of the area during the Alice Springs Orogeny (450–300 Ma) produced shallowly (16°) west plunging open folds and steeply dipping east-west striking high-strain shear zones characterised by Bt+Qz±Mus±Ky±Rt (upper greenschist–amphibolite facies) assemblages. Kinematic indicators determine a reverse sense of movement along these structures that overprint earlier high-grade fabrics in both igneous and sedimentary protoliths.

TABLE OF CONTENTS

Acknowledgments	iii
Abstract	iv
Table of Contents	v
List of Figures	viii
List of Tables	x
List of Acronyms	xi

CHAPTER 1: INTRODUCTION & REGIONAL GEOLOGY **1**

1.1	Introduction	1
1.2	Regional Geology of the Arunta Region	1
1.3	Local Geology of the Reynolds Range	3
1.3.1	Lander Package (1865–1820 Ma)	3
1.3.2	Stafford Event (1810–1800 Ma)	4
1.3.3	Reynolds Package (<i>ca.</i> 1780 Ma)	4
1.3.4	Yambah Event (1780–1770 Ma)	5
1.3.5	Chewings Orogeny (1590–1560 Ma)	5
1.3.6	Alice Springs Orogeny (450–300 Ma)	6
1.3.7	High-grade Metasedimentary Units	7
1.4	Project Aims & Objectives	8

CHAPTER 2: FIELDWORK & MAPPING **9**

2.1	Overview	9
2.2	Study Area	9
2.3	Fieldwork & Mapping	10

CHAPTER 3: STRUCTURAL GEOLOGY **16**

3.1	Introduction	16
3.2	Early Axial Planar Foliation (D1)	16
3.3	Dominant Gneissosity & Folding (D2)	16
3.4	NE Striking Shear Bands & Crenulations (D3)	20
3.5	Retrograde Shear Zones (D4)	23
3.6	Discussion	26

CHAPTER 4: PETROGRAPHY	29
4.1 Introduction	29
4.2 Methods	29
4.3 Metasedimentary Protoliths	30
4.3.1 Paragneiss	30
4.3.2 Calc-silicate Rocks	37
4.3.3 Quartz-mica Schists—D4 Shear Zones	40
4.4 Metaigneous Protoliths	44
4.4.1 Felsic Orthogneiss	44
4.4.2 Mafic Orthogneiss	47
4.4.3 Mesomylonite—D4 Mylonite Shear Zones	47
4.5 Discussion	50
 CHAPTER 5: LA-ICPMS U–Pb ZIRCON GEOCHRONOLOGY	 51
5.1 Introduction	51
5.1.1 Sample Description	52
5.2 Methods	53
5.3 Zircon Morphology	57
5.3.1 Quartzite	57
5.3.2 Boothby Orthogneiss	57
5.3.3 Diatexite	60
5.4 U–Pb Zircon Geochronology	62
5.4.1 Quartzite	62
5.4.2 Boothby Orthogneiss	70
5.4.3 Diatexite	79
5.5 Discussion	85
 CHAPTER 6: LA-MC-ICPMS ZIRCON Hf ISOTOPE ANALYSIS	 90
6.1 Introduction	90
6.2 Methods	90
6.3 Zircon Hf-Isotope Analysis	93
6.3.1 Quartzite	93
6.3.2 Boothby Orthogneiss	96
6.3.3 Diatexite	99
6.4 Discussion	104

CHAPTER 7: DISCUSSION & CONCLUSION **106**

7.1	Timing Relationships & Fabric Development	106
7.2	Maximum Age of Sediment Deposition & Correlations	107
7.3	Granitoid Emplacement	107
7.4	Timing of Metamorphism	107
7.5	Conclusions	108

CHAPTER 8: LIMITATIONS & FURTHER RESEARCH **110**

REFERENCES **111****APPENDICES (DIGITAL)**

Appendix 1	Catalogue of collected Samples and Prepared Thin-sections
Appendix 2	Structural Measurements
Appendix 3	U–Pb Geochronology Data
Appendix 4	Hf-isotope Analysis Data

LIST OF FIGURES

FIGURE	DESCRIPTION	PAGE
Figure 1.1	Generalised geological map of the Reynolds–Anmatjira Ranges	2
Figure 2.1	Field area landscape	8
Figure 2.2	Generalised geology of the study area near Mount Boothby	10
Figure 2.3	Inter-bedded pelitic and psammitic paragneiss outcrop	11
Figure 2.4	Diatexite outcrop in paragneiss	11
Figure 2.5	Quartzo-feldspathic sillimanite-rich paragneiss outcrop	12
Figure 2.6	Calc-silicate gneiss outcrop	13
Figure 2.7	Boothby Orthogneiss outcrop	14
Figure 3.1	S1 fabric developed axial planner to F1 fold in paragneiss	18
Figure 3.2	Stereographic analysis: D1 structural measurements	18
Figure 3.3	F2 refolding S0/S1 foliation with D3 overprint in paragneiss	19
Figure 3.4	Stereographic analysis: D2 structural measurements	19
Figure 3.5	Pervasive S2 gneissosity in Boothby Orthogneiss	20
Figure 3.6	F3 crenulation of S0/S1 foliation in paragneiss	21
Figure 3.7	Stereographic analysis: D3 structural measurements	21
Figure 3.8	F3 crenulation of S0/S1 foliation in paragneiss	22
Figure 3.9	D3 shear band overprinting S2 gneissosity in Boothby Orthogneiss	23
Figure 3.10	D4 high-strain shear zone in paragneiss	24
Figure 3.11	D4 high-strain mylonite zone in Boothby Orthogneiss	25
Figure 3.12	Stereographic analysis: D4 structural measurements	26
Figure 4.1	Photomicrograph: Poikiloblastic cordierite and F3 crenulation of sillimanite in metapelitic paragneiss (MB001)	31
Figure 4.2	Photomicrograph: Recrystallised aggregate of polygonal cordierite and K-feldspar neosome in metapelitic paragneiss (MB024)	32
Figure 4.3	Photomicrograph: F2 microfold in metapsammitic paragneiss	34
Figure 4.4	Photomicrograph: Seriate aggregate of interlobate quartz grains in quartzite (MB003)	35
Figure 4.5	Photomicrograph: Aligned sillimanite clusters in seriate K-feldspar-quartz-phlogopite matrix (MB002)	36
Figure 4.6	Photomicrograph: Tremolite-bearing diopside-plagioclase calc-silicate gneiss (MB009)	38
Figure 4.7	Photomicrograph: Forsterite olivine pseudomorphed by serpentine in a calcite-spinel matrix (MB010)	39
Figure 4.8	Photomicrograph: Micaceous schist (MB037, MB038)	42

Figure 4.9	Photomicrograph: Micaceous schist (MB043, MB048)	43
Figure 4.10	Photomicrograph: K-feldspar augen orthogneiss (Boothby Orthogneiss; MB007)	45
Figure 4.11	Photomicrograph: Sillimanite replacement of biotite in tourmaline-bearing plagioclase-K-feldspar-biotite orthogneiss (MB036)	46
Figure 4.12	Photomicrograph: granoblastic aggregate of plagioclase in plagioclase-hornblende-orthopyroxene-biotite gneiss (MB035)	48
Figure 4.13	Photomicrograph: σ -type asymmetric strain shadows developed on K-feldspar porphyroclasts in mylonitic foliation (MB004)	49
Figure 5.1	Representative zircon CL images: Quartzite (MB003)	58
Figure 5.2	Representative zircon CL images: Boothby Orthogneiss (MB007)	59
Figure 5.3	Representative zircon CL images: Diatexite (MB033)	61
Figure 5.4	Quartzite (MB003): Concordia diagram (Wetherill and Tera-Wasserburg) and Probability Density Distribution	64
Figure 5.5	Quartzite (MB003): Th vs U and Th/U ratio vs Age (Ma)	65
Figure 5.6	Quartzite (MB003): Mean age-youngest coherent group	66
Figure 5.7	Quartzite (MB003): Comparison of Lander and Reynolds package distributions	68
Figure 5.8	Boothby Orthogneiss (MB007): Concordia diagram (Wetherill and Tera-Wasserburg) and Probability Density Distribution	71
Figure 5.9	Boothby Orthogneiss (MB007): Th vs U and Th/U ratio vs Age (Ma)	72
Figure 5.10	Boothby Orthogneiss (MB007): Mean age- ≤ 1873 Ma	74
Figure 5.11	Boothby Orthogneiss (MB007): Mixture modelling- ≤ 1873 Ma	75
Figure 5.12	Boothby Orthogneiss (MB007): Mean age- ≤ 1846 Ma	76
Figure 5.13	Boothby Orthogneiss (MB007): Mixture modelling- ≤ 1846 Ma	78
Figure 5.14	Diatexite (MB033): Concordia diagram (Wetherill and Tera-Wasserburg) and Probability Density Distribution	81
Figure 5.15	Diatexite (MB033): Th/U ratio vs Age (Ma)	82
Figure 5.16	Diatexite (MB033): Concordia regressions	83
Figure 6.1	Quartzite (MB003): Hf-isotope analysis (Hf_i and ϵHf)	93
Figure 6.2	Quartzite (MB003): $^{176}(\text{Lu}, \text{Yb})/^{177}\text{Hf}$ ratio vs Age (Ma)	94
Figure 6.3	Boothby Orthogneiss (MB007): Hf-isotope analysis (Hf_i and ϵHf)	96
Figure 6.4	Boothby Orthogneiss (MB007): $^{176}(\text{Lu}, \text{Yb})/^{177}\text{Hf}$ ratio vs Age (Ma)	97
Figure 6.5	Diatexite (MB033): Hf-isotope analysis (Hf_i and ϵHf)	99
Figure 6.6	Diatexite (MB033): $^{176}(\text{Lu}, \text{Yb})/^{177}\text{Hf}$ ratio vs Age (Ma)	101

LIST OF TABLES

TABLE	DESCRIPTION	PAGE
Table 3.1	Summary of mapped tectonic fabrics and correlation with regional structures	27
Table 5.1	Frantz settings used during magnetic barrier separation of zircon grains	53
Table 5.2	Operating conditions and data acquisition parameters used during U-Pb analysis by LA-ICPMS	55
Table 5.3	Observed values for external-calibration and reference materials during U-Pb analysis by LA-ICPMS.	56
Table 5.4	Zircon size distribution: Quartzite (MB003)	57
Table 5.5	Zircon size distribution: Boothby Orthogneiss (MB007)	59
Table 5.6	Zircon size distribution: Diatexite (MB033)	60
Table 5.7	Summary of weighted average age calculations: Quartzite (MB003)	63
Table 5.8	Summary of weighted average age calculations: Boothby Orthogneiss (MB007)— ≤ 1874 Ma cut-off	73
Table 5.9	Summary of mixture modelling of hybrid dataset— ≤ 1874 Ma cut-off	74
Table 5.10	Summary of weighted average age calculations: Boothby Orthogneiss (MB007)—ages ≤ 1846 Ma	77
Table 5.11	Summary of mixture modelling of hybrid dataset— ≤ 1846 Ma cut-off	77
Table 6.2	Operating conditions and data acquisition parameters used during Hf-isotope analysis by LA-MC-ICPMS	90
Table 6.3	Observed values for reference materials during Hf-isotope analysis by LA-MC-ICPMS.	90

LIST OF ACRONYMS

ACRONYM	DESCRIPTION
<i>ca.</i>	Circa
CHUR	CHondrite Unfractionated Reservoir
CL	Cathodoluminescence
DM	Depleted Mantle
KDE	Kernel Density Estimate
LA-ICPMS	Laser Ablation Inductively Coupled Plasma Mass Spectrometry
LA-MC-ICPMS	Laser Ablation Multi Collector Inductively Coupled Plasma Mass Spectrometry
MSWD	Mean Square of Weighted Deviates
PDD	Probability Density Distribution
PDF	Probability Density Function
PDP	Probability Density Plot
SEM	Scanning Electron Microscope

1. INTRODUCTION & REGIONAL GEOLOGY

1.1 INTRODUCTION

Continental development commonly involves reworking of orogenic belts. This is particularly the case for Archaean and Proterozoic regions, which have had a substantial part of Earth history in which to accumulate the effects of multiple tectonic events (e.g. Hand & Buick, 2001). The processes involved in orogenic reworking involve both mechanical and thermal mechanisms, which are manifested in the structural, metamorphic and magmatic character of metamorphic terrains (Collins & Vernon, 1991; Hand & Buick, 2001).

Palaeoproterozoic basement rocks exposed in the Arunta Region of central Australia represent a region known to have experienced multiple orogenic events (Dirks & Wilson, 1990; Collins & Vernon, 1991; Dirks *et al.*, 1991; Collins & Shaw, 1995; Collins & Williams, 1995; Vry *et al.*, 1996; Williams *et al.*, 1996; Cartwright *et al.*, 1999; Hand & Buick, 2001; Scrimgeour *et al.*, 2005). However, the spatial and temporal extent of each orogenic event and interplay between existing structures and subsequent orogeny require further investigation.

The Arunta Region experienced at least four orogenic events. The major tectonic elements of the region formed during Paleoproterozoic orogenesis; these are termed the Stafford Event (*ca.* 1810–1800 Ma), Yambah Event (*ca.* 1780–1770 Ma) and Chewings Orogeny (*ca.* 1590–1560 Ma). Palaeozoic reactivation of the region occurred during the Alice Springs Orogeny (*ca.* 450–300 Ma). The distribution and geochronology of rocks of varied protolith and metamorphic grade were selected for analysis in the SE Reynolds–Anmatjira ranges approximately 130 km north of Alice Springs (Figure 1.1).

1.2 REGIONAL GEOLOGY OF THE ARUNTA REGION

The Arunta Region forms a *ca.* 200 000 km² exposure of Proterozoic to early Palaeozoic basement rocks extending across the southern portion of the Northern Territory in central Australia (Claoué-Long & Edgoose, 2008; Figure 1.1). The approximately E–W trending terrane is unconformably overlain by a system of Neoproterozoic to mid-Palaeozoic intra-cratonic sedimentary basins that form relics of the Centralian Superbasin, which once covered much of Proterozoic Australia (Walter *et al.*, 1995; Hand & Buick, 2001).

A revised subdivision of the Arunta has recently been proposed by Scrimgeour (2004) to replace the deteriorating geological framework established by earlier workers (Shaw *et al.*, 1984; Stewart *et al.*, 1984). To aid the reader's independent investigation, reference is made to earlier definitions where appropriate given their persistence in the literature. The Arunta Region is divided into three, largely fault-bounded, provinces with distinct protolith ages and subsequent tectono-metamorphic

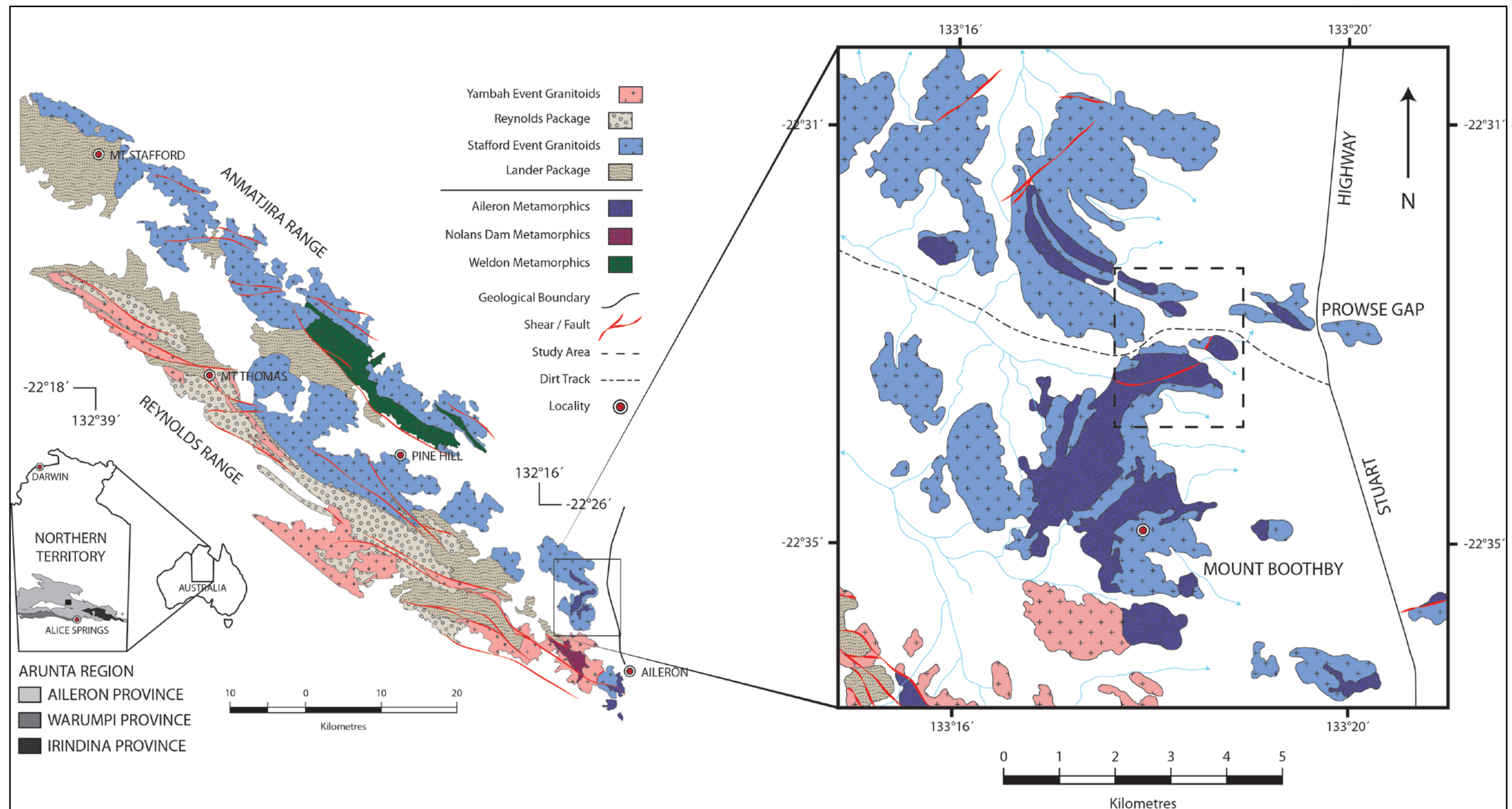


Figure 1.1 Generalised geology of the Reynolds–Anmatjira ranges. Large-scale detail to the right shows local geology of the Mount Boothby area (modified after Stewart, 1981; Buick *et al.*, 1999).

evolutions (Scrimgeour, 2004; Scrimgeour *et al.*, 2005; Figure 1.1). The oldest and most aurally extensive of these, the Aileron Province, includes much of the northern and central tectonic zones of Shaw *et al.* (1984). Sedimentary and igneous rocks of this province have depositional and intrusive ages largely restricted to the period 1870–1710 Ma, similar to other Palaeoproterozoic basement terranes of the North Australian Craton including the Tennant and Tanami regions to the north and northwest respectively (Scrimgeour *et al.*, 2005; Claoué-Long *et al.*, 2008).

The Warumpi Province defines a distinct geological terrane along the southwest margin of the Arunta Region that accreted onto the North Australian Craton at *ca.* 1640 Ma (Scrimgeour *et al.*, 2005). It is similar to the southern tectonic zone defined by Shaw *et al.* (1984), although it does not continue east past Alice Springs. Sedimentary and igneous rocks composing the Warumpi Province have protolith ages in the range *ca.* 1690–1600 Ma (Scrimgeour, 2004). The province is separated from the Aileron Province to the north by a series of major faults and shear zones including the Redbank Thrust that have been collectively termed the Central Australian Suture (Shaw & Black, 1991; Close *et al.*, 2003; Scrimgeour *et al.*, 2005).

In the eastern part of the Arunta Region, the Irindina Province comprises Neoproterozoic to Cambrian successions of the Harts Range Metamorphic Complex. Shaw *et al.* (1984) included this terrane in the central tectonic zone of their tectono-stratigraphic framework of the Arunta. However, it has now been demonstrated that these rocks underwent high-grade metamorphism during the Early Ordovician and were subsequently juxtaposed against the surrounding Strangways Complex during the early Alice Springs Orogeny at *ca.* 450–440 Ma (Buick *et al.*, 2001; Maidment *et al.*, 2002).

1.3 LOCAL GEOLOGY OF THE REYNOLDS–ANMATJIRA RANGES

The Reynolds and adjacent Anmatjira ranges form an approximately 120km long, northwest trending, orogenic belt in the central part of the Aileron Province (Vry *et al.*, 1996; Figure 1.1). The terrane consists of multiply deformed, polymetamorphosed basement rock, which collectively records Early-Proterozoic to mid-Palaeozoic orogenesis affecting much of the Arunta Region (Stewart *et al.*, 1984; Shaw *et al.*, 1984).

1.3.1 Lander Package (1865–1820 Ma)

The earliest rocks in the region compose a widespread clastic sedimentary unit across the north and west of the Aileron Province, constituting more than 60% of the exposed geology (Pietsch, 2001; Claoué-Long & Edgoose, 2008). Collectively known as the Lander Package, this unit is synonymous with the Lander Rock Beds, Lander Rock Formation and Mount Stafford Member and constitutes Division 2 rocks of Stewart *et al.* (1984). The package is dominated by interlayered

pelites and psammites (and their metamorphosed equivalents) along with minor calc-silicate rocks, basalt lavas and metadolerite. The sequence represents largely turbidite-style sedimentation, although in places marginal-marine and fluvial environments are interpreted (Pietsch, 2001; Scrimgeour, 2003). Basement to the Lander Package has not been identified and consequently the thickness of the sedimentary pile is unconstrained.

Comprehensive detrital zircon studies by Claoué-Long & Edgoose (2008) and Claoué-Long *et al.* (2008) constrain deposition of Lander Package protolith sediments to after *ca.* 1865 Ma based on the youngest coherent group of detrital zircon ages. These authors also observed a consistent provenance in Lander Package detrital zircon age distributions, which are dominated by *ca.* 1880–1840 Ma detritus (generally contributing >40% of the detritus).

1.3.2 Stafford Event (1810–1800 Ma)

The minimum depositional age of the Lander Package is constrained by an early suite of granitoids that extensively intruded the Lander Package during a province wide tectono-magmatic episode known as the Stafford Event, which continued from *ca.* 1810–1800 Ma (Collins & Williams, 1995; Scrimgeour, 2003).

Metamorphism and deformation associated with the Stafford Event was spatially associated with the Mount Stafford and Harverson granites that intrude Lander Package sedimentary rocks in the northern Anmatjira Range, and central Reynolds Range respectively (Collins & Vernon, 1991; Collins & Williams, 1995; Hand & Buick, 2001). In the Mount Stafford region, metapelitic and metapsammitic rocks of the Mount Stafford Member were metamorphosed under low-pressure (*ca.* 2.5 kbar) conditions in association with a significant lateral increase in temperature (*ca.* 400°C–800°C) over a distance of around 4 km (Vernon *et al.*, 1990; Collins *et al.*, 1991). High-grade metamorphism associated with the Stafford Event was not accompanied by pervasive deformation, and has consequently been referred to as a contact metamorphic effect of regional scale (Clarke *et al.*, 1990; Collins & Vernon, 1991; Hand & Buick, 2001).

1.3.3 Reynolds Package (*ca.* 1780 Ma)

Together with the early suit of Stafford Event granitoids, the Lander Package forms the basement substrate onto which platform-style sediments of the Reynolds Package were deposited. The Reynolds Package is preserved mainly as discontinuous erosional remnants in the keels of major synclines in the north and west of the Aileron Province (Claoué-Long *et al.*, 2008). In the NW Reynolds Range, Lander Package sedimentary rocks are separated from those of the overlying Reynolds Package by a moderately angular unconformity of *ca.* 40° (Collins & Shaw, 1995). The Reynolds Package is synonymous with the Reynolds Range Group (RRG) and constitutes Division

3 rocks of Stewart *et al.* (1984). The package consists of basal conglomerate and quartz-sandstone (Mt Thomas Quartzite), pelite, arkose and calc-silicate rocks, interpreted by Dirks (1990) as representing shallow marine to intertidal sedimentation.

The maximum depositional age of the Reynolds Package is constrained by the 1810-1800 Ma Stafford Event granitoids that intrude the underlying Lander Package, and an unnamed sandstone unit dated at <1805 Ma (Claoué-Long *et al.*, 2008) that occurs immediately below the angular unconformity.

1.3.4 Yambah Event (1780-1770 Ma)

Intruding the Reynolds Package, and therefore constraining the minimum depositional age of the protolith sediments, is a later suite of flat-lying granitic plutons denoting the 1780-1770 Ma Yambah magmatic event (formerly the Early Strangways Event of Collins & Shaw, 1995). In the Reynolds-Anmatjira ranges, this event was characterised by abundant felsic magmatism, accompanied by local fabric development and contact metamorphism at P-T conditions of *ca.* 3.5 kbar and 550°C (Hand & Buick, 2001). The granitic precursors of the Warimbi Schist and Napperby Gneiss, which intruded both Lander and Reynolds package rocks at 1785±22 Ma and 1780±10 Ma respectively, are representative of Yambah Event magmatism in the Reynolds-Anmatjira region (Collins & Williams, 1995). Claoué-Long & Hoatson (2005) made comment on the brief time interval separating the Stafford and Yambah events, suggesting the later may or may not represent a continuation of the earlier system.

1.3.5 Chewings Orogeny (1590-1560 Ma)

The 1590-1560 Ma Chewings Orogeny forms part of a more extensive intra-cratonic event that affected much of Palaeoproterozoic Australia (Scrimgeour, 2004). The expression of the Chewings Orogeny in the Reynolds-Anmatjira ranges is predominantly thermal in nature, evidenced by a distinct geochronological overprint accompanying a continuous increase in metamorphic grade, from greenschist facies in the northwest to LPHT (4-5 kbar and 750-800°C) granulite facies in the southeast, observed along the length of the Reynolds Range (Vry *et al.*, 1996; Williams *et al.*, 1996; Rubatto *et al.*, 2001). Widespread and varied deformation of both Lander and Reynolds package sedimentary rocks and their metasedimentary equivalents, along with gneissic fabric development in both Stafford and Yambah event granitoids occurred during the Chewings Orogeny (Hand *et al.*, 1995; Vry *et al.*, 1996; Williams *et al.*, 1996; Rubatto *et al.*, 2001). Intense upright SE-trending folds that developed in response to NE-SW oriented compression can be traced along the length of the Reynolds Range where in the NW the axial surface fabric overprints Yambah Event contact

metamorphic assemblages (Hand & Buick, 2001). Williams *et al.* (1996) demonstrate the long-lived nature of the Chewings Orogeny using concordant and discordant leucosome segregations that formed over 26 ± 3 million years, suggesting HT metamorphism outlasted pervasive deformation.

Despite the prevalence of Chewings Orogeny ages seen in metamorphic zircon studies there is no magmatism associated with the Chewings Orogeny in the Reynolds–Anmatjira region. Consequently the nature of the thermal processes responsible for regional LPHT metamorphism during the Chewings Orogeny remains unclear. However, several lines of evidence presented by Hand & Buick (2001) suggest high-levels of crustal heat production may be associated with high-heat producing granites of the earlier Stafford and Yambah events resulting in anomalous thermal gradients.

1.3.6 Alice Springs Orogeny (450-300Ma)

The Alice Springs Orogeny was a protracted period of intracratonic tectonism that affected the Arunta Region during the Palaeozoic (Collins & Shaw, 1995; Hand & Buick, 2001). In the Reynolds–Anmatjira ranges, Proterozoic tectono-metamorphic features are over-printed by an anastomosing system of steeply dipping, SE and east-trending shear zones that developed in response to NNE–SSW convergent deformation (Collins & Teyssier, 1989).

The metamorphic grade of shear zones in the Reynolds Range increases from qz+chl+ms (greenschist facies) assemblages in the NW, to Ky+Bt+Sil+Mus (amphibolite facies) assemblages in the SE, similar to the regional isograds observed during the Chewings Orogeny (Buick *et al.*, 1999; Hand & Buick, 2001). Dirks *et al.* (1991) interpreted this similarity in metamorphic grade variation as an indication of temporal association, suggesting shear zone development began during the waning stages of Mesoproterozoic metamorphism in a transition from coaxial to non-coaxial deformation. It was only later retrogressive (Chl+Mus) overprints of these assemblages that Dirks *et al.* (1991) attributed to reactivation during the Alice Springs Orogeny, thus proposing a polyphase history. However, Cartwright *et al.* (1999) document Rb–Sr ages of sheared metapelites from Mt Boothby, and ^{40}Ar – ^{39}Ar ages of sheared granite from Sandy Creek yielding consistent *ca.* 334 Ma (Alice Springs Orogeny) ages, which they interpreted as indicating a temporally distinct tectonic episode, unrelated to tectonism during the Proterozoic. In light of the anomalous crustal heat production estimates of Hand *et al.* (1995; cited Hand & Buick, 2001), Hand & Buick (2001) suggest the similar metamorphic character of shear zones that formed during Alice Springs Orogeny was controlled by a thermal regime contributed to by Stafford and Yambah event granites.

1.3.7 High-grade Metasedimentary Units

The relatively simple geological framework of the Aileron Province presented thus far has emerged largely in response to an ever increasing geochronological dataset. However, during initial attempts to reconcile the geology of the Arunta Region, early workers isolated three granulite facies metasedimentary units from the regional stratigraphic framework (largely on the basis of grade and post depositional histories) assigning them to Division 1 of Stewart *et al.* (1984; Stewart *et al.*, 1980). These units include the Weldon, Aileron and Nolans Dam metamorphics. In the SE Anmatjira Range, granulite facies metasedimentary rocks of the Weldon Metamorphics are in faulted contact with low-grade Lander Package sedimentary rocks. On the basis of detrital zircon geochronology, the Weldon Metamorphics have been assigned as high-grade Lander Package equivalents by Claoué-Long *et al.* (2008). However, the relationships of the Aileron and Nolans Dam metamorphics with the regional stratigraphic framework remain undefined. Several authors have alluded to a correlation of the Aileron Metamorphics with the Lander Package on the basis of lithological similarity (Clarke & Powell, 1991; Collins & Shaw, 1995; Buick *et al.*, 1999; Cartwright *et al.*, 1999 and Pietsch, 2001). However, to date there has been no quantitative (geochronological) evidence published to substantiate this correlation.

This study will focus on granulite facies metasedimentary rocks of the Aileron Metamorphics outcropping in the Mount Boothby area to the NNW of Aileron in the SE Reynolds Range (Figure 1.1). At this location, units mapped as Aileron Metamorphics form several discontinuous enclaves and rafts (up to 4 km long) in voluminous Boothby Orthogneiss (Stewart *et al.*, 1980). To the southwest of Mount Boothby the unit is in contact with the northeast extent of the 1785 ± 22 Ma Napperby Gneiss (Collins & Williams, 1995).

1.4 RESEARCH AIMS & OBJECTIVES

This study aims to quantitatively constrain the timing of sedimentation, intrusion and subsequent metamorphism of the Aileron Metamorphics to establish their relationship with the regional stratigraphic framework of the Aileron Province.

The following objectives have been identified to achieve the proposed outcomes of the study:

- Establish a relative timing of events using field relationships complimented by microstructural analysis of overprinting tectonic fabrics.
- Determine the metamorphic grade of each tectonic fabric.
- Compare and contrast the detrital zircon age distributions and (where possible) the Hf isotope geochemistry of the Aileron Metamorphics with those of the Lander and Reynolds packages.
- Establish the emplacement age of the Boothby Orthogneiss, which envelopes the Aileron Metamorphics in the Mount Boothby area.
- Constrain the timing of granulite facies metamorphism in the area and the implications this has for the relative timing of fabric development.

2. FIELDWORK & MAPPING

2.1 OVERVIEW

Fieldwork was conducted intermittently over 22 days from July 1 to July 22, 2012 during undergraduate field study in the Arunta Region. Fieldwork was conducted from the Aileron Roadhouse, which operates a service station, general store and camping ground on the Stuart Highway approximately 120 km north of Alice Springs.

2.2 STUDY AREA

The study area covers *ca.* 5km² immediately to the north of Mount Boothby in the SE Reynolds Range, approximately 130 km NNW of Alice Springs (Figure 1.1). Access to the area is via a dirt track (4WD only) that turns west from the Stuart Highway 12 km north of Aileron. Vegetation consists mainly of patchy spinifex grass, with saplings, shrubs and more established trees occurring along drainages and the footslope of hills. Rock outcrop is restricted to areas of high topographical relief, which are separated by extensive alluvial flats of unknown thickness. In the south of the study area a Telecom microwave tower atop the hillcrest provides a prominent reference point, visible from much of the study area (Figure 2.1).



Figure 2.1 Caption continues onto following page.

Figure 2.1 Extensive alluvial flats separate Boothby Orthogneiss in the foreground from the prominent southern outcrop in the study area composed of Boothby Orthogneiss (less vegetated outcrop on the right) and inter-bedded pelitic and psammitic paragneiss (left) in the background. Telecom microwave tower in the background (left).

2.3 MAPPING & SAMPLING

High resolution satellite images were used as base maps in order to map out the extent and relationships between the primary lithologies. Outcrops in the study area were extensively traversed on foot to observe rock type, structure and field relationships. Sample locations were recorded using a Garmin GPSmap 62s, Geocentric Datum of Australia 94 (GDA94), UTM Zone 53. In total, 43 samples were collected in the study area; their grid-reference and brief description is provided in Appendix 1.

A 5 km² area was mapped (Figure 2.2) comprising five rock types; the Aileron Metamorphics were subdivided into three groups: i) inter-bedded pelitic and psammitic paragneiss, ii) K-feldspar-quartz-sillimanite-phlogopite paragneiss and iii) calc-silicate gneiss. The Boothby Orthogneiss is dominated by K-feldspar augen orthogneiss with minor leucocratic (plagioclase-quartz-K-feldspar-tourmaline-biotite) orthogneiss.

Metasedimentary rocks are dominated by thickly inter-bedded (cm-scale) pelitic and psammitic paragneiss and lesser quartzite horizons (Figure 2.2, 2.3). Sillimanite and cordierite assemblages and extensive leucosome indicate granulite facies metamorphism of these rocks. Local outcrop-scale diatexite was mapped directly north of the microwave tower (Figure 2.4). All pelitic and psammitic rocks are complexly deformed with multiple generations of deformation, except the igneous components of diatexite, which are undeformed.

A distinctive quartzo-feldspathic sillimanite-rich unit (200 m thick) is conformable with the main structural grain of the map and outcrops through the centre of the study area (Figure 2.2, 2.5). Bedding is poorly preserved within the massive unit and migmatite is rare. Another unique rock type forms a low-moderate relief hill in the centre east of the field area, composed of calc-silicate gneiss. Compositional layering (cm-scale) within the unit is interpreted as bedding. This unit is interpreted to be the metamorphosed equivalents of a bedded siliceous dolomite (Figure 2.2, 2.6).

The inter-bedded pelitic and psammitic paragneiss has a gradational contact with Boothby Orthogneiss comprising a high proportion of migmatite, suggesting the relationship is intrusive. The Boothby Orthogneiss is a coarse grained K-feldspar augen orthogneiss (Figure 2.7a). Feldspar augen commonly display rapakivi textures of plagioclase mantles on K-feldspar augen, the former weathers preferentially emphasising the structures. The unit forms moderate relief boulderous to whale back outcrops. Local migmatite involves garnet surrounded by leucosome and post-dates the

main deformation events. Minor garnet-bearing dykes cut the gneissic fabric. A minor, though distinctive, component of the Boothby Orthogneiss includes sugary-textured leucocratic granitoid with dark ovoid blebs that are 1–2 cm across (Figure 2.7b). This component has a sharp contact with the main phase of the Boothby Orthogneiss. However, high-strain precludes the interpretation of which phase came first.

The study area is dissected by an anastomosing system of steeply dipping, east-west shear zones, which in paragneiss outcrop weather recessively with respect to adjacent gneissic lithologies forming drainages through the hill-slope. Sample sites of interest to the present study are shown in Figure 2.2.

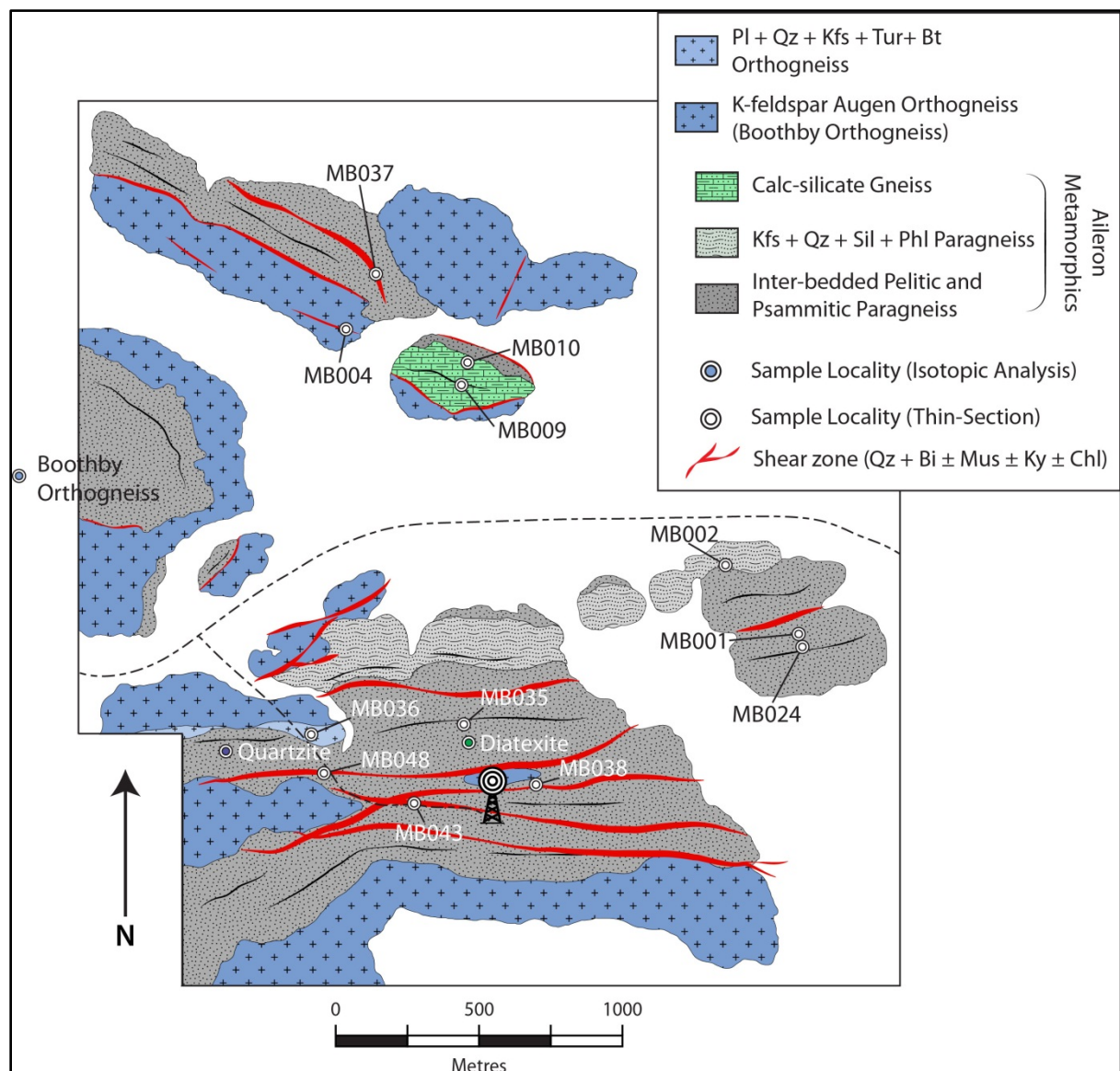


Figure 2.2 Generalised geological map of the study area displaying prominent rock-types and sample localities of specimens analysed in this study. The microwave tower in the south of the study area provides a prominent geographical reference point visible from much of the area.



Figure 2.3 Inter-bedded pelitic and psammitic paragneiss. Scale is 200 mm in length.



Figure 2.4 Diatexite outcrop sampled for metamorphic zircon (sample MB033). Note the undeformed nature of the K-feldspar-rich leucosome relative to the melanosome, which displays a sillimanite gneissosity. Scale is 200 mm in length.



Figure 2.5 Kfs+Qz+Sil+Phl paragneiss outcrop displaying compositional layering interpreted as primary bedding (S0). Scale is 200 mm in length.



Figure 2.6 Calc-silicate gneiss outcrop displaying compositional layering interpreted as primary bedding (S0). Scale is 200 mm in length.

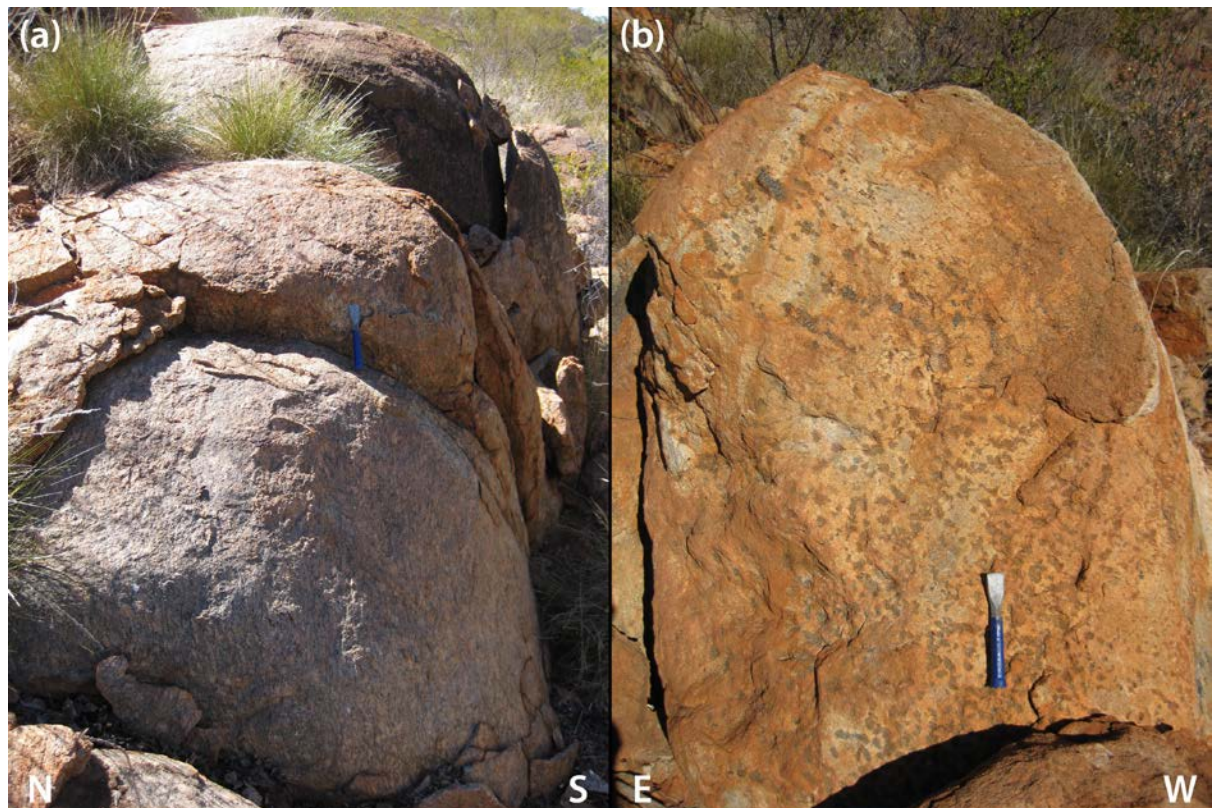


Figure 2.7 View looking east. (a) Boothby Orthogneiss weathers to metre sized rounded boulders largely devoid of vegetation. Note the near vertical gneissosity defined by alternating biotite and K-feldspar augen-rich layers. (b) Leucocratic granitoid composes a small portion of the Boothby Orthogneiss. Scale is 200 mm in length.

3. STRUCTURAL GEOLOGY

3.1 INTRODUCTION

Metasedimentary and metaigneous rocks in the study area preserve multiple structural elements indicative of a poly-tectonic history. This chapter describes the geometry and overprinting relationships of tectonic fabrics mapped in the study area and their relationship to primary rock type. Where possible, correlation has been made with the structural terminology used by earlier workers to characterise analogous structures elsewhere in the Reynolds–Anmatjira ranges. Structural measurements were taken in the field using a Suunto Global (M3) field compass set to a declination of 11°. Stereonet analysis was conducted using Stereonet version 8.8.3. Structural measurements taken in the study area are presented in Appendix 2.

3.2 EARLY AXIAL PLANAR FOLIATION (D1)

The earliest tectonic fabric identified in the study area is locally preserved in folded inter-bedded metapelitic and metapsammitic rocks outcropping in the east of the study area. A well-defined secondary foliation (S1) is most strongly developed in metapelitic horizons at a high angle to primary bedding (S0) in the hinges of rare tight to isoclinal F1 folds (Figure 3.1). The S1 foliation is defined by the preferential alignment of coarse grained sillimanite and regressive cordierite. In the limbs of F1 folds, S1 is parallel to bedding. The orientation of S1 varies from ESE to E striking and from steeply N dipping to steeply S dipping (Figure 3.2). Employing the acute bisector method of fold analysis the axial surface of F1 is estimated at 091°/82°S, and the fold axis plunge 39° towards 097°. Evidence of D1 is not observed in orthogneiss outcrop.

3.3 DOMINANT GNEISSOSITY AND FOLDING (D2)

Throughout the study area, the composite S0/S1 is intensely deformed by tight, steeply inclined–upright F2 folds that plunge moderately to the ESE (Figure 3.3). The axial surface of F2 folds varies between steeply N and steeply S dipping. Employing the acute bisector method of fold analysis, the axial surface of F2 is estimated at 104°/84°NNE and the fold plunge 43° towards 095°. In the field there is no evidence of axial planar foliation development in response to D2 in paragneiss, as a new foliation is difficult to distinguish from the transition of S0/S1. In orthogneiss outcrop, a penetrative ESE striking gneissosity is defined by biotite and K-feldspar augen. As with the axial surface of F2, the gneissosity varies between steeply N and steeply S dipping. The similar relative intensity and attitude of F2 folds in paragneiss and the penetrative gneissosity in orthogneiss suggests these structures are manifestations of the same deformation event, with morphological variation between sedimentary and igneous protoliths likely reflecting rheological contrast between these rock-types.

Consequently, the penetrative east-southeast striking gneissosity in orthogneiss outcrop is termed S2. Locally S2 is overprinted by undeformed garnet-bearing K-feldspar leucosome (Figure 3.5).

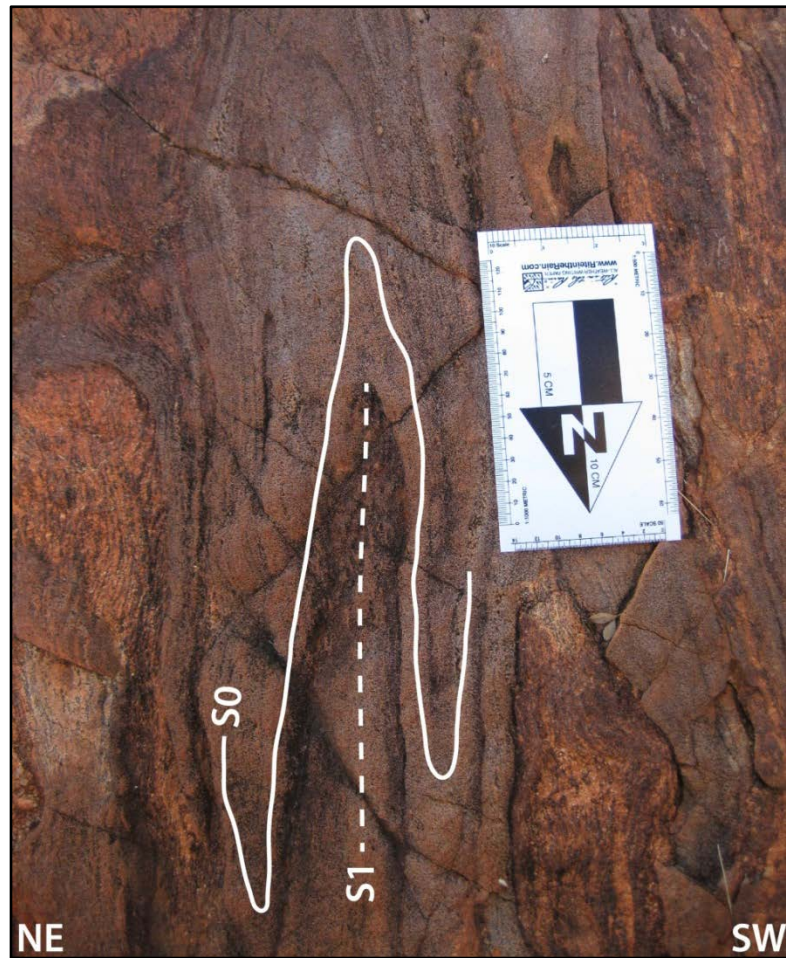


Figure 3.1 F1 fold in inter-bedded metapelite and metapsammitic paragneiss. S1 foliation defined by alignment of Sil+Crd sub-parallel to bedding (S0). Longest dimension of scale is 153 mm.

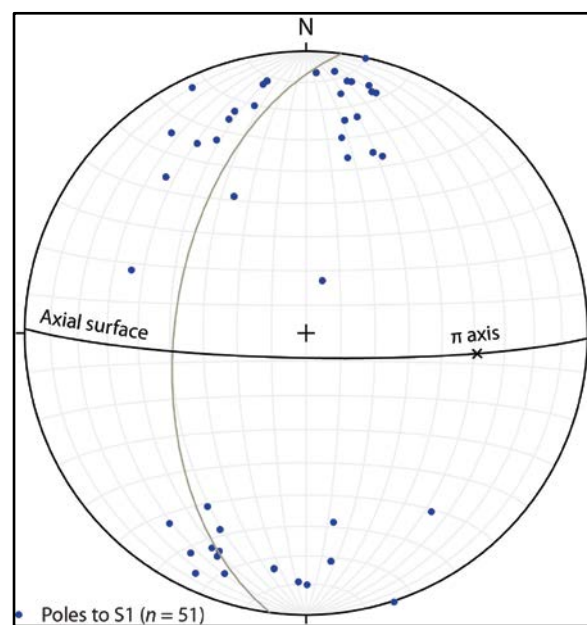


Figure 3.2 Poles to S1 measured in paragneiss outcrop.

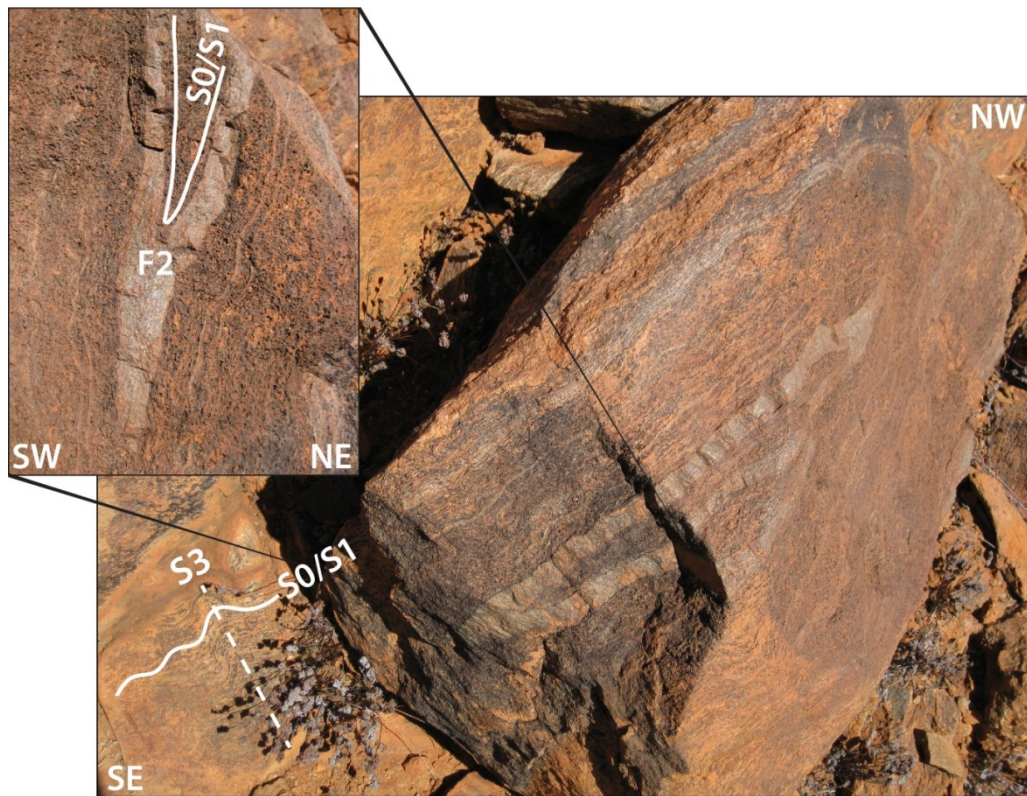
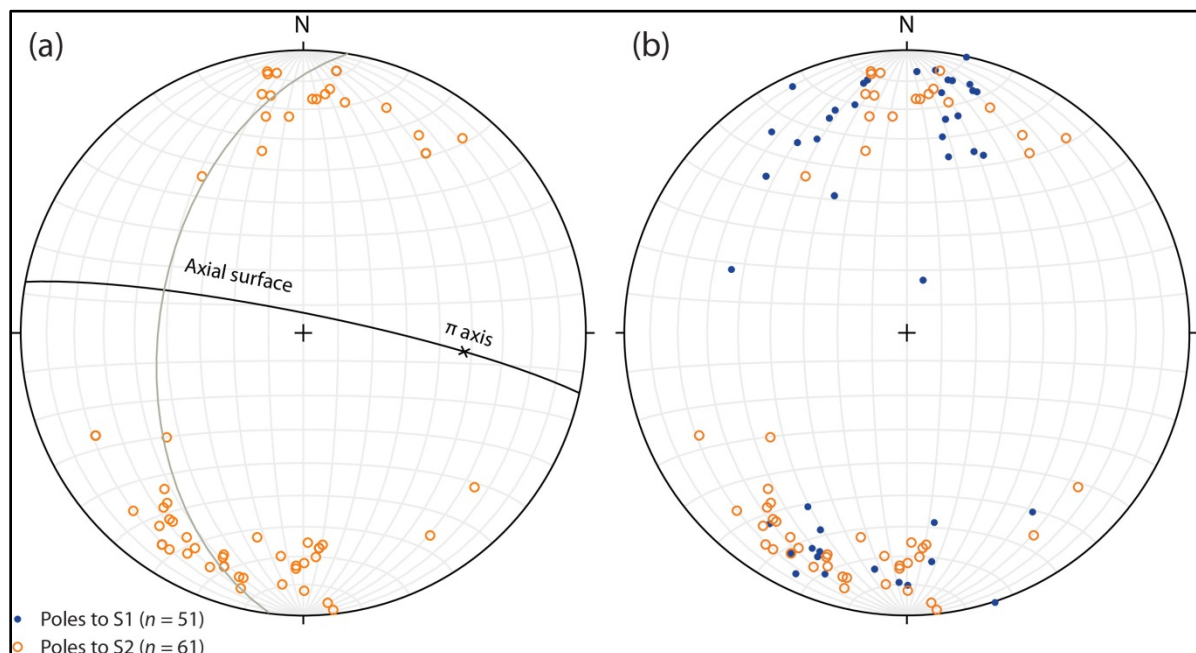


Figure 3.3 Deformed inter-bedded pelitic and psammitic paragneiss. Expanded view shows S0/S1 being refolded about a tight F2 fold. In the background (main view) S0/S1 is deformed by NNE striking D3 crenulations. Base of inset is *ca.* 45 cm.



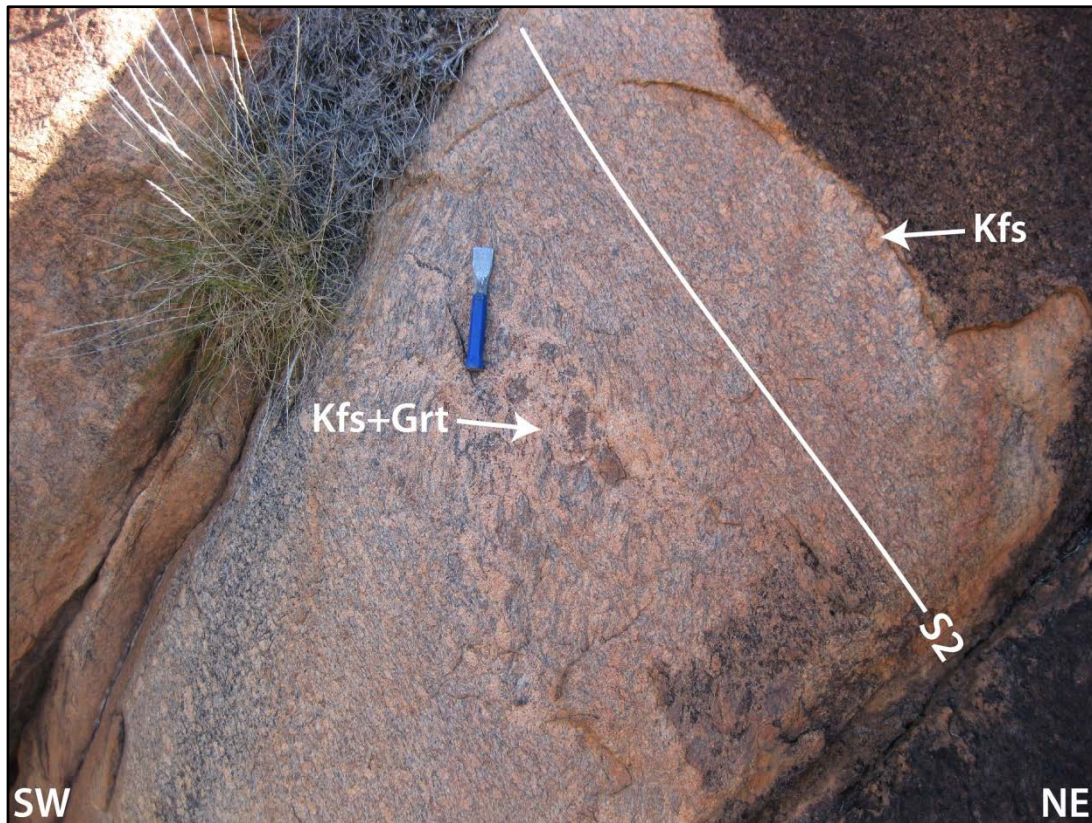


Figure 3.5 Penetrative S2 gneissosity developed in Boothby Orthogneiss in the west of the study area. The S2 gneissosity is steeply N dipping and defined by megacrystic Kfs+Bt. Note the Grt-bearing Kfs leucosome overprinting the S2 gneissosity. Scale is 200 mm in length.

3.4 NNE STRIKING SHEAR BANDS & CRENULATIONS (D3)

In metapelitic paragneiss outcrop, the composite S0/S1 is locally deformed by centimetre-scale crenulations with close to tight geometries, termed D3. The axial surfaces of F3 crenulations strike NNE and generally dip moderately to steeply W. When plotted on the stereonet, F3 fold axes form two populations along a best fit great circle 020°/74°ESE, plunging moderately S and moderately NNE in turn. Employing the acute bisector method of fold analysis indicates the F3 fold axis is deformed by shallowly WNW plunging (16°), open folds that dip steeply to the NNE (Figure 3.7a). These post-D3 folds are only indicated by stereographic analysis and were not observed in the field. In metapelitic horizons, D3 crenulations locally become obscured by disseminated leucosome (Figure 3.8).



Figure 3.6 Moderately S plunging S3 crenulations of the Sil+Crld S1 foliation in inter-bedded metapelitic (centre) and metapsammitic (top) paragneiss. Note the cavities produced by the differential weathering of coarse grained cordierite porphyroblasts. Scale is 200 mm in length.

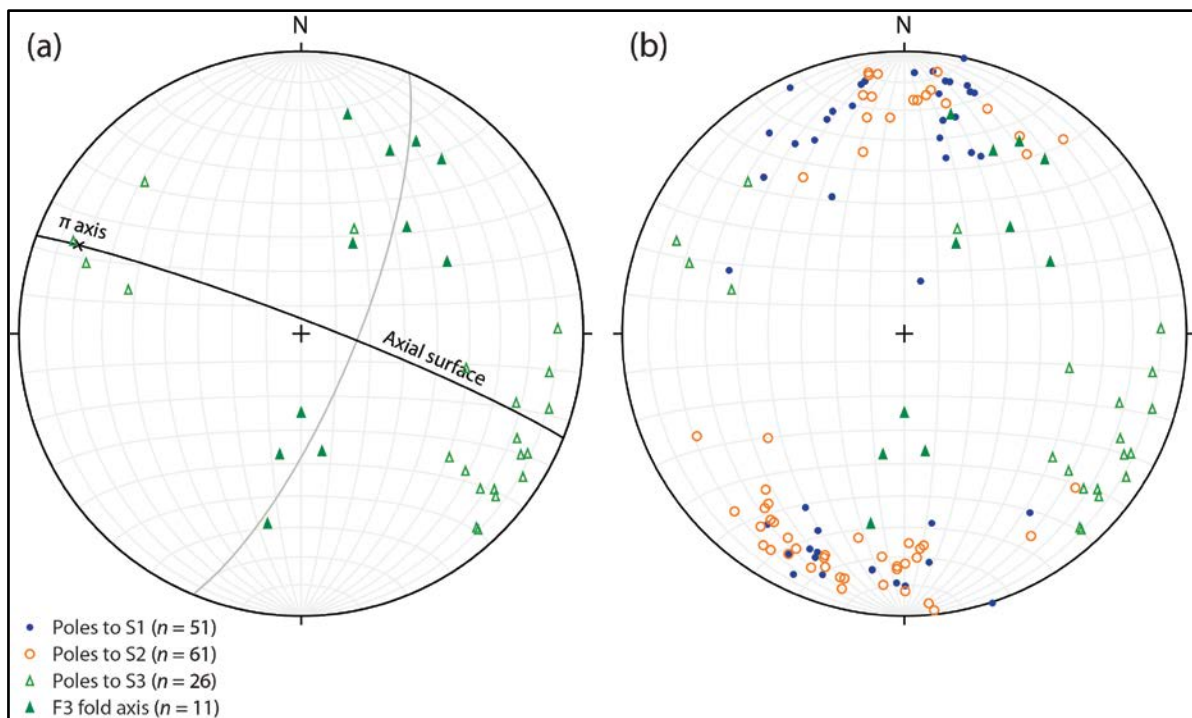


Figure 3.7 Caption continues onto following page.

Figure 3.7 (a) Poles to S3 and F3 fold axis lineations. Note the F3 fold axis is refolded by later open folds plunging shallowly to the WNW. (b) Combined poles to S1, S2, S3 and F3 fold axis. Note the orientation of D3 structures is in contrast to D1 and D2 structures.

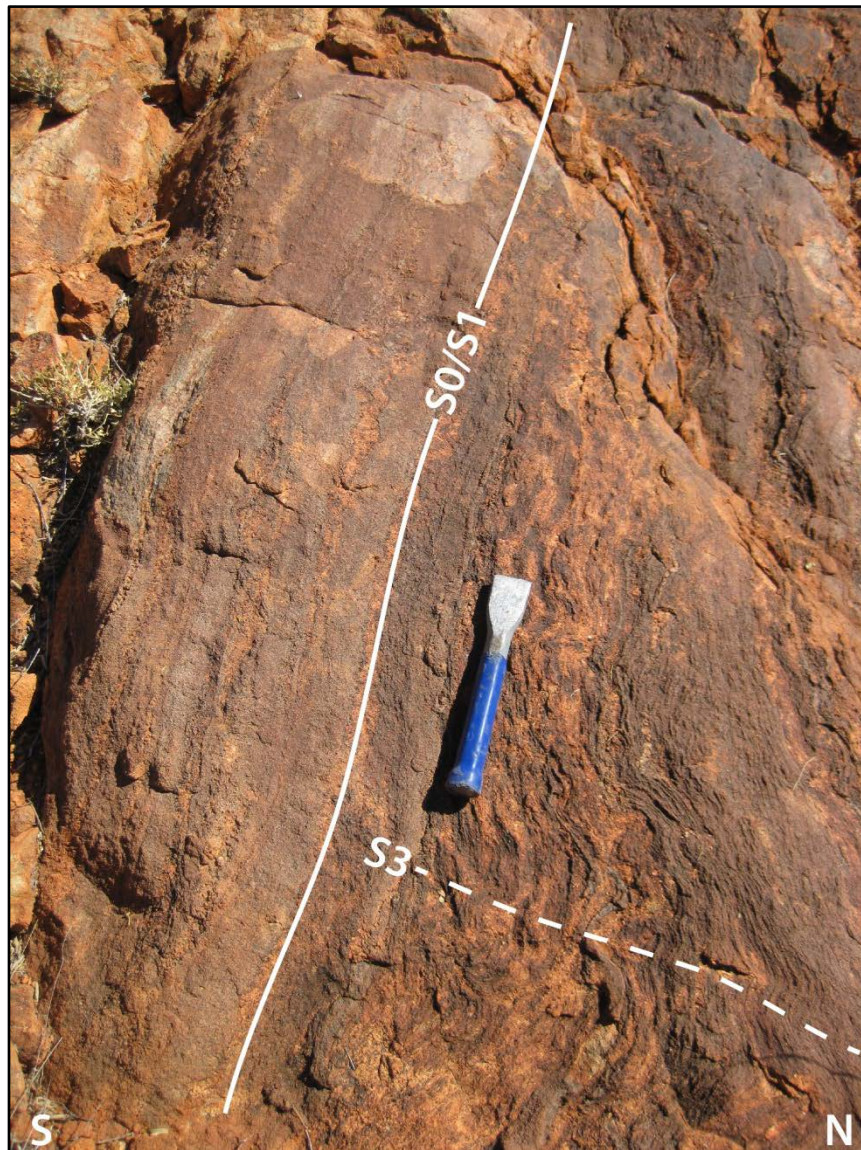


Figure 3.8 S3 crenulations of the Sil+Crd S1 foliation in inter-bedded metapelitic (right) and metapsammitic (left) paragneiss. Note the disseminated leucosome predominately developed in metapelitic horizons. Scale is 200 mm in length.

In the Boothby Orthogneiss, the pervasive S2 gneissosity is locally displaced along high strain ductile shear bands and lesser developed crenulation bands (Figure 3.9). These structures generally strike NNE and vary between steeply NW and steeply SE dipping. As with D2, the similar attitude of these structures to D3 crenulations in paragneiss outcrop suggests they are the manifestation of the same deformation event, with morphological variation between sedimentary and igneous protoliths likely reflecting rheological contrast between these rock-types. Distinction between shear bands and crenulation bands is a matter of scale, with incipient shear crenulations generally no more

than a few centimetres wide. In contrast the more developed shear bands are generally several centimetres wide and in the north of the study area form a metre-wide mylonite zone. In some instances, K-feldspar rich leucosome is localised along D3 shear bands in orthogneiss (Figure 3.9).



Figure 3.9 Vertical section normal to D3 shear band in Boothby Orthogneiss. Note minor leucosome localisation along shear band (top). Incipient shear crenulations are developed to the left of the main shear band. Sense of movement along S3 shear plane is east side up. Scale is 148 mm in length.

3.5 RETROGRADE SHEAR ZONES (D4)

All earlier fabrics are overprinted by a system of high-strain shear zones that dissect the study area termed D4. In paragneiss outcrop, shear zones compose micaceous schists comprising $Qz+Bt\pm Mus\pm Chl\pm Ky$ assemblages and commonly contain quartz veins localised within the shear plane (Figure 4.10). The S4 schistosity strikes WNW and dips steeply N with a subordinate set of

shear zones dipping to the S (Figure 3.12a). D4 shear planes generally contain a well-defined mineral lineation (L4) defined by the alignment of micaceous minerals and rarely kyanite. L4 shows some variation, though generally plunges moderately N (Figure 3.12a). Mica schists preserve rare shear bands that indicate a reverse sense of movement along these structures.

D4 high-strain zones developed in igneous protoliths produce a mylonitic foliation (Figure 3.11), which contains a mineral stretching lineation defined by relict K-feldspar porphyroclasts drawn out parallel to the transport direction. Asymmetric mantled porphyroclasts indicate a reverse movement sense along these structures.

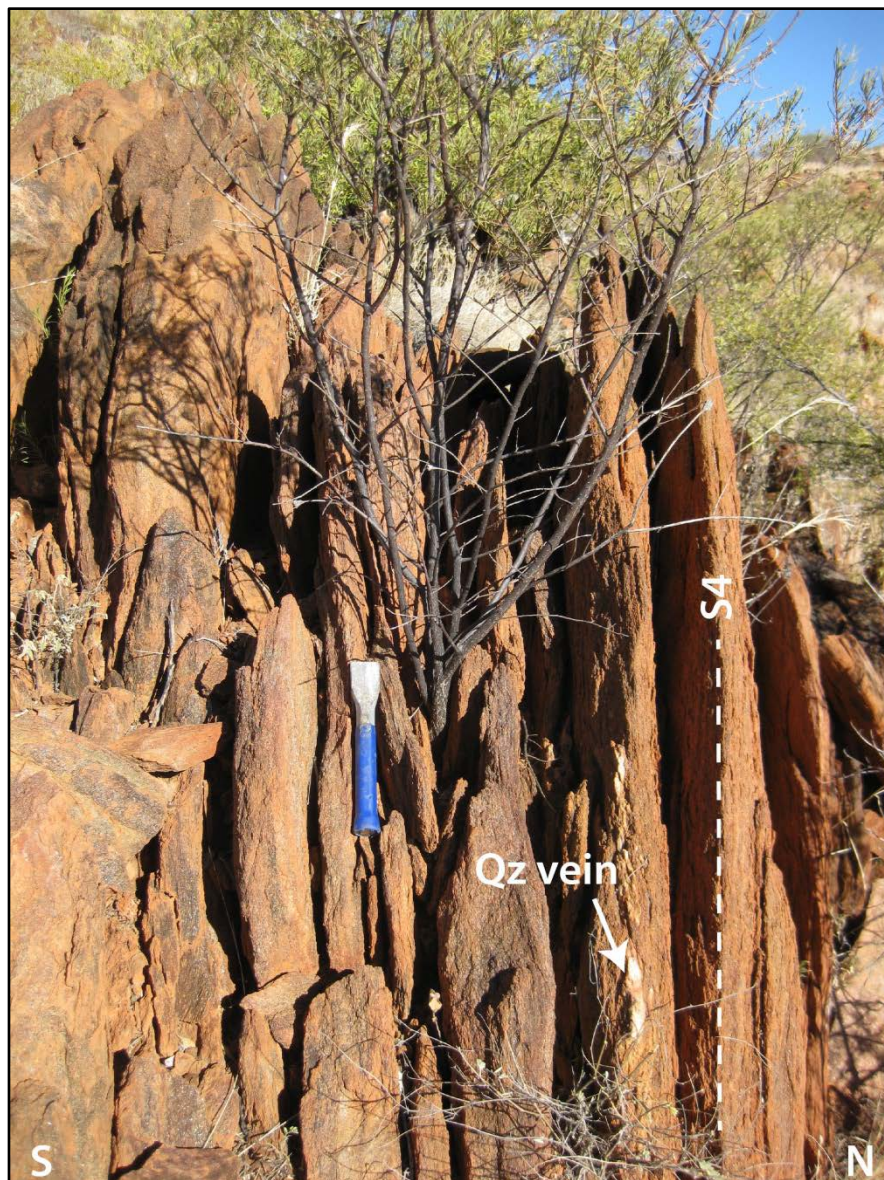


Figure 3.10 Vertical D4 shear zone developed in metasedimentary rocks. Shear zone is defined by $Qz+Bt+Ky$ schistosity. Note minor quartz veining developed parallel to the S4 schistosity. Scale is 200 mm in length.

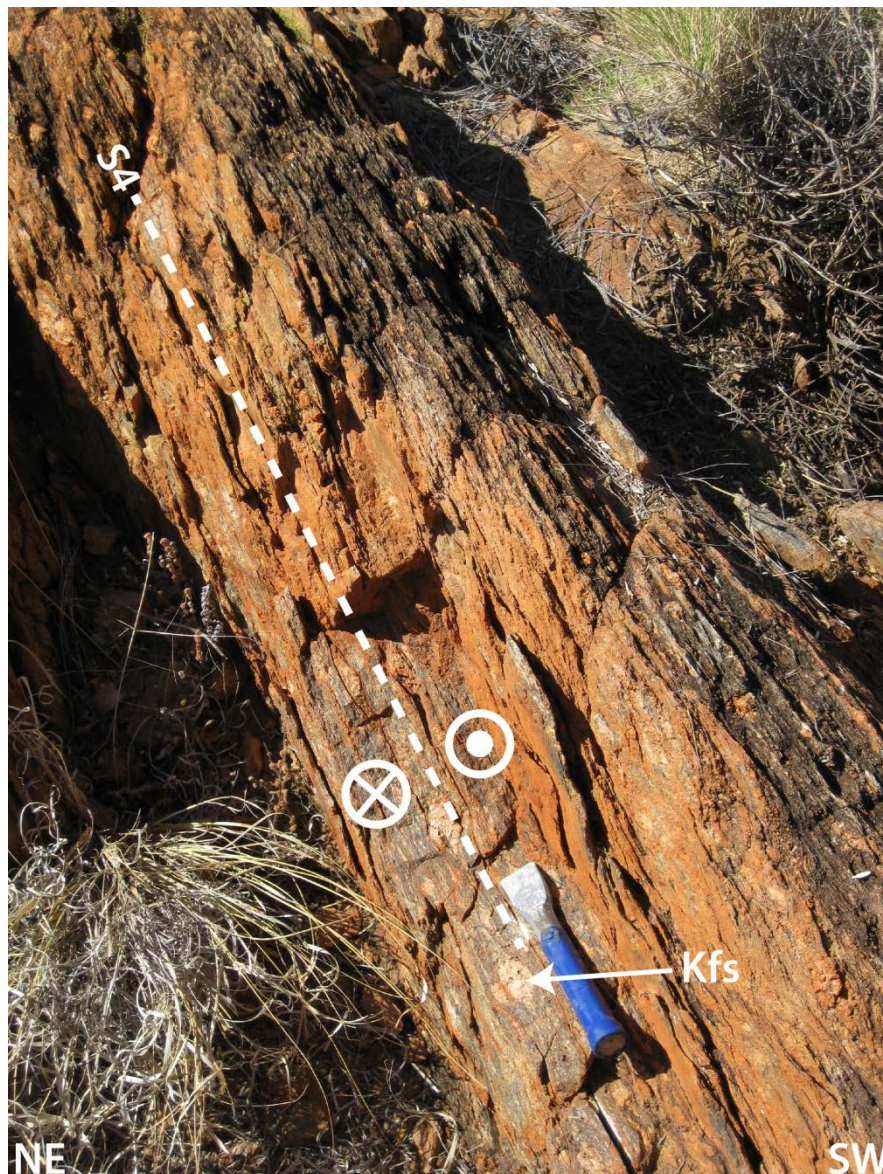


Figure 3.11 Steeply S dipping D4 mylonite shear zone developed in Boothby Orthogneiss. Note the cm sized relict Kfs-porphyroclasts. In the vertical plane normal to S4, asymmetric mantled Kfs-porphyroclasts indicate reverse sense of shear translating to S over N movement along the shear plane. Scale is 200 mm in length.

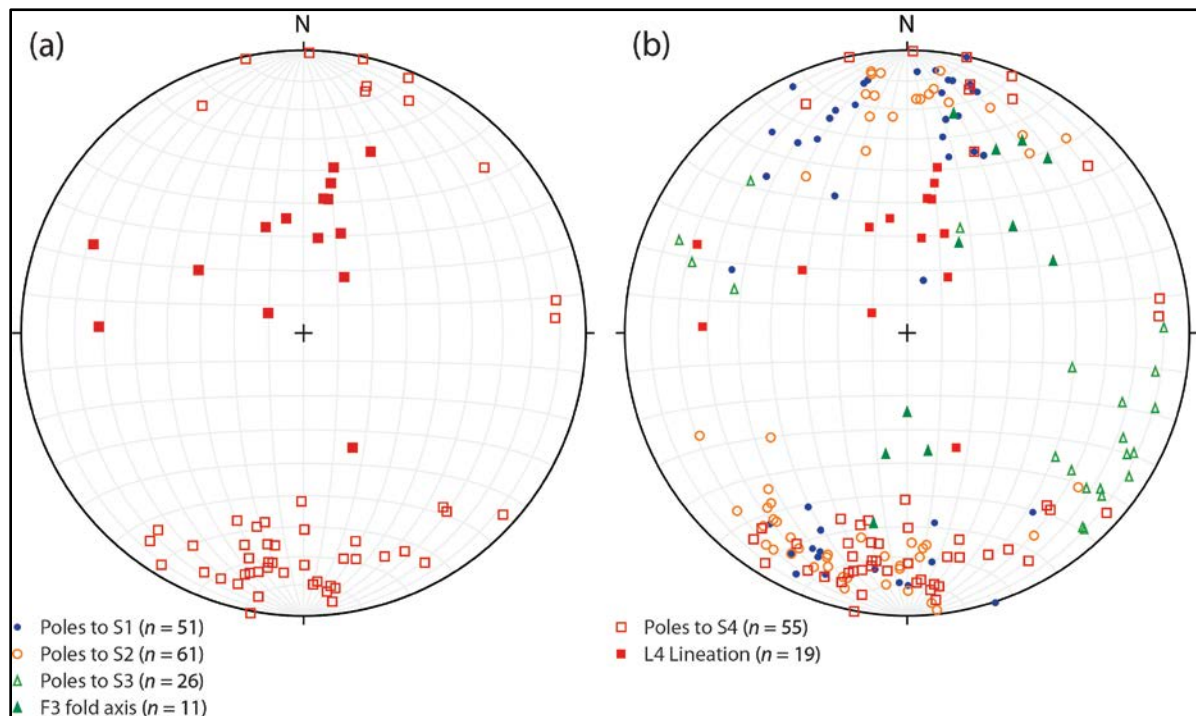


Figure 3.12 (a) Poles to S4 and L4 mineral lineations. Note the dominantly N dip direction of D4 shear zones. (b) Combined poles to S1, S2, S3 and F3 fold axis, S4 and L4. Note the orientation of D4 structures is similar to D1 and D2 structures.

3.6 DISCUSSION

Metasedimentary and metaigneous rocks in the study area preserve evidence of at least 4 deformation events, which are summarised in Table 3.1. D1 structures (S1, F1) are only observed in metasedimentary rocks of the Aileron Metamorphics and include tight, upright folds in response to N–S directed compressional tectonics at or above sillimanite isograd P–T conditions. S1 is sub-parallel to bedding. The protolith granitoid of the Boothby Orthogneiss, being devoid of D1 structures, is interpreted as post-D1. S1 and F1 are transposed into S2 and F2 during the dominant tectonic event in the mapping area (D2). S2 is also of sillimanite grade in the paragneiss and defines the main gneissosity in the Boothby Orthogneiss. F2 folds are tight and formed in ENE–SSW directed shortening. D3 comprises a less pervasive deformation event, which resulted in close to tight crenulations (F3) of bedding and earlier foliations. On the basis of orientation, shear bands in the orthogneiss are considered as D3 equivalent structures. However, a pervasive S3 foliation did not develop in either rock type. The minor D3 structures delineate SE–NW shortening. The most recent event to have affected rocks in the study area produced a system of WNW–ESE striking shear zones with predominately northward dip directions and subordinate set with southward dip directions. Moderate–steeply north plunging L4 lineations and asymmetric sense of shear indicators indicate a dominantly N over S transport. A minor transpressional component is evidenced by lineations plunging shallowly to the W and NW. This is consistent with the observations of Collins

& Teyssier (1989) who proposed a transpressional regime during the development of crustal scale “pop-up” structures in response to NNE–SSW directed shortening.

Table 3.1 Summary of structural elements mapped in the study area and correlative terminology of analogous structures mapped elsewhere in the Reynolds–Anmatjira ranges. ^aDirks & Wilson (1990), ^bCollins *et al.* (1991), ^cBuick *et al.* (1994).

Deformation Event	Structural Element		Structural Correlation
	Paragneiss	Orthogneiss	
D1	E–W striking, tight, upright folds, Sil+Crđ axial planar foliation	Pre-granitoid emplacement	^a DI ₁ , ^b D _{1c}
D2	WNW–ESE striking, tight, upright folds	WNW–ESE striking, steeply dipping Bt+Kfs gneissosity	^a DII ₂ , ^b D _{2d}
D3	NNE–SSW striking crenulations of S1 foliation	NNE–SSW striking, steep–moderately dipping S3 shear and crenulation bands	^a DII ₃ , ^c D3
D4	WNW–ESE striking, steeply dipping shear zones; shallowly WNW plunging, open folding of F3 crenulation fold axis	WNW–ESE striking, steeply dipping mylonitic shear zones; minor reorientation of S2	^a DII ₄ , ^c D4

On the basis of orientation, fold style and cross cutting relationships with local granites, D1 is correlated with DI₁ of Dirks & Wilson (1990) in the Mt Thomas area, who in turn correlate their event with S_{1c} of Collins *et al.* (1991) in the Mt Stafford area. On the basis of metamorphic grade, intensity of fabric development, fold geometry and similar deformation of the Yakalibadgi Granite near Mt Thomas, D2 correlates with the DII₂ of Dirks & Wilson (1990) and D_{2d} of Collins *et al.* (1991). The morphology and orientation of S3 shear bands in the Boothby Orthogneiss correlate with DII₃ shear crenulations of Dirks & Wilson (1990). Buick *et al.* (1994) also correlate non-pervasive crenulation bands SE of Mt Thomas with DII₃ shear crenulations of Dirks & Wilson (1990). Open folding of the F3 crenulation axis is inferred from stereographic analysis rather than observed in the field and is interpreted as minor buckling in response to NNE–SSW directed compression during D4. It is likely that these post-D3 folds also produced the dip variation observed in D2 structures. High-strain D4 shear zones are well documented in the Reynolds–Anmatjira ranges and there is an increasing consensus amongst workers that these structures formed exclusively

during the Palaeozoic Alice Springs Orogeny (Collins & Teyssier, 1989; Cartwright *et al.*, 1999; Hand & Buick, 2001). D4 shear zones of this study correlate with DIII of Dirks & Wilson (1990) and D4 of Buick *et al.* (1994).

The hydrous mineralogy of D4 shear zones indicates these structures were the focus of intense hydration from granulite facies assemblages. This interpretation is supported by the localisation of quartz veins along many D4 shear zones and suggests these structures acted as conduits for hydrothermal fluid flow during the Palaeozoic. In the eastern MacDonnell Ranges district, the circulation of hydrothermal fluids along Alice Springs Orogeny shear zones produced the Winnecke Au mineralisation (Skwarnecki, 2004).

D1 is inferred by Dirks & Wilson (1990) to predate *ca.* 1800 Ma Stafford Event granites. D2 overprints Yambah Event granites near Mt Thomas (Dirks & Wilson, 1990), suggesting the deformation is likely to be of Chewings Orogeny age. Leucosome localised along D3 equivalent shear bands in the Napperby Gneiss were dated by Hand *et al.* (1995) at 1570 ± 6 Ma indicating these structures were at least active during the Chewings Orogeny and likely formed during this time.

Using the whole-rock Rb–Sr method of dating, Cartwright *et al.* (1999) constrained the development of D4 shear zones to 333 ± 16 Ma, placing shear zone development within the Alice Springs Orogeny.

4. PETROGRAPHY

4.1 INTRODUCTION

The study area comprises several prominent rock-types of varying mineralogical and geochemical composition, and metamorphic grade. This chapter documents petrographic descriptions of representative rock-types outcropping in the study area and complements structural observations of the previous chapter. The samples have been grouped on the basis of protolith (sedimentary and igneous) and metamorphic grade. A list of samples selected for thin-sectioning is provided in Appendix 1.

4.2 METHODS

Twenty-three polished thin-sections were prepared for petrographic examination. Blocks were cut from hand specimens so as to best represent the structural or mineralogical element of interest. L-S tectonites were cut perpendicular to foliation and parallel to lineation to expose shear sense indicators. Micro-folds were cut perpendicular to the fold axis, exposing the profile of these structures. Samples were resin impregnated and mounted onto glass slides before being ground to the conventional thickness of *ca.* 30µm. Samples were examined using transmitted light microscope techniques for mineralogy, growth habit, grain size, modal abundance, grain boundary relationships and tectonic microstructure. The modal abundances of individual phases were determined using a Swift automatic point counter measuring a 500 point grid on each thin-section. Photomicrographs of representative or characteristic microstructures were captured using NIS-Elements (version 4.11) remote capture software controlling a Nikon DS-Fi1 high-definition camera head fitted to a Nikon eclipse 50iPOL binocular microscope. Morphological terminology used to classify foliations is that of Passchier & Trouw (2005) and mineral abbreviations are those of Whitney & Evans (2010).

4.3 METASEDIMENTARY PROTOLITHS

4.3.1 Paragneiss

These include inter-bedded pelitic and psammitic granulites preserving D1–D3 structures sampled from the south, and southeast of the study area.

CORDIERITE-SILLIMANITE-BIOTITE PARAGNEISS (MB001)

Mineral modal abundances are Cordierite = 59 vol.%, Sillimanite = 18 vol.%, K-feldspar = 11 vol.%, Biotite = 2 vol.%, Quartz = 1-2 vol.%. Rutile/Ilmenite <1 vol.%, Zircon/Monazite <1 vol.%, Apatite <1 vol.%.

The very high mode of cordierite and sillimanite suggest the protolith of this sample was a pelite. Cordierite forms large poikiloblasts up to 12 mm in the longest dimension (Figure 4.1). Cordierite poikiloblasts contain abundant randomly oriented inclusions of fine grained radiogenic minerals, namely zircon and monazite, which become less prevalent toward the rim (Figure 4.1, top right), or inclusions of biotite and equigranular apatite. The margins of cordierite poikiloblasts contain inclusions of fine sillimanite aligned with the external sillimanite-bearing foliation (S1).

The matrix of the rock contains K-feldspar with flame textures, quartz, sillimanite (both fibrolite and coarse grains), biotite, and accessory rutile, ilmenite, zircon, monazite and apatite. The sillimanite-biotite foliation (S1) is locally crenulated (F3; Figure 4.1). F3 crenulated biotite is partially pseudomorphed by fibrolitic sillimanite. There is minor chlorite alteration of the cordierite rims.

CORDIERITE-SILLIMANITE-BIOTITE PARAGNEISS (MB024)

Mineral modal abundances are Cordierite = 59 vol.%, Sillimanite = 21 vol.%, K-feldspar = 11 vol.%, Biotite = 2 vol.%, Quartz = 2 vol.%. Rutile/Ilmenite <1 vol.%, Zircon/Monazite <1 vol.%, Apatite <1 vol.%.

Sample MB024 is mineralogically similar to sample MB001 (above), and was sampled at the same location, though preserves distinct microstructures. Cordierite forms domains of strongly recrystallised polygonal grains that are wrapped by sillimanite-biotite bearing foliation domains (Figure 4.2a, b). Locally occurring between cordierite grains are irregular shaped pockets of undeformed K-feldspar neosome (Figure 4.2c, d). In the foliation domain, fibrolitic sillimanite is overprinted by coarse grained euhedral prisms of randomly oriented sillimanite (Figure 4.2a, b).

The matrix of the rock contains K-feldspar with flame textures, quartz, sillimanite (both fibrolite and coarse grains), biotite, and accessory rutile, ilmenite, zircon, monazite and apatite.

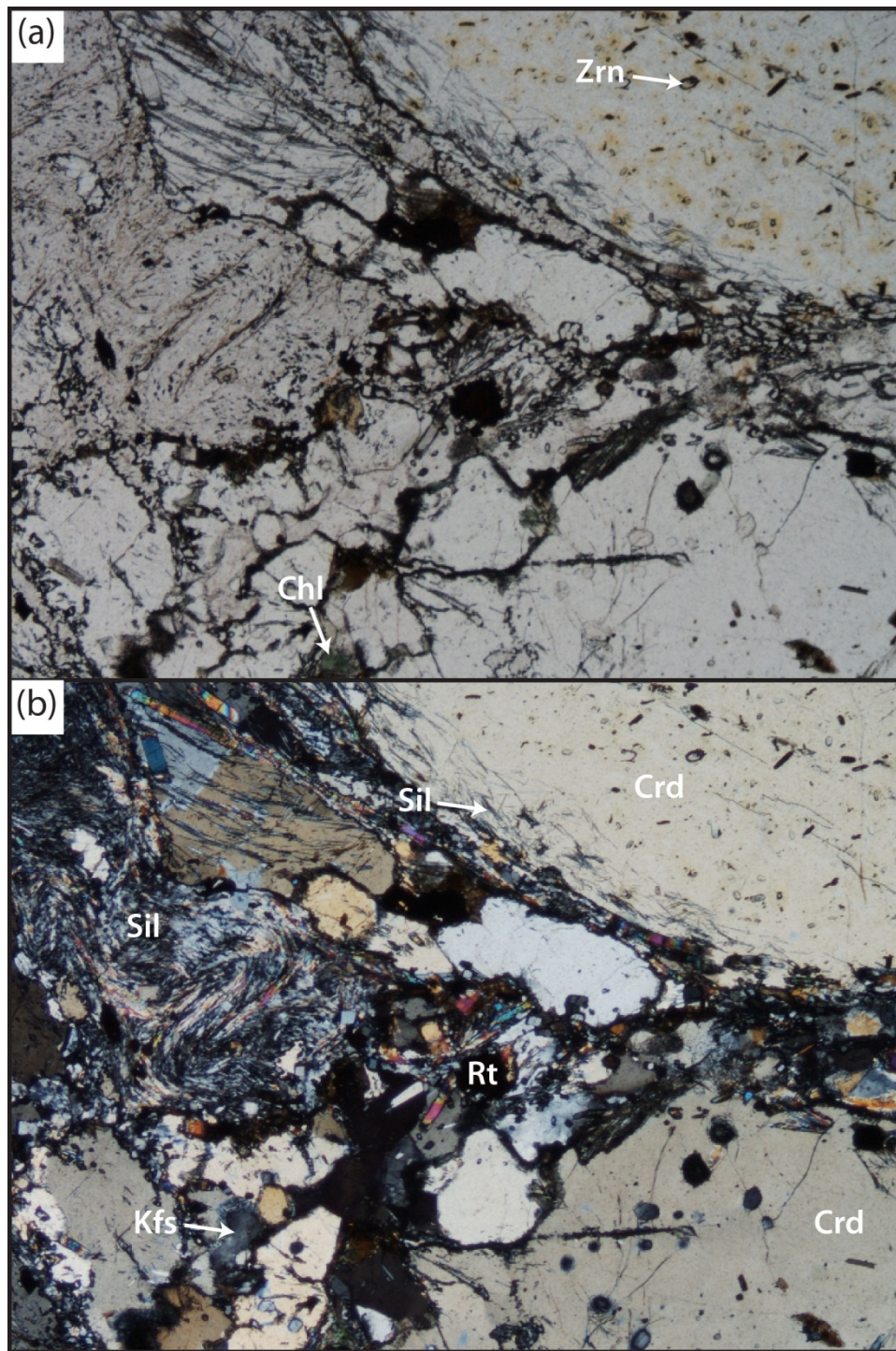


Figure 4.1 Photomicrograph of metapelite sample MB001 in (a) PPL and (b) XPL. In the central left of the image, fine grained sillimanite is tightly crenulated by D3. Base of image is 4.3 mm.

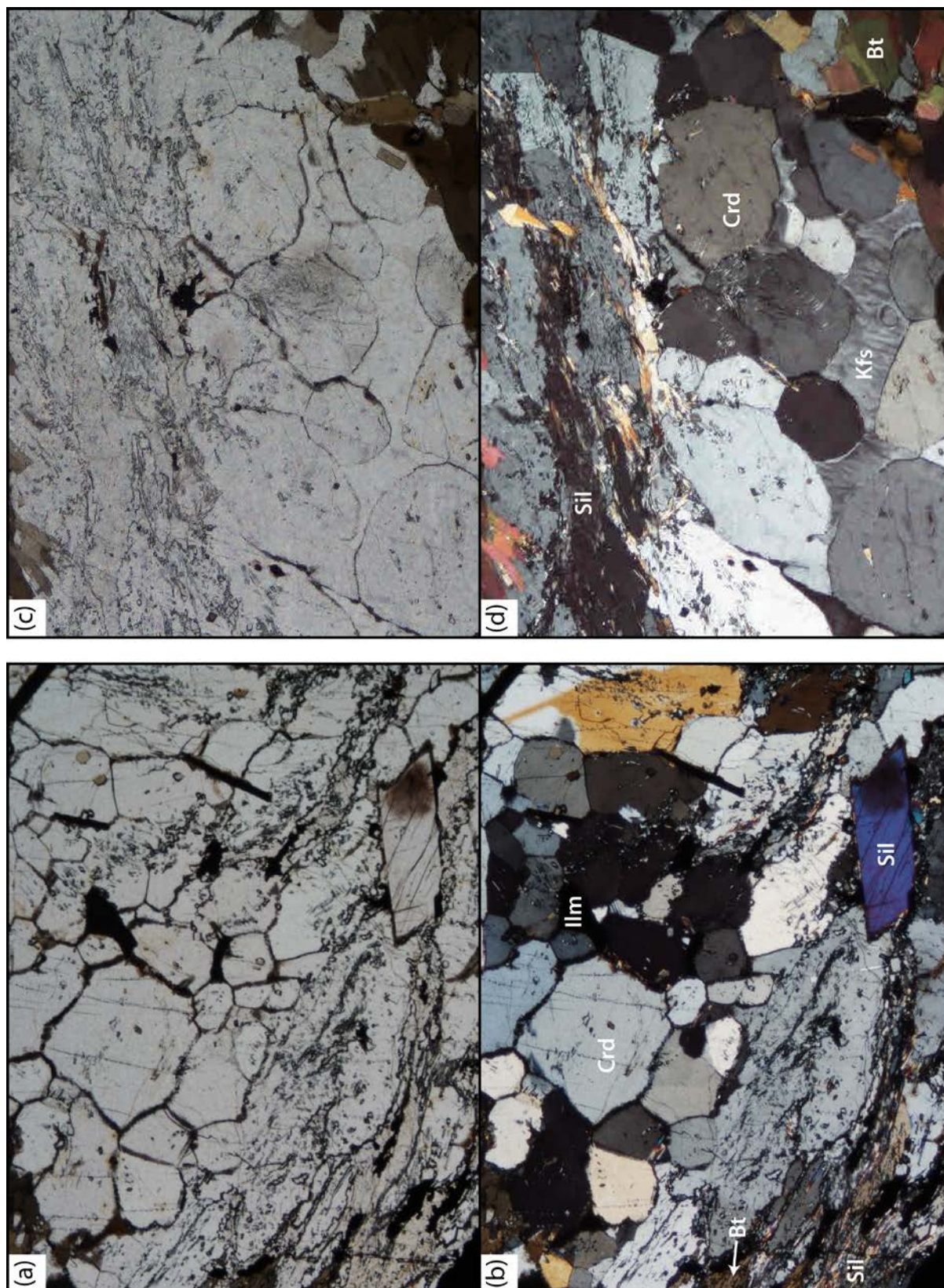


Figure 4.2 Photomicrographs of sample MB024 showing (a, b) polygonal aggregate of recrystallised cordierite wrapped by a sillimanite-biotite-bearing foliation (S1) which is in turn overprinted by coarse grained sillimanite prisms. (c, d) Irregular K-feldspar occurring between cordierite blasts representing crystallised partial melt. Base of image is 4.3 mm.

CORDIERITE-BIOTITE-QUARTZ PARAGNEISS (MB049)

Sample MB049 contains a tight F2 fold from psammo-pelitic paragneiss outcrop in the south of the study area. The F2 fold axis plunges 43° towards 094. In thin-section, folded layers (S1) comprise abundant cordierite, K-feldspar, biotite with lesser quartz and accessory rutile and ilmenite (Figure 4.3). Cordierite display anhedral grain shapes up 3.5 mm in length. Fine sillimanite inclusions in cordierite align parallel to the microfold limbs and is inferred to represent S1. Quartz forms interlobate to ameboid grains commonly featuring elongate sub-grain boundaries highlighted by slight sub-grain rotation recrystallisation. Quartz-quartz boundaries are typically sutured with small recrystallised grains developed along the migrating boundary. No new axial planar foliation was observed.

Fibrolitic sillimanite partly replaces S1 biotite, producing clusters of sillimanite. The lack of alignment with any foliation is consistent with post-D2 static growth of the sillimanite textures.

QUARTZITE (MB003)

Mineral modal abundances are Quartz = 81 vol.%, Biotite = 9 vol.%, Cordierite = 9 vol.%, Ilmanite <1 vol.%, Zircon/Monazite <1 vol.%

Inter-bedded with pelitic and psammitic layers are less-common quartzite horizons, up to 30 cm thick. In thin-section, quartz predominates and forms a seriate aggregate of interlobate grains displaying elongate sub-grain boundaries (Figure 4.4b centre). Quartz-quartz boundaries are highly irregular and show evidence of grain boundary migration recrystallisation. Minor biotite grains show elongated, anhedral grain shapes and are poorly-align to define a subtle foliation (S1). Anhedral cordierite displays typical yellow pleochroic haloes around small inclusions (Figure 4.4a top left, centre right) and a lesser internal strain than quartz grains (Figure 4.4b bottom centre). Fine grained fibrolite replaces cordierite along grain boundaries and partially replaces biotite. Accessory zircon and monazite typically occurs as rounded, ovoid grains and lesser elongate grains.

QUARTZ-K-FELDSPAR-SILLIMANITE-PHLOGOPITE PARAGNEISS (MB002)

Mineral modal abundances are Quartz = 39 vol.%, K-feldspar = 27 vol.%, Sillimanite = 26 vol.%, Phlogopite = 8 vol.%

Euhedral sillimanite occurs as elongate clusters that are up to 19 mm in length, which align with S1 in the field. Fine fibrolitic replacements produce radiating fans where they have partly or completely pseudomorphed anhedral phlogopite. Potassium-feldspar form anhedral grains with partially developed flame texture and commonly occur with rounded quartz, phlogopite and sillimanite (aligned with external) inclusions.

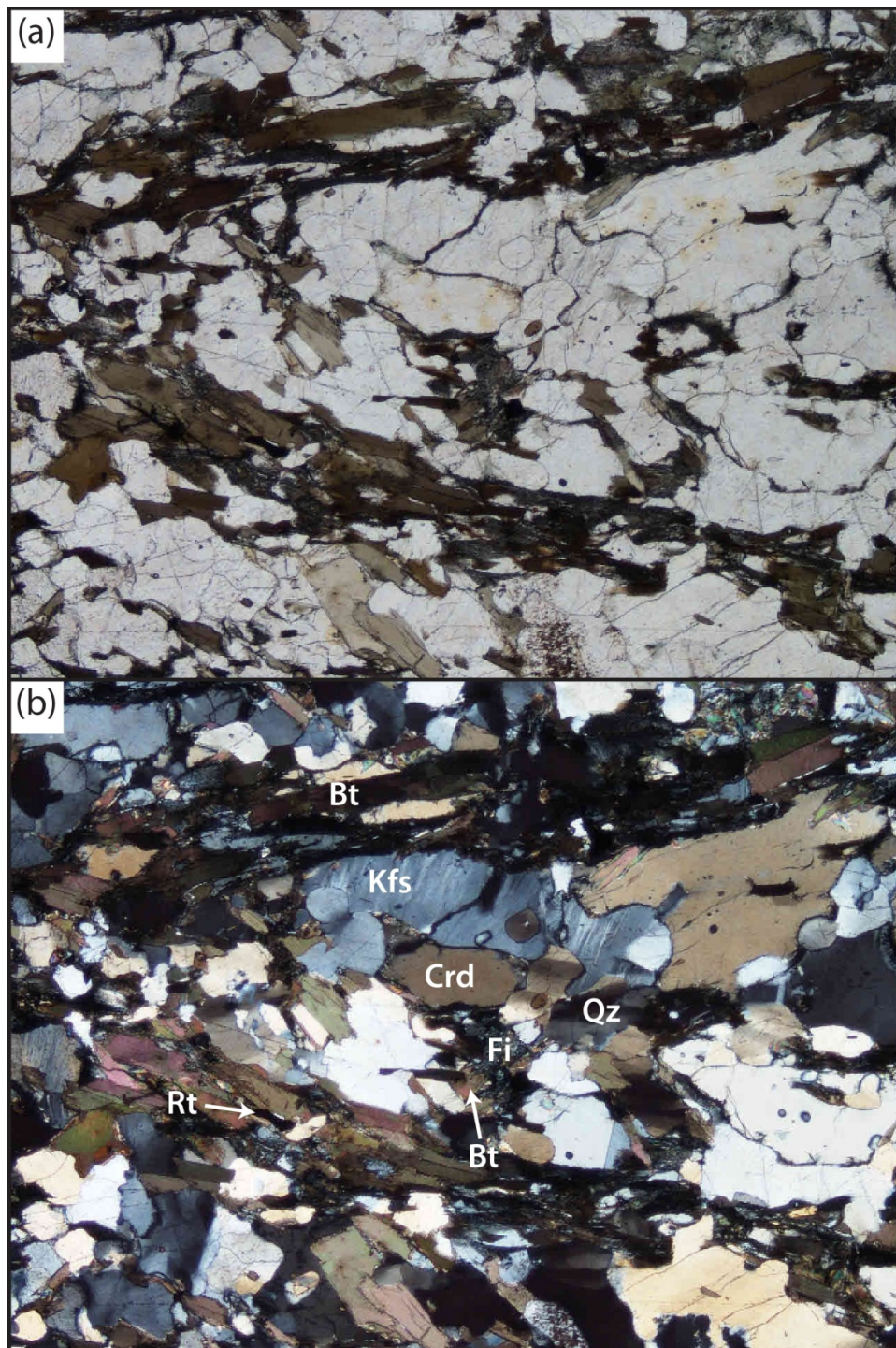


Figure 4.3 Photomicrograph of paragneiss sample MB049. The microstructure preserves a tight F2 fold that refolds the S1 assemblage. (a) PPL and (b) XPL. Base of image is 4.3 mm.

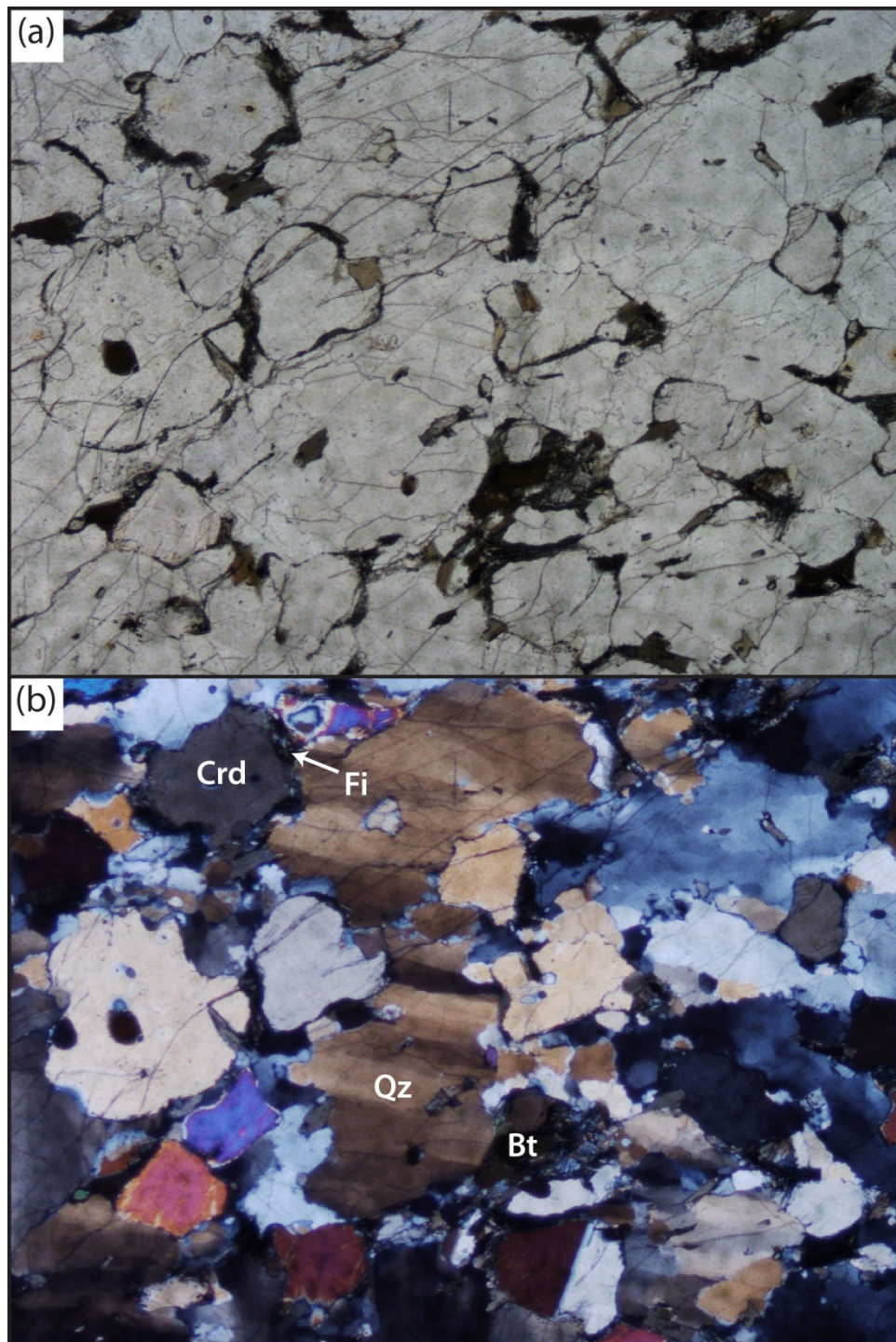


Figure 4.4 Photomicrograph of quartzite sample MB003 in (a) PPL and (b) XPL. Note the numerous elongate sub-grain boundaries present in quartz. Base of image is 4.3 mm.

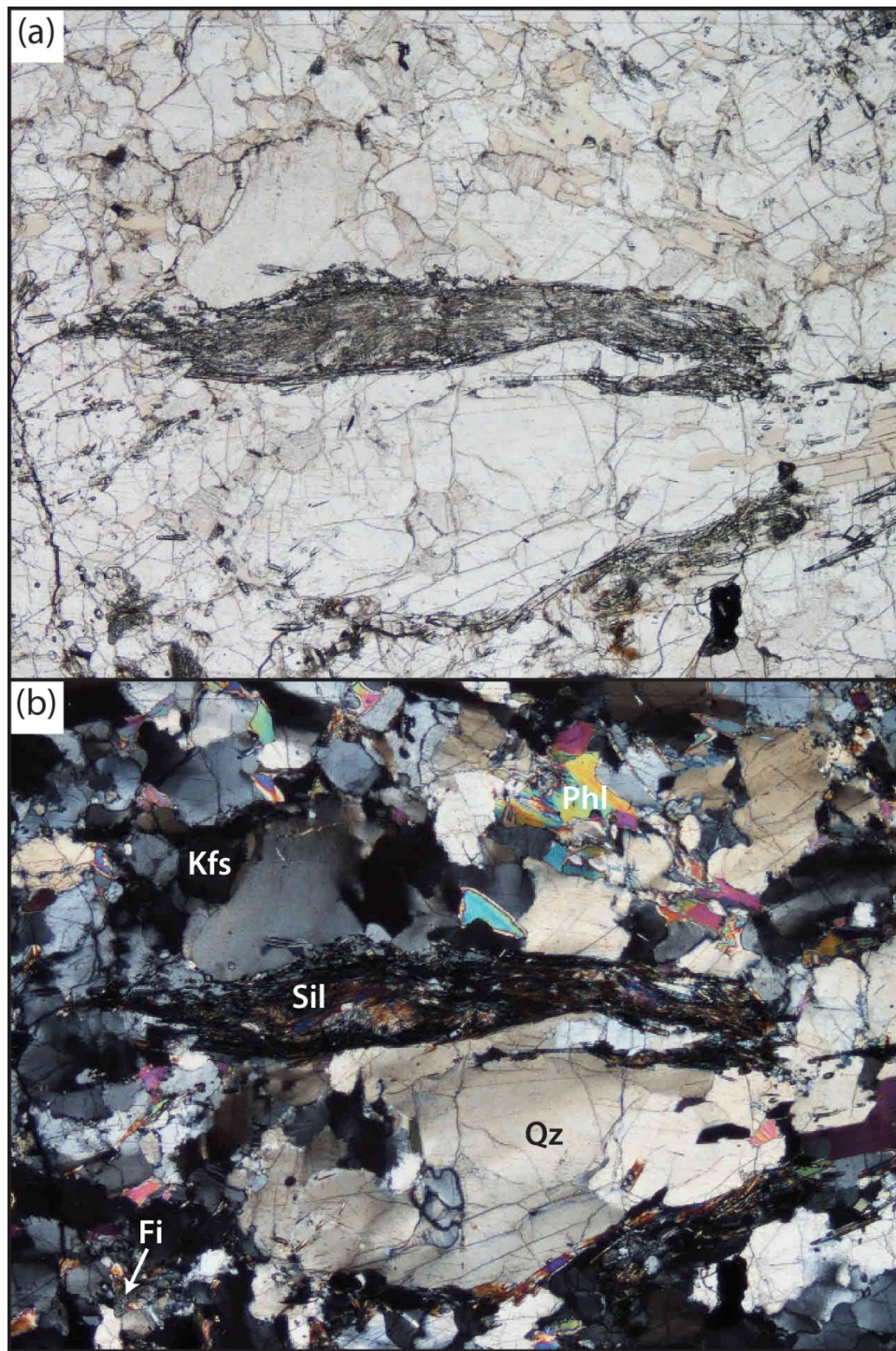


Figure 4.5 Photomicrograph of K-feldspar-quartz-sillimanite-phlogopite paragneiss (MB002) shown in (a) PPL and (b) XPL. Sillimanite forms elongate clusters aligning to define the S1 foliation. Phlogopite shows pale pleochroism (top centre-right). Base of image is 4.3 mm.

4.3.2 Calc-silicate Rocks

Two samples of calc-silicate rock collected from the outcrop in the centre of the study area are described. Sample MB010 was sampled on the northern margin of the unit, proximal to a D4 shear zone that bounds the outcrop. Sample MB009 was collected toward the centre of the outcrop.

TREMOLITE-BEARING DIOPSIDE-PLAGIOCLASE CALC-SILICATE GNEISS (MB009)

Mineral modal abundances of Diopside = 55 vol.%, Plagioclase = 30 vol.%, Calcite = 7 vol.%, Tremolite = 4 vol.%, Epidote 3 vol.%, Titanite = 1 vol.%

Diopside and plagioclase feldspar form a granoblastic texture (Figure 4.6a, b) with radiating splays of tremolite occurring interstitial between the diopside and feldspar (Figure 4.6c, d). Minor calcite, epidote and titanate occur locally in the thin section (Figure 4.6c, d).

CALCITE-SERPENTINE-SPINEL CALC-SILICATE GNEISS (MB010)

Mineral modal abundances are Serpentine = 44 vol.%, Calcite = 35 vol.%, Opq = 10 vol.%, Spinel = 6 vol.%, Rutile = 1 vol.%, Zircon = <1 vol.%.

In thin-section sample MB010 is dominated by ovoid clusters of serpentine that completely pseudomorph forsterite olivine in a calcite matrix (Figure 4.7). Twinned calcite forms a coarse grained mosaic. Calcite twin morphology varies from thick and tabular (Type II of Burkhard, 1993) to thick with serrated boundaries modified by dynamic recrystallisation (Type III of Burkhard, 1993). The serpentine forms a reticulated or 'mesh structure' as a consequence of its development along fractures in the original olivine crystal. Accessory phases include green spinel, ilmenite, rutile and zircon.

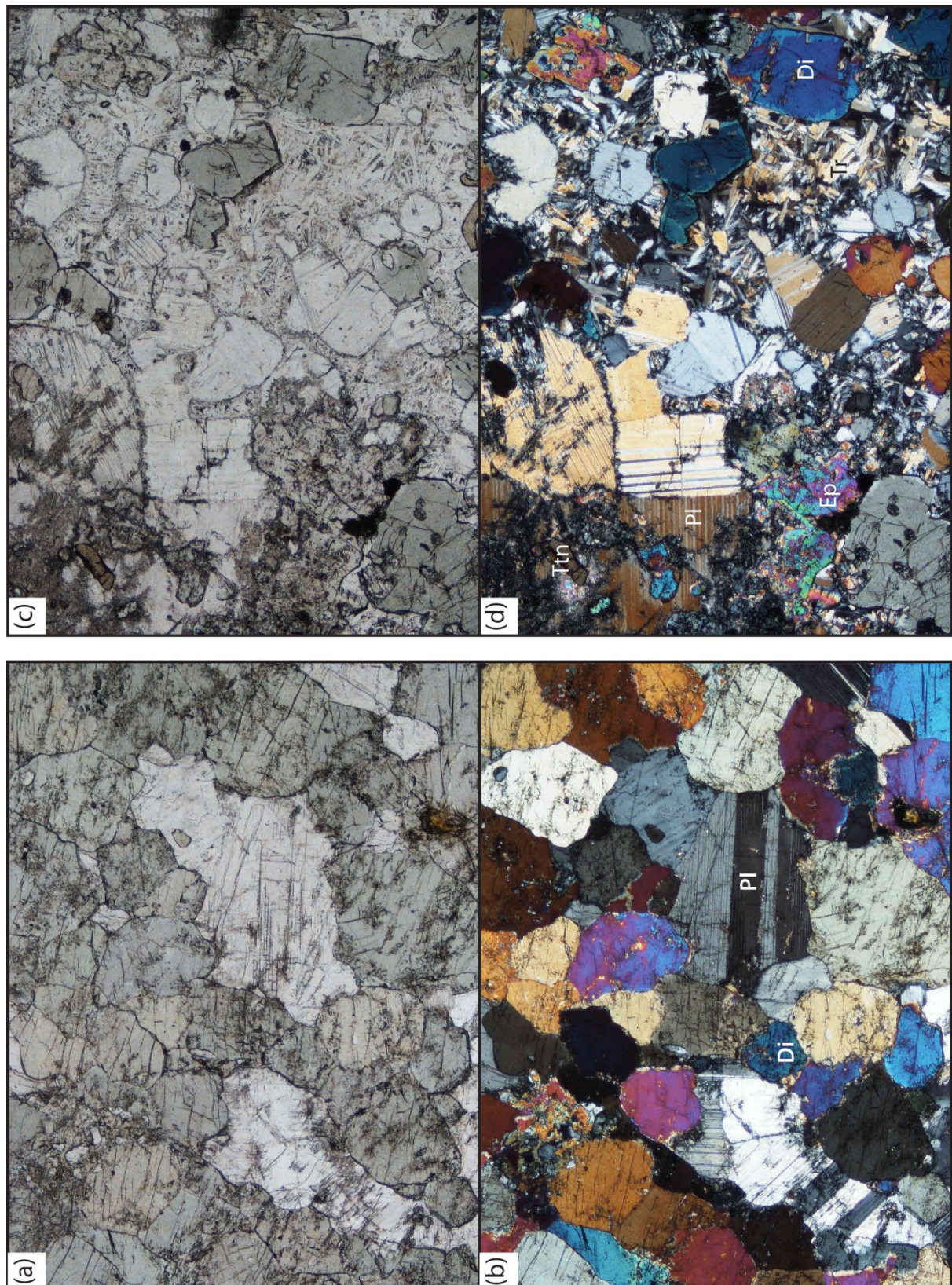


Figure 4.6 Photomicrographs of tremolite-bearing diopside-plagioclase calc-silicate gneiss (MB009) in different areas of the same thin-section. (a,c) and (b,d) show PPL and XPL views respectively. Base of image is 4.3 mm.

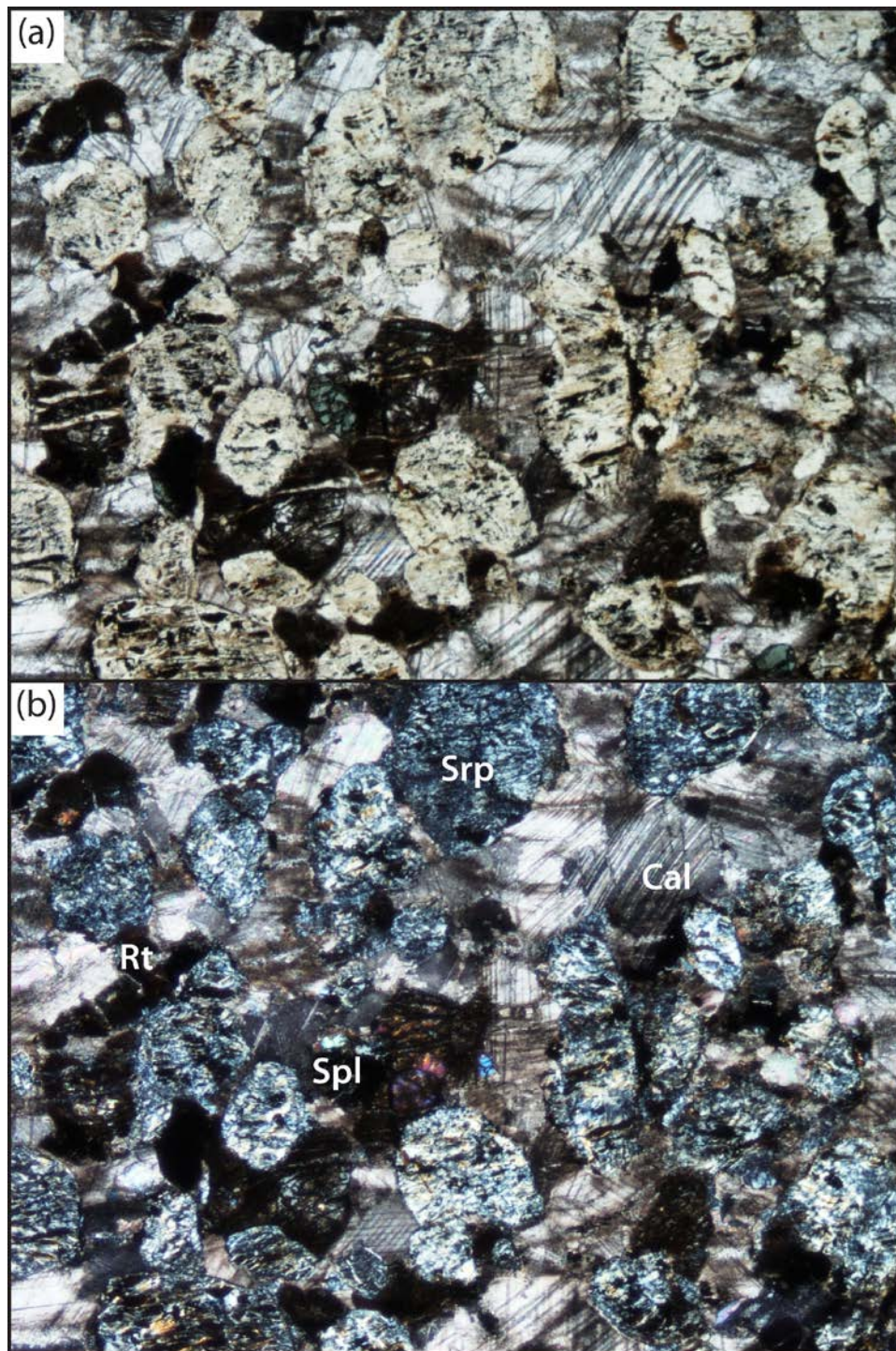


Figure 4.7 Photomicrographs depicting calcite-serpentine-spinel calc-silicate gneiss (MB010) under (a) PPL and (b) XPL. Base of image is 4.3 mm.

4.3.3 Quartz-Mica Schists—D4 Shear Zones

Three micaceous schists (samples MB038, MB043 and MB048) composing D4 high-strain shear zones were sampled along a steeply north dipping structure in the south of the study area and a fourth sample (MB037) was collected in the central north of the study area. In hand specimen, samples display a penetrative schistosity defined by aligned platy micas, namely biotite and muscovite. The foliation surface of sample MB038 contains locally aligned, though generally random, porphyroblasts of kyanite that are up to 17 mm in length. Sample MB048 shows subtle compositional banding, varying between biotite-rich and muscovite-rich folia up to a few millimetres thick. Samples MB037 and MB043 appear relatively homogeneous.

BIOTITE-CHLORITE-QUARTZ SCHIST (MB037)

Mineral modal abundances are Biotite = 54 vol.%, Chlorite = 23 vol.%, Quartz = 23 vol.%.

In thin-section, biotite and chlorite compose cleavage domains that alternate with polycrystalline quartz domains to define a zonal, disjunctive foliation termed S4 (Figure 4.8a, b). Chlorite shows pale green–yellow pleochroism and generally forms aligned aggregates of acicular crystals up to 1 mm in length, although chlorite-biotite intergrowths are common. Biotite forms euhedral crystals, with green–brown pleochroism, up to 2.5 mm in length. The 001 faces on both chlorite and biotite crystals control the morphology of quartz, which is interstitial, commonly resulting in elongated grain shapes no longer than 0.9 mm at the longest dimension. Quartz-quartz boundaries are generally irregular and approach 120° dihedral angles at triple junctions. Both biotite-chlorite and quartz domains are folded into a partially developed asymmetric crenulation cleavage (S5), which overprints the earlier disjunctive foliation.

QUARTZ-BIOTITE-KYANITE SCHIST (MB038)

Major mineral modal abundances are Quartz = 45 vol.%, Biotite = 38 vol.%, Kyanite = 16 vol.%. Accessory mineral modal abundances are Rutile = <1 vol.%, Zircon = <1 vol.%.

Sample MB038 (Figure 4.8c, d) displays an anastomosing disjunctive foliation defined by aligned aggregates of biotite and kyanite. Biotite displays elongate, euhedral habit in cleavage domains, and sub-hedral habit in quartz-rich. Kyanite forms elongated sub-hedral to anhedral grain shapes with abundant rounded fine inclusions. Individual crystals are generally less than 1.7 mm in length, with rare grains being up to 3.1 mm in length. Kyanite is preferentially distributed similar to biotite and is less abundant in quartz-rich domains, likely reflecting geochemical variation inherited from primary bedding rather than differentiation during foliation development. Quartz is extensively recrystallised, rarely showing evidence of accumulated internal strain (e.g. undulatory extinction). Quartz-quartz boundaries show gentle curvature, though straight boundaries are common. As with

sample MB037, the morphology of quartz is largely controlled by the 001 crystal faces of biotite, which in mica-rich domains results in elongated grain shapes and pinning structures at the ends of mica crystals. However, in mica-poor domains, quartz aggregates achieve a polygonal microstructure in which perfect 120° dihedral angles are common at quartz triple junctions.

BIOTITE-QUARTZ SCHIST (MB043)

Major mineral modal abundances are Biotite = 75 vol.%, Quartz = 22 vol.%. Accessory Rutile = 2 vol.%, Zircon = <1 vol.%.

Sample MB043 (Figure 4.9a, b) preserves a spectacular continuous foliation defined by euhedral–very elongate biotite generally between 0.5–0.7 mm in length. Quartz generally occurs as small elongate aggregates of grains disseminated within, but aligned with, the schistosity. Highly irregular quartz-biotite boundaries arise from the fine grain size of biotite, and consequently the small surface area of 001 crystal faces, resulting in multiple pinning structures along the quartz boundary that may appear irregular. Quartz-quartz boundaries are interlobate, commonly bulging into adjacent grains. The habit of accessory rutile varies from elongate to ovoid and aligns with biotite in the continuous foliation. An incipient crenulation overprint produced minor kinking (F5) of the dominant schistosity (S4, Figure 4.9a, b).

QUARTZ-BIOTITE-MUSCOVITE SCHIST (MB048)

Major mineral modal abundances are Quartz = 44 vol.%, Biotite = 33 vol.%, Muscovite = 18 vol.%, Ilmanite = 5 vol.%. Accessory Zircon = <1 vol.%.

Sample MB048 (Figure 4.9c, d) differs from the earlier schist samples by the presence of very elongate muscovite (commonly *ca.* 1.7 mm in length) that is intergrown with euhedral biotite to define mica-rich domains in an anastomosing, disjunctive foliation. Quartz-quartz boundaries are curved to irregular and make a 90° angle with 001 crystal faces of mica. Subtle undulatory extinction highlights sub-grain boundaries in many quartz crystals, though this is more common in larger grains (up to 1.6 mm at the longest dimension). Many quartz grains contain subhedral to rounded inclusions of biotite and/or accessory zircon commonly aligned to the external foliation.

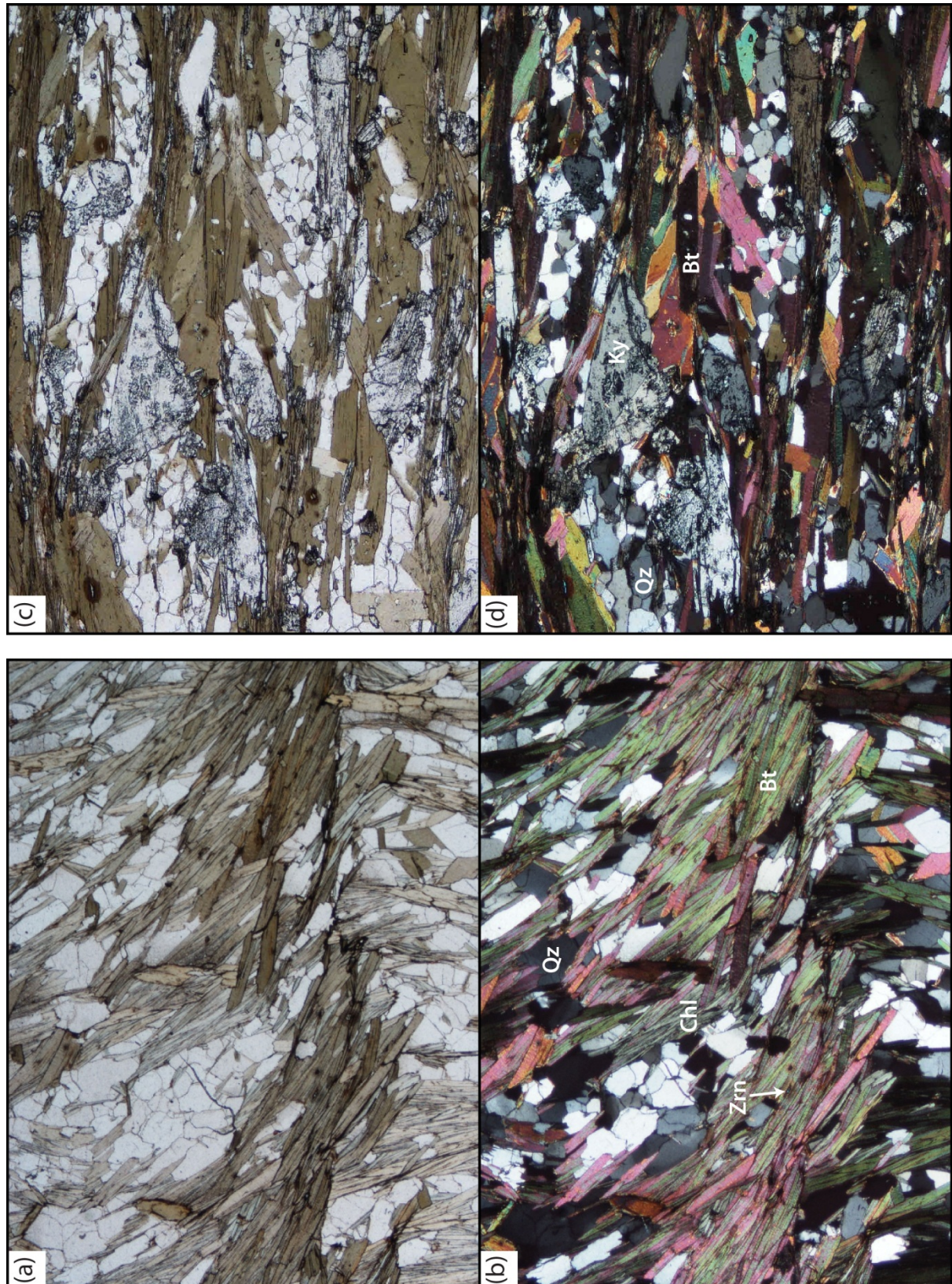


Figure 4.8 Photomicrographs (a) and (b) depict biotite-chlorite-quartz schist (MB037) under PPL and XPL respectively. Photomicrographs (c) and (d) depict quartz-biotite-kyanite schist (MB038) under PPL and XPL respectively. The longest dimension of individual photomicrographs is 4.3 mm.

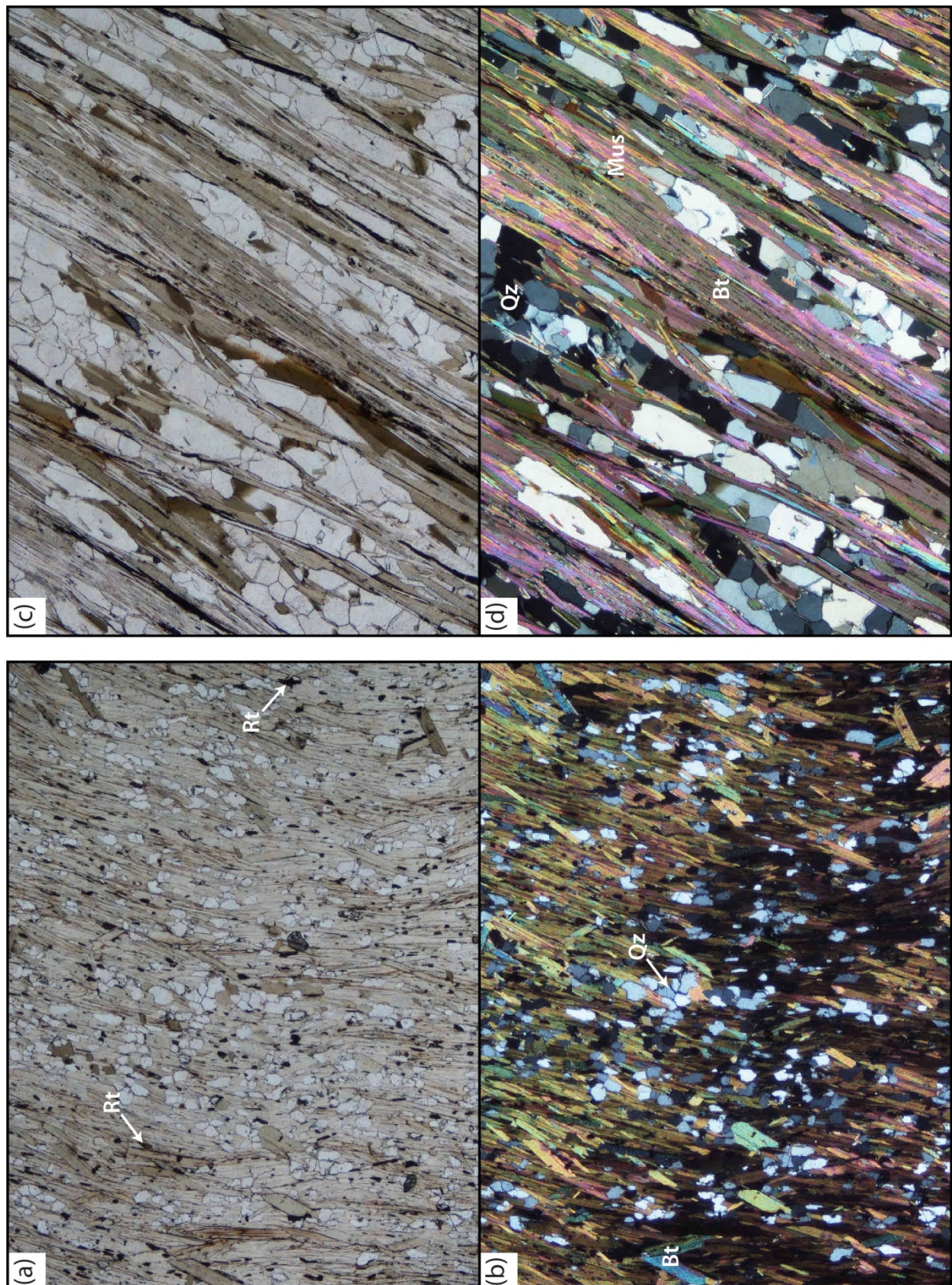


Figure 4.9 Photomicrographs (a) and (b) depict biotite-quartz schist (MB043) under PPL and XPL respectively. Photomicrographs (c) and (d) depict quartz-biotite-muscovite schist (MB048) under PPL and XPL respectively. The longest dimension of individual photomicrographs is 4.3 mm.

4.4 METAIGNEOUS PROTOLITHS

4.4.1 Felsic Orthogneiss

K-FELDSPAR AUGEN ORTHOGNEISS (BOOTHBY ORTHOGNEISS; MB007)

Mineral modal abundances are Orthoclase = 30 vol.%, Plagioclase = 27 vol.%, Quartz = 22 vol.%, Microcline = 9 vol.%, Biotite = 9 vol.%, Ilmanite = 1 vol.%, Zircon = <1 vol.%.

Sample MB007 is a coarse grained K-feldspar augen orthogneiss representative of Boothby Orthogneiss in the study area. In hand sample, MB007 displays a penetrative S2 gneissosity defined by alternating biotite and feldspar rich layers (Figure 3.5). Igneous K-feldspar megacrysts define lenticular augen within the foliation plane. In thin-section, anhedral K-feldspar occur as strongly flame-textured orthoclase and microcline up to 4.0 mm long in a groundmass of interlobate quartz and subhedral biotite (Figure 4.10c, d). Myrmekite texture is common and produces embayments along K-feldspar boundaries (Figure 5.10d centre). Plagioclase is less abundant than K-feldspar but display better formed rectangular crystal shapes commonly preserving complex igneous twins (Figure 5.10a, b). Quartz grains show varying degrees of internal strain ranging from grains with abundant sub-grain boundaries to recrystallised grains approaching 120° triple junctions with adjoining grains.

TOURMALINE-BEARING PLAGIOCLASE-QUARTZ-K-FELDSPAR-BIOTITE ORTHOGNEISS (MB036)

Mineral modal abundances are Plagioclase = 38 vol.%, Quartz = 27 vol.%, K-feldspar = 17 vol.%, Biotite = 8 vol.% Sillimanite = 7 vol.%, Tourmaline = 4 vol.%, Zircon = <1 vol.%, Rutile = <1 vol.%.

In hand specimen, sample MB036 is a sugary textured, leucocratic, orthogneiss with *ca.* 1 cm spotty patches of dark green coloured mineral. In thin-section, plagioclase, quartz, K-feldspar and biotite form a seriate aggregate of interlobate grains. Green-brown biotite is domainal, denoting the ‘spotty’ texture observed in hand specimen, and is partly to completely pseudomorphed by splays of euhedral sillimanite. Tourmaline occurs randomly throughout the thin-section as irregular shaped grains or partly recrystallised aggregates. Igneous plagioclase is preserved, although not to the extent observed in sample MB007, forming partly recrystallised grains up to 2.6 mm in length.

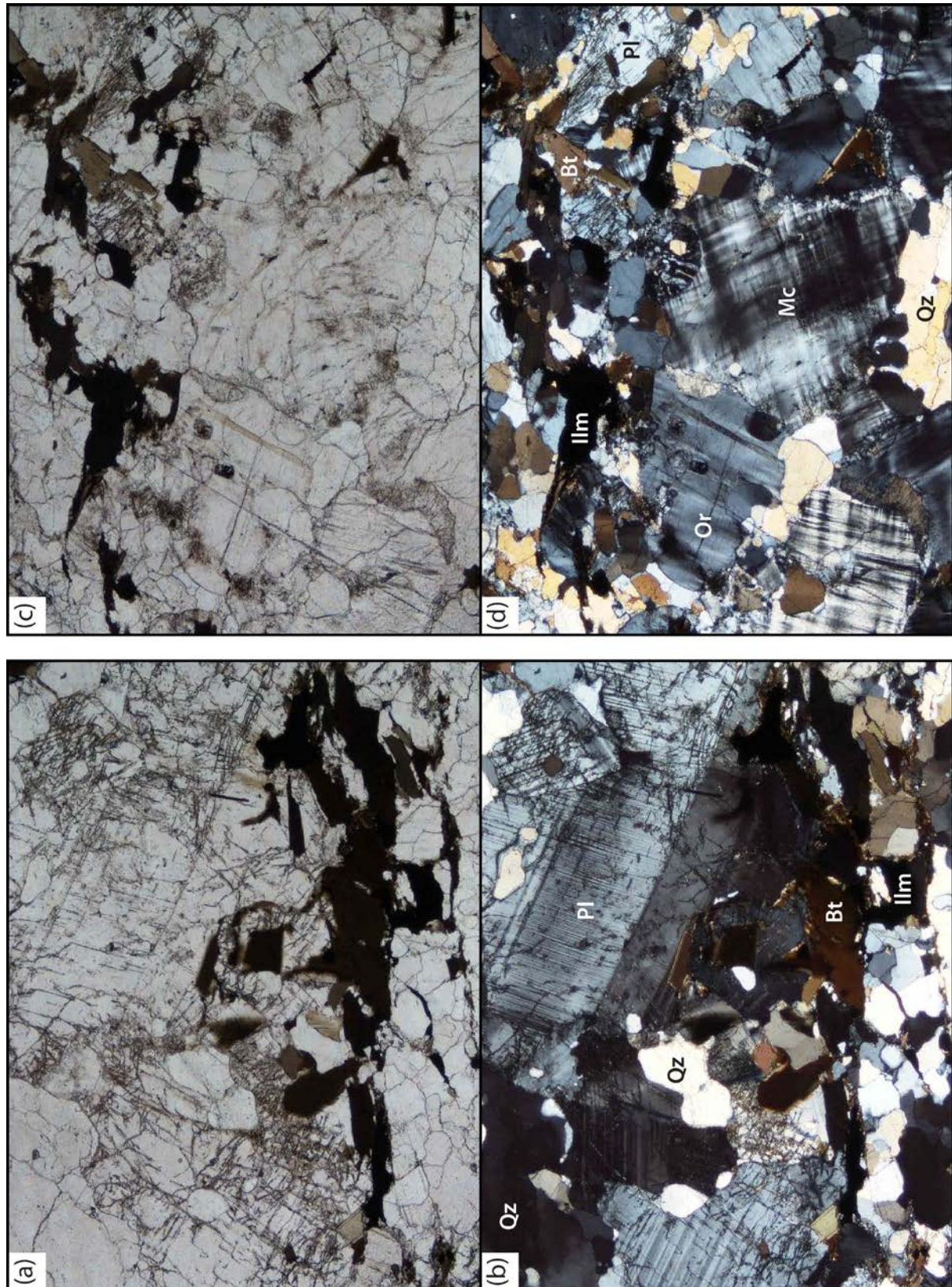


Figure 4.10 Photomicrograph of K-feldspar augen orthogneiss (MB007) shown in (a, c) PPL and (b, d) XPL. Igneous plagioclase crystals are preserved suggestion incomplete recrystallisation of the protolith granitoid. Myrmekite is developed along microcline grain boundaries. Base of image is 4.3 mm.

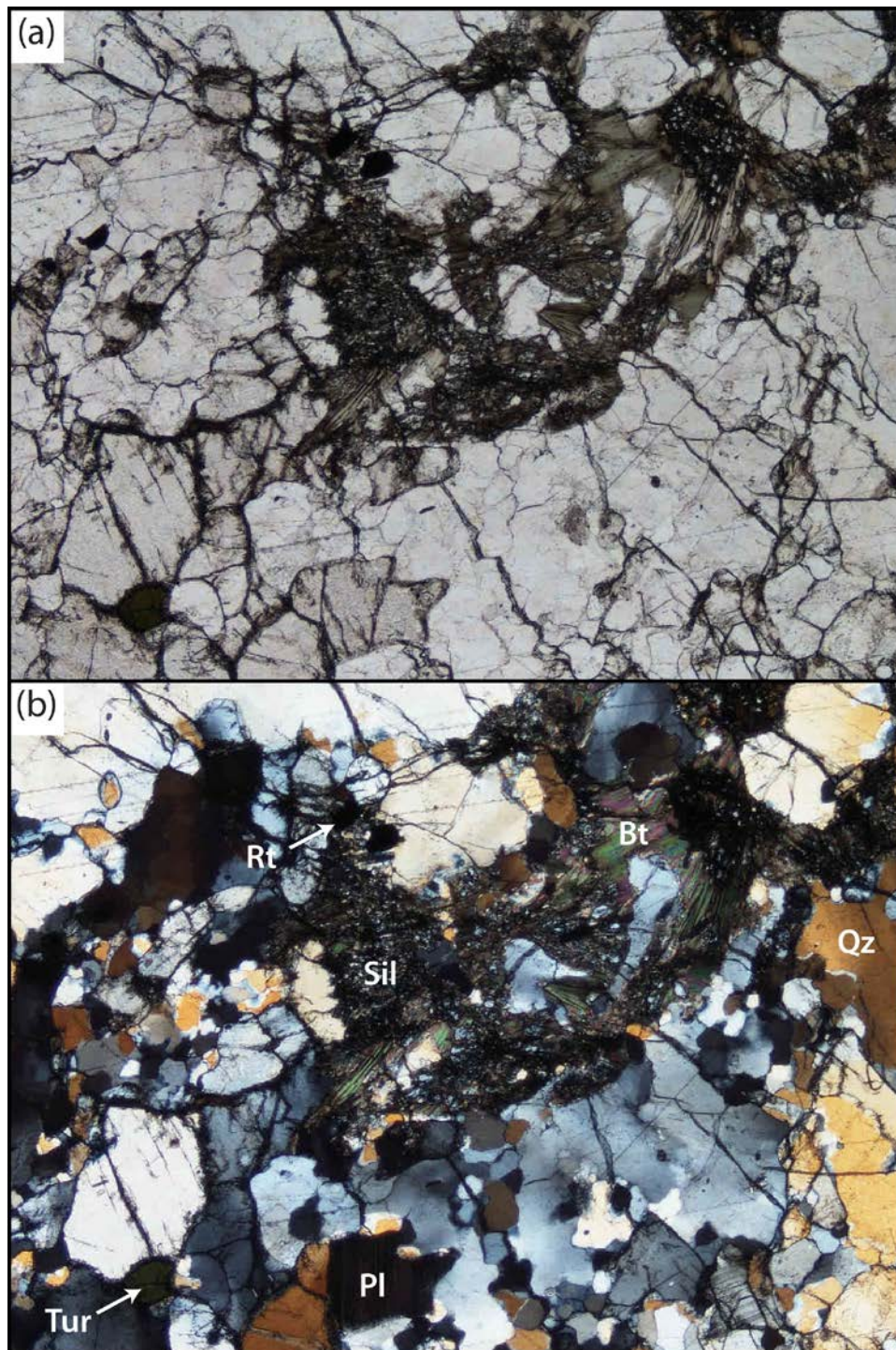


Figure 4.11 Photomicrograph of tourmaline-bearing plagioclase-K-feldspar-biotite orthogneiss (MB036) shown in (a) PPL and (b) XPL. Biotite is partially pseudomorphed by sillimanite. Base of image is 4.3 mm.

4.4.1 Mafic Orthogneiss

PLAGIOCLASE-HORNBLende-ORTHOpyroxene-BIOTITE GNEISS (MB035)

Mineral modal abundances of Plagioclase = 35 vol.%, Hornblende = 21.8 vol.%, Orthopyroxene = 15 vol.%, Biotite = 12 vol.% Quartz 6 vol.%, Ilmanite = 1 vol.%, Zircon = <1 vol.%.

Mafic gneiss was sampled from several elongate pods occurring in paragneiss outcrop north of the microwave tower. Plagioclase grains produce a granoblastic microstructure (Figure 4.12). Orthopyroxene is skeletal to porphyroblastic with inclusions of mainly plagioclase with lesser hornblende and biotite (Figure 4.12). Biotite is foxy-red-brown and forms sub-hedral grains. Hornblende and biotite define a well-developed gneissosity (S1). Ilmenite is a common accessory throughout the sample.

4.4.2 Mesomylonite—D4 Mylonite Shear Zone

Sample MB004 was taken from a steeply south dipping mylonite zone (Figure 3.11) developed in Boothby Orthogneiss in the north of the study area. The mylonitic foliation plane contains elongated K-feldspar aggregates defining a mineral stretching lineation plunging south.

In thin-section, microcline (as individual or less common aggregates) and lesser orthoclase compose highly eroded porphyroclasts in a fine matrix of recrystallised quartz, feldspar, biotite and muscovite. Microcline displays characteristic tartan-twinning whilst orthoclase displays variably developed deformation twins and flame texture. Myrmekitic intergrowths replace microcline to varying degrees along some grain boundaries. Biotite-muscovite domains and polycrystalline quartz ribbons alternate to define the mylonitic foliation (Figure 4.13). Consistent σ -type asymmetric strain shadows of quartz, or biotite and muscovite, or both, indicate a south over north (reverse) sense of movement along the mylonite zone. The percentage of matrix (*ca.* 70%) to porphyroclasts (*ca.* 30%) indicates the sample is a mesomylonite.

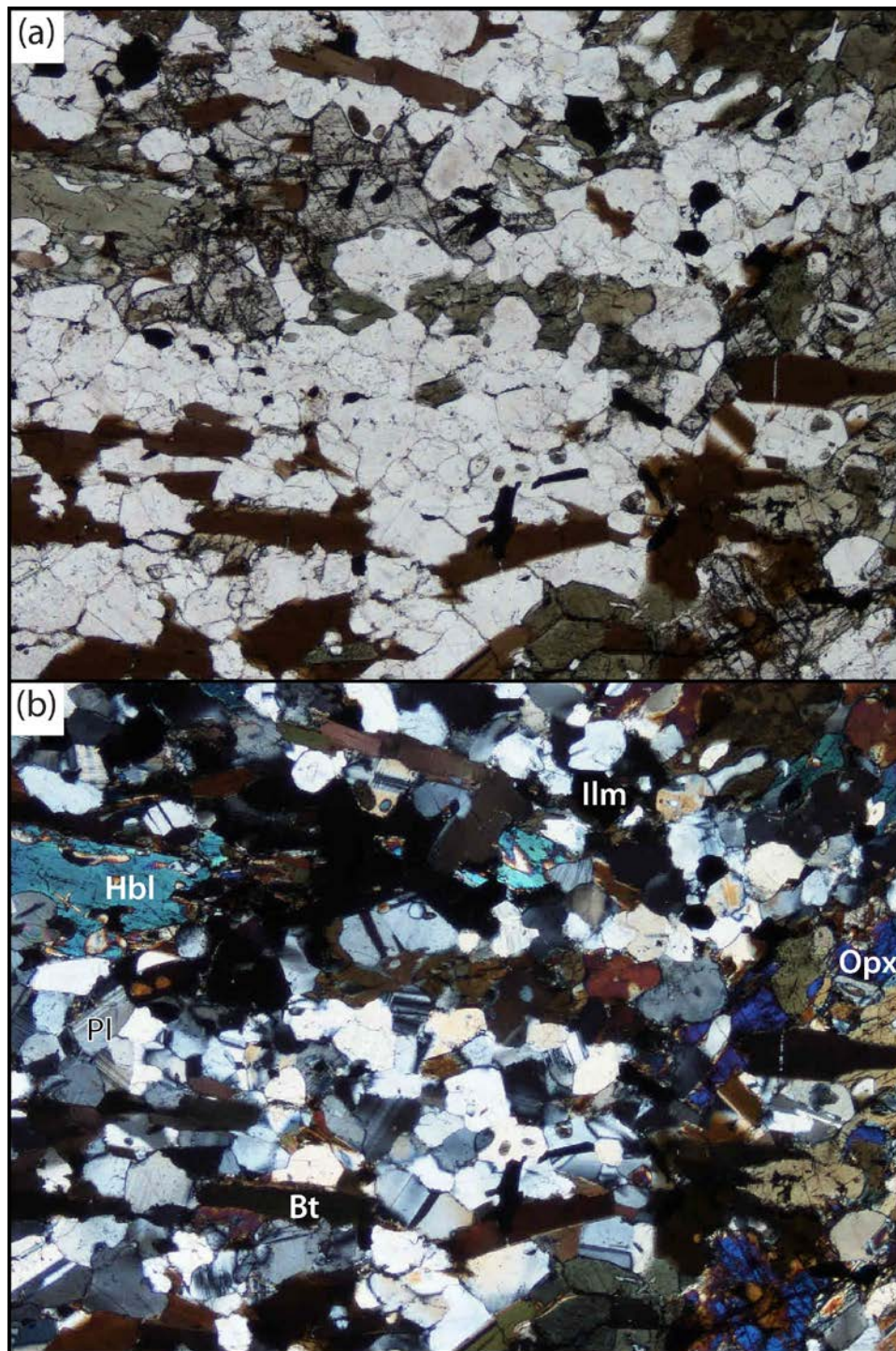


Figure 4.12 Photomicrograph of plagioclase-hornblende-orthopyroxene-biotite gneiss (MB035) shown in (a) PPL and (b) XPL. Orthopyroxene is skeletal with inclusions of mainly plagioclase with lesser hornblende and biotite. Base of image is 4.3 mm.

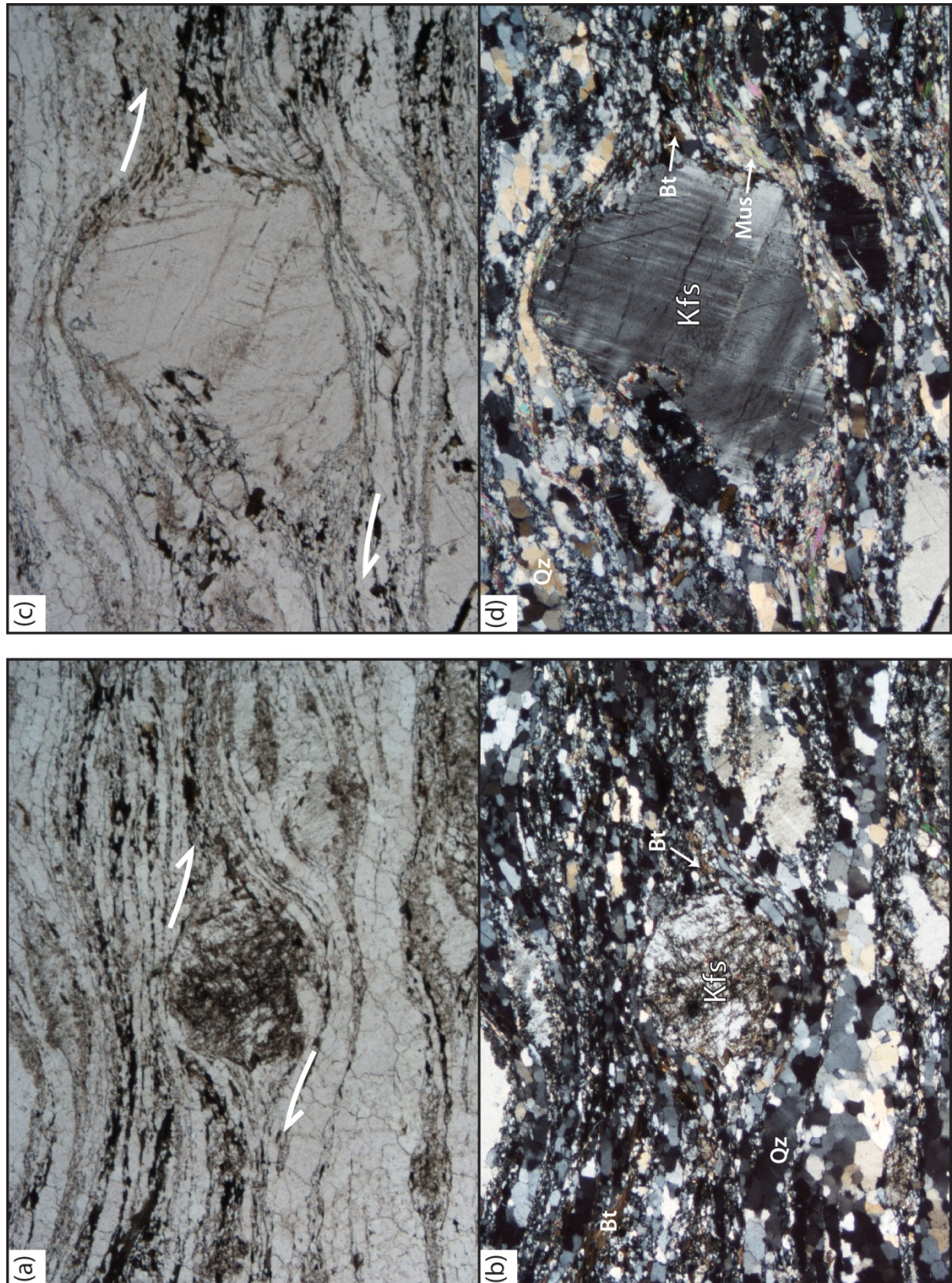


Figure 4.13 Photomicrograph of mesomylonite shear zone (MB004) shown in (a, c) PPL and (b, d) XPL. Asymmetric strain shadows developed on K-feldspar porphyroclasts indicate a reverse sense of movement along the shear plane. Base of image is 4.3 mm.

4.5 DISCUSSION

On the basis of the S1 assemblage including sillimanite and cordierite in pelitic paragneiss and orthopyroxene in mafic gneiss, D1 occurred at granulite facies conditions (*ca.* 750°C) in the shallow crust (4.4 kbar; Clarke & Powell, 1991; Dirks *et al.*, 1991). Stability of the S1 assemblage during transposition into S2 and folding by F2 and F3 may be interpreted two ways. Firstly, that the P–T conditions during later events were the same, and there was no need for the M1 paragenesis to re-equilibrate. Alternatively, sufficient dehydration of the bulk rock was achieved during progressive M1 metamorphism that re-equilibration was not possible during later events. The post-F3 sillimanite pseudomorph textures after biotite and recrystallisation of cordierite to a polygonal aggregate are consistent with similar high-grade conditions persisting throughout the structural scheme and outlasting pervasive deformation.

Schists sampled from paragneiss outcrop in the south of the study area are characterised by Bt+Qz±Mus±Ky±Rt assemblages, which indicate amphibolite facies conditions during shear zone development. This is consistent with P–T estimates of Dirks *et al.* (1991) who estimated that kyanite+staurolite-bearing shear zones cross-cutting metapelites in the Mount Boothby area formed at 550–600°C and 5–6 kbar. The assemblage has undergone rapid recrystallisation in the deforming shear plane. This is likely to result from high fluid flow assisting recrystallization, which is consistent with the high mica content of the rocks and quartz veins localised along the shear plane, observed in the field. Further evidence of fluid flow along D4 shears is the serpentinization of olivine in sample MB010, which was sampled proximal to a shear zone on the northern margin of calc-silicate rock outcrop.

The preservation of some igneous microstructure in sample MB007 is consistent with only partial recrystallization of the granitoid protolith during D2. The dominance of S2 in the field is in stark contrast to the limited development of a new S2 assemblage in the paragneiss samples at thin section scale. These relationships suggest that S2 in the paragneiss is largely a folded and transposed S1, consistent with a lower strain nature of S2 in the orthogneiss. The mineral assemblage of S2 in the Boothby Orthogneiss is not diagnostic of metamorphic grade. However, the muscovite-bearing D4 mylonite zones cutting orthogneiss are consistent with the amphibolite-grade shear zones in the paragneisses.

5. U–PB ZIRCON GEOCHRONOLOGY BY LA–ICPMS

5.1 INTRODUCTION

The U–Pb method of dating is centred on three independent radioactive decay series involving parent isotopes ^{238}U , ^{235}U and ^{232}Th that undergo combined α - and β -decay to daughter isotopes ^{206}Pb , ^{207}Pb and ^{208}Pb respectively (Harley & Kelly, 2007). U^{4+} (ionic radius = 1.05Å) and Th^{4+} (ionic radius = 1.10Å) readily camouflage for Zr^{4+} (ionic radius = 0.87Å) in the crystal lattice of zircon (ZrSiO_4). Pb^{2+} (ionic radius = 1.32Å) is largely excluded from the zircon lattice during crystal formation, and so Pb values measured in zircon are mostly radiogenic in origin (Faure & Mensing, 2005). Furthermore, zircon is resistant to isotopic re-equilibration at high-grade metamorphic and even magmatic temperatures, commonly allowing multiple episodes of crystal growth (or consumption) to be recorded in a single grain (Davis *et al.* 2003).

Zircon most commonly occurs as an accessory phase in acidic igneous rocks and metamorphic rocks. However, sedimentary rocks may also contain a significant fraction of zircon derived from weathered igneous and metamorphic protosources. Therefore, detrital zircon in sedimentary rocks and sediments is likely to record the magmatic and orogenic histories of crustal protosources that contributed to the sediment load (Qian *et al.*, 2012).

The youngest U–Pb ages of zircon grains in populations of detrital zircon are commonly used to constrain maximum depositional ages of stratigraphic units and establish basic stratigraphic superposition (Dickinson & Gehrels, 2009). This approach is especially valuable for Precambrian strata lacking datable biota or volcanic horizons (e.g. Phillips *et al.*, 2006; Claoué-Long *et al.*, 2008; Jones *et al.*, 2009). When detrital zircon geochronology is coupled with geochronology of cross-cutting igneous rocks, both maximum and minimum constraints are established for the age range over which the sediments were deposited (Fedo *et al.*, 2003).

The maximum depositional age can be determined using (i) the youngest individual detrital zircon grain age, or (ii) the youngest coherent population of detrital zircon grain ages. The youngest individual age approach is cautioned against in high grade metasedimentary rocks due to the possibility of detrital grains experiencing Pb-loss during orogenesis or new metamorphic growth (Nelson, 2001). In these rocks, the youngest population of ages ($n \geq 3$) is a more conservative approach (Dickinson & Gehrels, 2009).

This chapter documents U–Pb geochronology of zircon grains liberated from three samples collected in the study area. Each of the three samples has been selected to assess a specific aspect of the geochronological character of the Aileron Metamorphics as outlined in section 5.1.1.

5.1.1 Sample Description

Sample MB003 was taken from a *ca.* 30cm thick quartzite horizon in paragneiss outcropping in the southwest of the study area (Figure 1.1, Figure 4.4). It is stratigraphically conformable with adjacent psammitic and pelitic horizons and continuous along strike. Therefore, MB003 is interpreted to be the metamorphosed equivalent of a mature quartz-arenite, and considered prospective for detrital zircon representing the provenance of the Aileron Metamorphics. Appealingly, features indicative of migmatization or partial melting were absent from the quartzite outcrop, limiting the potential for dissolution of detrital grains in partial melt.

The enveloping post-D1 Boothby Orthogneiss (sample MB007, Figure 1.1, Figure 4.10) was sampled at a location *ca.* 200m immediately west of the study area. Here the local strain effects of the D2 and D3 events are more subtly developed. It is anticipated that the lower degree of strain expressed in the sample may render the U–Pb isotopic system of any magmatic zircon present relatively undisturbed by these events.

Sample MB033 (Figure. 1.1) is a post-D3 Kfs–Qz–Pl diatexite taken from paragneiss outcropping in the south of the study area. At this location diatexite has developed along, as well as across the earlier high grade fabrics and is unfoliated. Although it is likely that the diatexite intruded its current position, it is anticipated that zircon entrained in resititic selvages or having crystallized from the melt will preserve the cooling age of LPHT metamorphism in the region, and so constrain the timing of earlier fabrics.

5.2 METHODS

Sample preparation, imaging and laboratory geochemical analysis was conducted within the Geochemical Analysis Unit (GAU) at the Australian Research Council National Key Centre for Geochemical Evolution and Metallogeny of Continents (GEMOC), Macquarie University, Sydney.

5.2.1 Zircon Liberation & Separation

Approximately 1 kg of each sample selected for U–Pb zircon geochronology was manually reduced to a feed size $<3\text{ cm}^3$ prior to processing. Zircon was liberated from each sample using a selFrag Lab S1.1 Laboratory System, discharging 115.2 kV at an average 3.2 Hz. The disaggregated sample was then passed through 600 μm and 210 μm nylon sieves, separating the sample into three size-fractions; a $>600\text{ }\mu\text{m}$ fraction; a 600–210 μm fraction; and a $<210\text{ }\mu\text{m}$ fraction, of which the 600–210 μm and $<210\text{ }\mu\text{m}$ size fractions were further processed. Each retained size-fraction was separated into heavy mineral separates (HMS) and light mineral separates (LMS) using a lotok pan. Magnetic minerals were removed from the HMS by hand using REE-magnets and the non-magnetic fraction retained for further processing. Zircon was concentrated from the non-magnetic HMS using a Frantz LB-1 Magnetic Barrier Laboratory Separator in a staged approach of increasing magnetic field-strength summarised in Table 5.1.

Table 5.1 Summary of magnetic field settings employed during zircon concentration by Frantz Magnetic Barrier Laboratory Separator.

Pass	Mean Voltage (V)	Mean Current (A)
1	01.60	00.00
2	15.70	00.23
3	25.40	00.38
4	67.10	01.03

Artificial biasing of detrital zircon U–Pb age spectra due to magnetic barrier separation techniques has been well documented by Sircombe & Stern (2002). These authors concluded that a compromise between broad representation and analytical efficiency (avoiding discordant and thus unreliable results) could be achieved by using a Frantz setting of 1.8A and 10° side-slope. A more conservative Frantz setting of *ca.* 1A and 10° side-slope was adopted in this study.

The diamagnetic separate was then processed by heavy-liquid separation using a sodium polytungstate ($3\text{Na}_2\text{WO}_4\cdot 9\text{WO}_3\cdot \text{H}_2\text{O}$) solution with a specific gravity of ~ 2.95 ; the sinking mineral fraction was then inspected for zircon. Zircon grains representing the range of morphologies

present in each sample were hand-picked and mounted in epoxy resin discs before being polished so as to expose the central portions of the grains.

5.2.2 Cathodoluminescence (CL) Microscopy

Cathodoluminescence is a standard technique used to assess the internal structure of zircon grains and to guide site selection for analysis by laser ablation techniques. Zircon grain mounts were carbon coated prior to imaging to prevent charging of the grain surface.

CL imaging of zircon grains was conducted using a Zeiss EVO|MA15 Scanning Electron Microscope (SEM) operating at 20 kV, with a beam current of 100 μ A. The magnification, focus, brightness and contrast were optimised for each. Representative grains to be incorporated into the thesis body were captured at higher resolution.

Individual zircon characteristics including dimensions, aspect ratio (length/width), morphology, and internal structure were recorded and representative grains selected for isotopic analysis.

5.2.3 U–Pb Zircon Geochronology by Laser Ablation–Inductively Coupled Plasma Mass Spectrometry (LA–ICPMS)

U–Pb isotope analysis of zircon was conducted using an Agilent 7700 series inductively coupled plasma mass spectrometer (ICPMS) attached to a Photon-Machines Analyte Excite laser ablation (LA) system. Due to maintenance requirements, the abovementioned LA system was temporarily replaced by a New Wave Research UP-213 LA system, which was used to analyse 62 unknowns from sample MB003. Data acquisition parameters used during analysis are summarised in Table 5.2.

Prior to analysis, a pre-ablation of the target area was conducted to remove isotopic contaminants from the sample surface. Pre-ablation included 5 pulses of the target area with a 50 μ m spot size, followed by a 25 second gas blank to clear the instrument. Analysis included 60 seconds of background signal prior to ablation followed by 600 pulses over 120 seconds (5 Hz) of signal acquisition. Samples were ablated using a spot size of 30–40 μ m. A typical run included two analyses of the external calibration zircon standard GJ, one analysis of the reference zircon standard 91500, one analysis of the reference standard Mud Tank, fifteen analyses of unknowns, followed by a further two analyses of the calibration zircon standard GJ.

Initial interrogation of raw scan-by-scan data was conducted using GLITTER 4.41 (Griffin *et al.*, 2008) data reduction software. Further refinement of the dataset was done using Microsoft EXCEL data worksheets developed for Terranechron® analysis (Belousova pers. comm.). Isotopic

lead compositions were corrected for the influence of common lead and lead loss using a Microsoft *EXCEL* template based on the algorithm of Andersen (2002).

Table 5.2 Summary of operating conditions and data acquisition parameters used during U-Pb analysis by LA-ICPMS.

LA system		
Make	Photon Machines	New Wave Research
Model	Analyte Excite	UP-213
Type	Excimer (excited dimer)	Nd: YAG (solid-state)
Wavelength	193 nm	213 nm
Beam diameter (spot size)	30-40 μm	30-40 μm
Repetition rate	5 Hz	5 Hz
Fluence	~14.26 J/cm ⁻²	~7.12 J/cm ⁻²
ICPMS system		
Make	Agilent	
Model	7700 series	
Type	Quadrupole	
Gas flows:		
Plasma (Ar)	15 L/min	
Carrier (He)	0.8 L/min	
Make-up (Ar)	1 L/min	
Data Acquisition Parameters		
Data acquisition protocol	Time-resolved analysis	
Standards		
External calibration standard	GJ	
Primary reference standard	91500	
Secondary reference standard	Mud Tank	
Pre-ablation	5 pulses, 50 μm spot size, followed by 25 second gas blank to clear the instrument.	
Background signal time	60 seconds	
Data acquisition signal time	120 second (600 pulses)	
Isotopes determined	²⁰⁴ Pb, ²⁰⁶ Pb, ²⁰⁷ Pb, ²⁰⁸ Pb, ²³² Th, ²³⁸ U	
Dwell time per isotope (ms)	10, 15, 30, 20, 10, 15 respectively	
Data reduction software	GLITTER 4.41	

External calibration standard GJ (Jackson *et al.*, 2004) was used to correct for elemental fractionation. Analytical accuracy was monitored using internal reference standards 91500 (Wiedenbeck *et al.*, 1995) and Mud Tank (Black & Gulson, 1978). Values obtained during this study are within statistical error of published values for these reference materials as shown in Table 5.3.

Table 5.3 Summary of published and observed values for external-calibration and reference standards obtained during LA–ICPMS analysis of samples documented in this study. Measured values are weighted average age determinations in isoplot.

Standard	Reported Value (Ma)		Measured Value (Ma)		
	Mean Age	1 σ	Mean Age	1 σ	<i>n</i>
GJ $^{206}\text{Pb}/^{238}\text{U}$ Age (Jackson <i>et al.</i> , 2004)	600.39	0.65	600.5	1.7	50
91500 $^{207}\text{Pb}/^{206}\text{Pb}$ Age (Wiedenbeck <i>et al.</i> , 1995)	1065.40	0.30	1063	14	19
Mud Tank $^{206}\text{Pb}/^{238}\text{U}$ Age (Black & Gulson, 1978)	732	5	727	4.4	12

5.2.4 Visualisation of Age Data

Detrital age data has conventionally been represented using the Probability Density Plot (PDP), a probability density function, which is fundamentally governed by the analytical precision of each age measurement. The practical and theoretical functionality of the PDP (in the context of detrital age distributions) has been strongly criticised by Vermeesch (2012) who demonstrated that in certain situations the emphasis of analytical precision could result in unclear data representation and lead to misguided interpretation. Vermeesch (2012) proposed the Kernel Density Estimator (KDE) as a more statistically robust alternative for visualising detrital age distributions. The KDE is a probability density function that is governed by local probability density (rather than analytical precision).

In this study, DensityPlotter 2.0 (Vermeesch, 2012) was used to visually represent the relative likelihood (i.e. probability) of different ages in a population. This software allows a probability density distribution to be calculated using both the KDE and PDP simultaneously. The software also incorporates the mixture modelling algorithm of Galbraith (2005), which was used to resolve multiple age components within the age populations. Concordia plots and weighted average age (mean age) calculations were generated using the Isoplot 3.75 add-in for Microsoft *EXCEL* developed by Ludwig (2012).

5.3 ZIRCON MORPHOLOGY

Zircon separated from samples documented herein was assessed by conventional imaging techniques to guide isotopic analysis and aid geochronological interpretation.

5.3.1 Detrital Zircon—Quartzite (MB003)

Zircon grains liberated from quartzite sample MB003 display highly varied external morphologies and internal structures. Grains show colourless, pale pink, orange-brown to brown hues. Most crystals have rounded terminations resulting in ovoid morphologies, although prismatic and near spherical forms are also present (Figure 5.1). Less common are angular fragments and very elongate grains (Figure 5.1k, l). Aspect ratios range from 1.01:1–5.80:1, with 90% of mounted grains less than 3:1 (Table 5.4). Grain length ranges from *ca.* 60–350 μm , though generally <140 μm (Table 5.4).

Table 5.4 Summary of grainsize and aspect ratio distribution of mounted grains from quartzite sample MB003.

	Length (μm)	Width (μm)	Aspect Ratio (L/W)
Minimum	57.35	29.48	1.01
1st Quartile	98.98	51.58	1.64
Median	123.10	62.38	2.01
3rd Quartile	144.45	72.27	2.40
Maximum	348.48	212.18	5.80

Cathodoluminescence images of grains representing those selected for analysis are shown in Figure 5.1. In many grains, primary zonation has been variably altered by secondary structures (Figure 5.1e–g, j–l). In several examples, oscillatory zoned rim domains truncate zoned xenocrystic cores along an irregular boundary (Figure 5.1b). Faceted grains featuring unaltered primary oscillatory zoning are rare (Figure 5.1a). Small ovoid inclusions and fine cracks are common features of many grains. Thin, low CL response, selvages transgressing primary zonation from the crystal edge are also common (Figure 5.1f, j–l).

6.3.2 Magmatic Zircon—Boothby Orthogneiss (MB007)

Orthogneiss sample MB007 yielded an abundance of zircon. Grains are generally honey brown, with lesser colourless and pink varieties also present. Doubly terminating, prismatic grain shapes predominate, although some grains display more rounded morphologies. Grain lengths range from *ca.* 80–370 μm , though in contrast to zircon in sample MB003 most grains are >140 μm in length. Aspect ratios range from 1:1–4:1, with 95% of mounted grains less than 3:1 (Table 5.5).

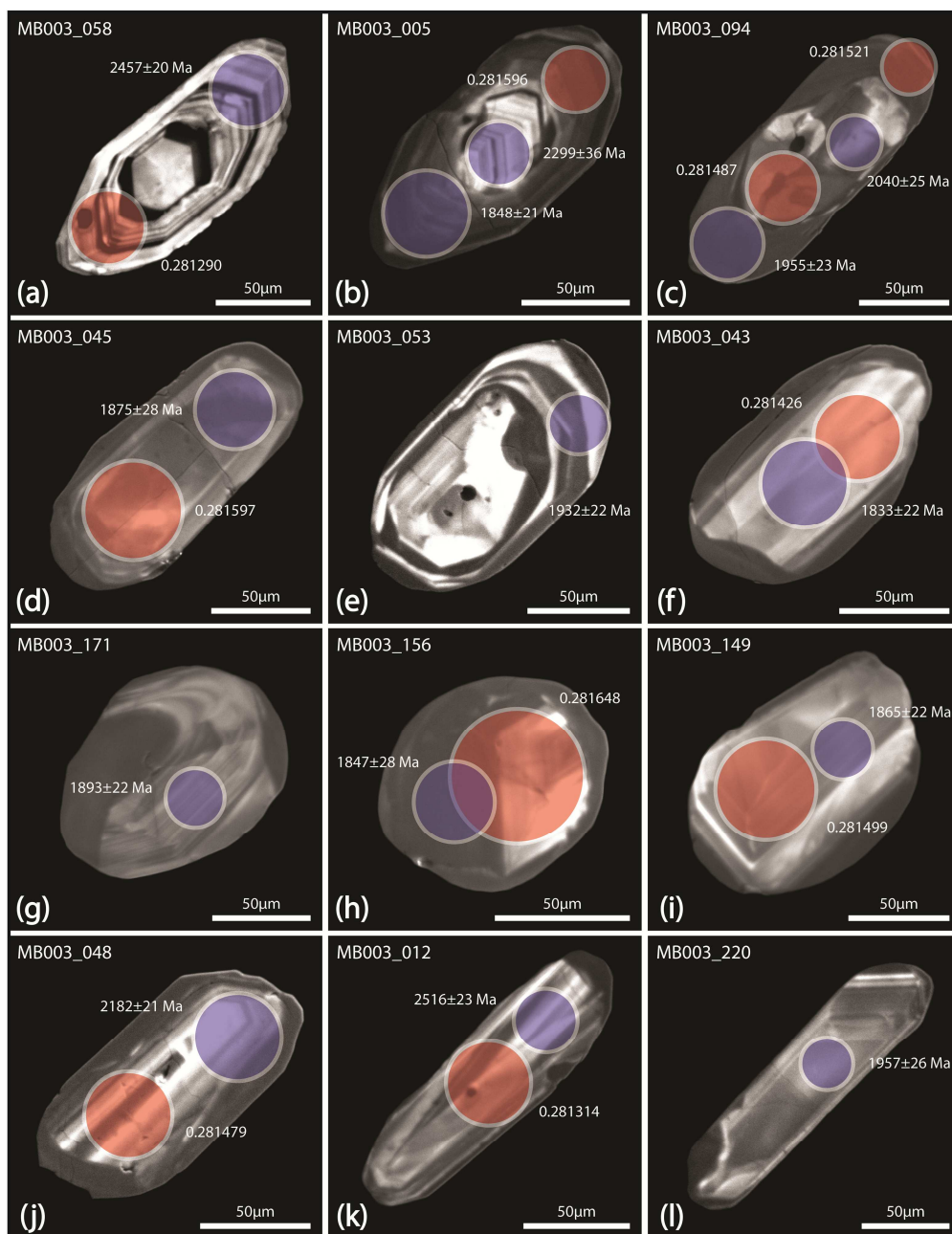
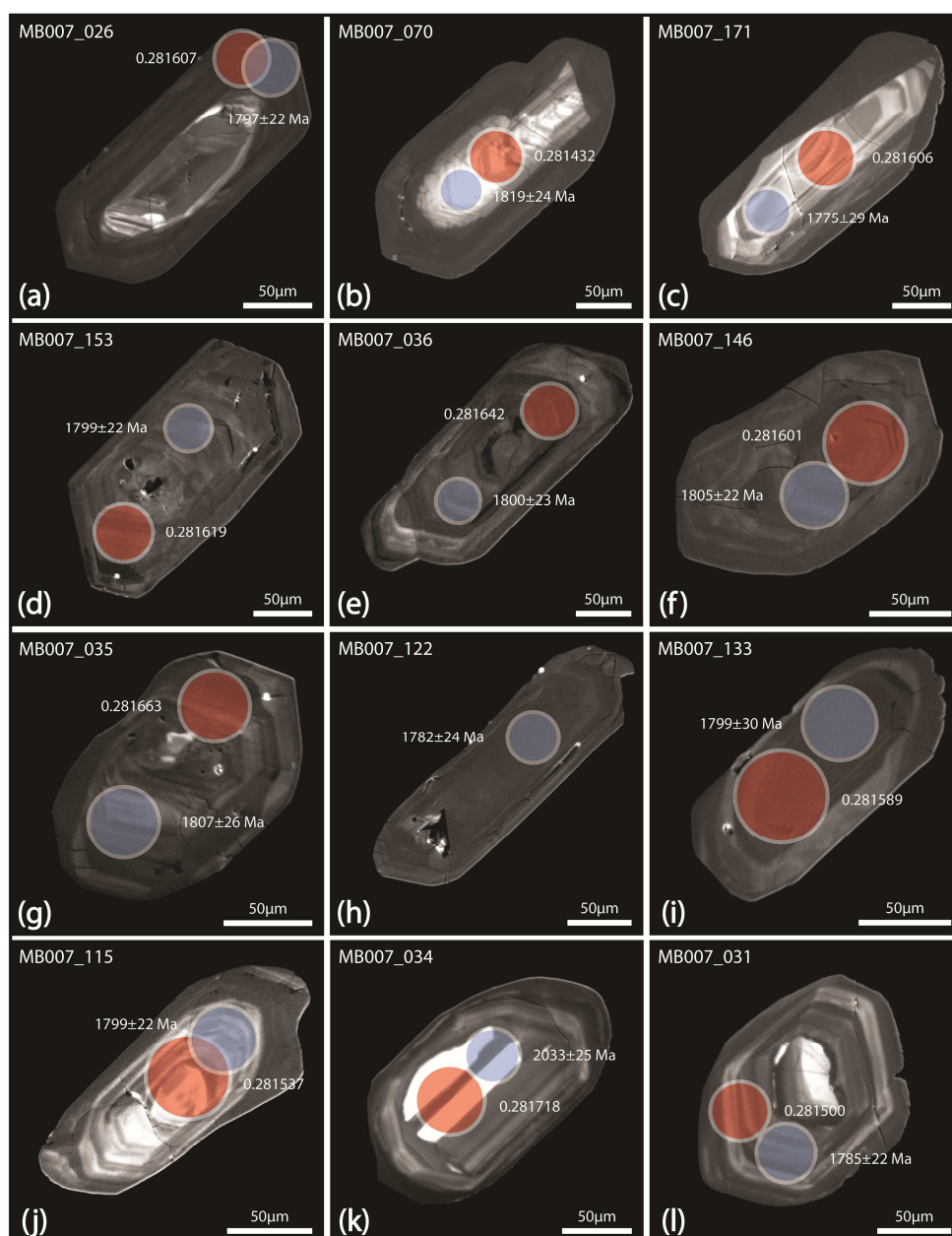


Figure 5.1 Cathodoluminescence images of representative grains from quartzite sample MB003 selected for isotopic analysis. Filled circles show ablation sites for Hf_i (red) and U–Pb (violet) analysis. Scale bar is 50 μm.

Figure 5.2 shows CL images of representative grains selected for isotopic analysis. Grains commonly display euhedral rim domains that feature well-defined moderate-response oscillatory zonation (Figure 5.2a, d, e). Along the boundary of some grains, this primary zonation is blurred or convoluted by secondary alteration (Figure 5.2f). Irregular shaped, xenocrystic cores are present in some grains (Figure 5.2a, k, l). Fractures are developed in the majority of grains including radial and concentric forms (Figure 5.2 h–i and k respectively). The central portions of many grains contain small cavities and inclusions surrounded by altered primary zoning (Figure 5.2d, g, e, h).

Table 5.5 Summary of grainsize and aspect ratio distribution of mounted grains from orthogneiss sample MB007.

	Length (μm)	Width (μm)	Aspect Ratio (L/W)
Minimum	78.42	37.10	1.01
1st Quartile	147.34	76.95	1.55
Median	182.49	92.46	1.99
3rd Quartile	221.34	109.82	2.42
Maximum	369.62	209.60	4.00

**Figure 5.2** Cathodoluminescence images of representative grains from orthogneiss sample MB007 selected for isotopic analysis. Filled circles show ablation sites for Hf_i (red) and U–Pb (blue) analysis. Scale bar is 50 μm .

5.3.3 Metamorphic Zircon—Diatexite (MB033)

Grain shapes vary between irregular-ovoid grains, elongate prisms with rounded terminations, and angular fragments (Figure 5.3). Grain length ranges from *ca.* 55–310 μm and aspect ratios from 1:1–3.45:1 (Table 5.6). It is noted that the distribution of grainsize is similar to that of sample MB003.

Table 5.6 Summary of grainsize and aspect ratio distribution of mounted grains from diatexite sample MB033.

	Length (μm)	Width (μm)	Aspect Ratio (L/W)
Minimum	54.51	31.89	1.01
1st Quartile	87.09	50.61	1.52
Median	107.48	58.28	1.80
3rd Quartile	129.77	70.41	2.12
Maximum	311.59	168.26	3.45

Characteristic of zircon from this sample are low CL response (low-response) rim domains that penetrate inward from the grain edge (Figure 5.3). These (generally structureless) features commonly mantle primary zoned core domains. The low-response rim domain–core domain transition is generally blurred (Figure 5.3c–e, g), although in some cases it is sharp and irregular (Figure 5.3h, i). In Figure 5.3f, ghosted primary zonation is preserved in the recrystallised low-response rim domain. Fractures are common in core domains but are rarely observed propagating into the surrounding rim domain, in most cases becoming blurred at the core-rim boundary (Figure 5.3a–d).

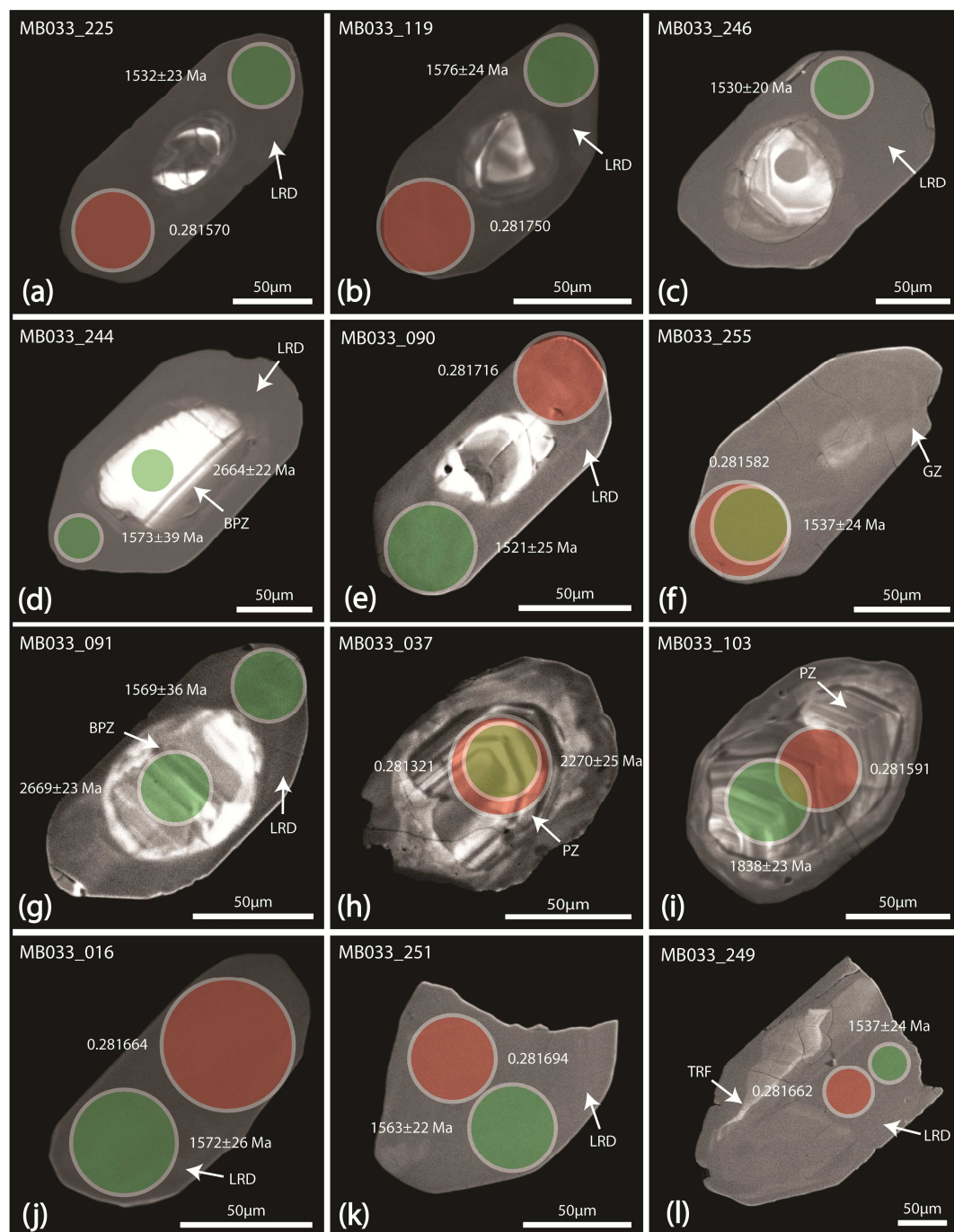


Figure 5.3 Cathodoluminescence images of representative grains from diatexite sample MB033 selected for isotopic analysis. Filled circles show ablation sites for Hf_i (red) and U–Pb (green) analysis. Labelled internal structures are low-response rim domain (LRD), primary zoning (PZ), blurred primary zoning (BPZ), ghost zoning (GZ), and transgressive reaction front (TRF). Scale bar is 50 μm.

5.4 U–PB ZIRCON GEOCHRONOLOGY

Initial U–Pb datasets were examined to assess the influence of common-Pb, central discordance and the performance of reference materials. These factors were taken into consideration when developing justifiable criteria to refine datasets for age calculations. Analyses were universally excluded when featuring:

1. >2% common-Pb
2. >5% central discordance

Analyses featuring >5% discordance are excluded from age calculation unless those analyses were used to define a discordia. At the ≤5% discordance level, analyses were progressively excluded from each dataset on the basis of highest weighted residual until a probability of ≥0.05 was achieved (indicating an age estimate at the 95% confidence limits). Each dataset was then re-evaluated, using the same approach, at the ≤3% and ≤2% discordance level in an attempt to explore the influence of discordance on the age calculation. More specialised exclusion criteria are discussed under relevant sample headings where appropriate.

As noted in Chapter 2, protolith ages in the Aileron Province are >1 Ga. As such, all ages referred to herein are reported as $^{207}\text{Pb}/^{206}\text{Pb}$ ages unless otherwise noted. All U–Pb geochronological data is presented in Appendix 3.

5.4.1 Detrital Zircon Geochronology—Quartzite (MB003)

A total of 107 analyses were conducted on a non-random sample of 104 grains (including 3 core-rim pairs) selected on the basis of available surface area for analysis. The dataset shows a high level of concordance with 87% of analyses displaying ≤5% discordance. Individual analyses produce a spread of ages from 3296 ± 22 Ma to 1468 ± 26 Ma, increasing in abundance from Palaeoarchaeon to Palaeoproterozoic ages (Figure 5.4). In Figure 5.4c, the probability density distribution is dominated by a population peak at *ca.* 1860 Ma, with subordinate populations occurring at *ca.* 1940 Ma, 2165 Ma, 2320 Ma and 2510 Ma. Core-rim pairs display significant age variation across these domains; in one instance the core being *ca.* 450 Ma older than the corresponding rim domain (Figure 5.1b). Thorium–uranium contents are variable, though values <1000 and <3000 ppm (respectively) predominate (Figure 5.5a). Thorium/uranium ratios are highly scattered ranging from 1.37–0.01, although relatively low Th/U ratios (<0.2) are more common with decreasing age (Figure 5.5b).

Of the 107 analyses, one analysis was excluded featuring >2% common-Pb and fifteen excluded featuring >5% discordance. A further two analyses featuring outlying ages of 1759 ± 23 Ma and 1726 ± 21 Ma were excluded, interpreted as grains affected by Pb-loss. This left $n = 89$ grains

suitable for calculation of the youngest coherent population of detrital ages. Using the method of Vermeesch (2004), this gave a 95% confidence that no age fraction composing $\geq 6.3\%$ of the total detrital population had been missed. Of the initial 89 grains, 54 were progressively excluded on the basis of highest weighted residual to achieve a mean age of 1864 ± 9 Ma ($n = 35$, MSWD = 1.3) defining the youngest statistically coherent population of detrital ages at the $\leq 5\%$ discordance level (Figure 5.6a). The dataset was then re-evaluated at the $\leq 3\%$ and $\leq 2\%$ discordance levels, producing mean ages of 1866 ± 11 Ma ($n = 30$, MSWD = 1.4) and 1861 ± 12 Ma ($n = 22$, MSWD = 1.2) respectively (Figure 5.6b, c; Table 5.7).

Table 5.7 Summary of mean age calculations to determine the youngest coherent population of detrital ages from quartzite sample MB003. Age calculation displayed in red is the preferred age estimate used in this study.

Exclusion Criteria	<i>n</i>	Weighted Average Age (Ma)	MSWD %	Probability of Fit
Initial Population	104	2092 ± 58	165	0.000
$\leq 2\%$ Common Pb	103	2097 ± 57	161	0.000
$\leq 5\%$ Discordance	35	1864 ± 9	1.3	0.110
$\leq 3\%$ Discordance	30	1866 ± 11	1.4	0.067
$\leq 2\%$ Discordance	22	1861 ± 12	1.2	0.240

Refining the dataset at the $\leq 3\%$ and $\leq 2\%$ discordance levels had little effect on the calculated age other than to increase statistical uncertainty (due to the reduced number of analyses included in the calculation; Table 5.7). For this reason the age calculated at the $\leq 5\%$ discordance level (1864 ± 9 Ma) is the preferred age estimate of this study. At the 95% confidence limit, this provides a maximum depositional age of 1873 Ma. Alternatively, when measured on the youngest individual age (1814 ± 32 Ma) the maximum depositional age is reduced to 1846 Ma at the 95% confidence limit.

In Figure 5.7c, detrital zircon ages from 5 Lander Package samples published by Claoué-Long & Edgoose (2008) and Claoué-Long *et al.* (2008) have been combined to generate a representative probability density distribution of the Lander Package for comparison with sample MB003. Columns representing a 50 Ma time period have been positioned behind each of the prominent age populations present in the quartzite probability density distribution. Following these columns, it is apparent that similar age populations are present throughout the Lander Package distribution.

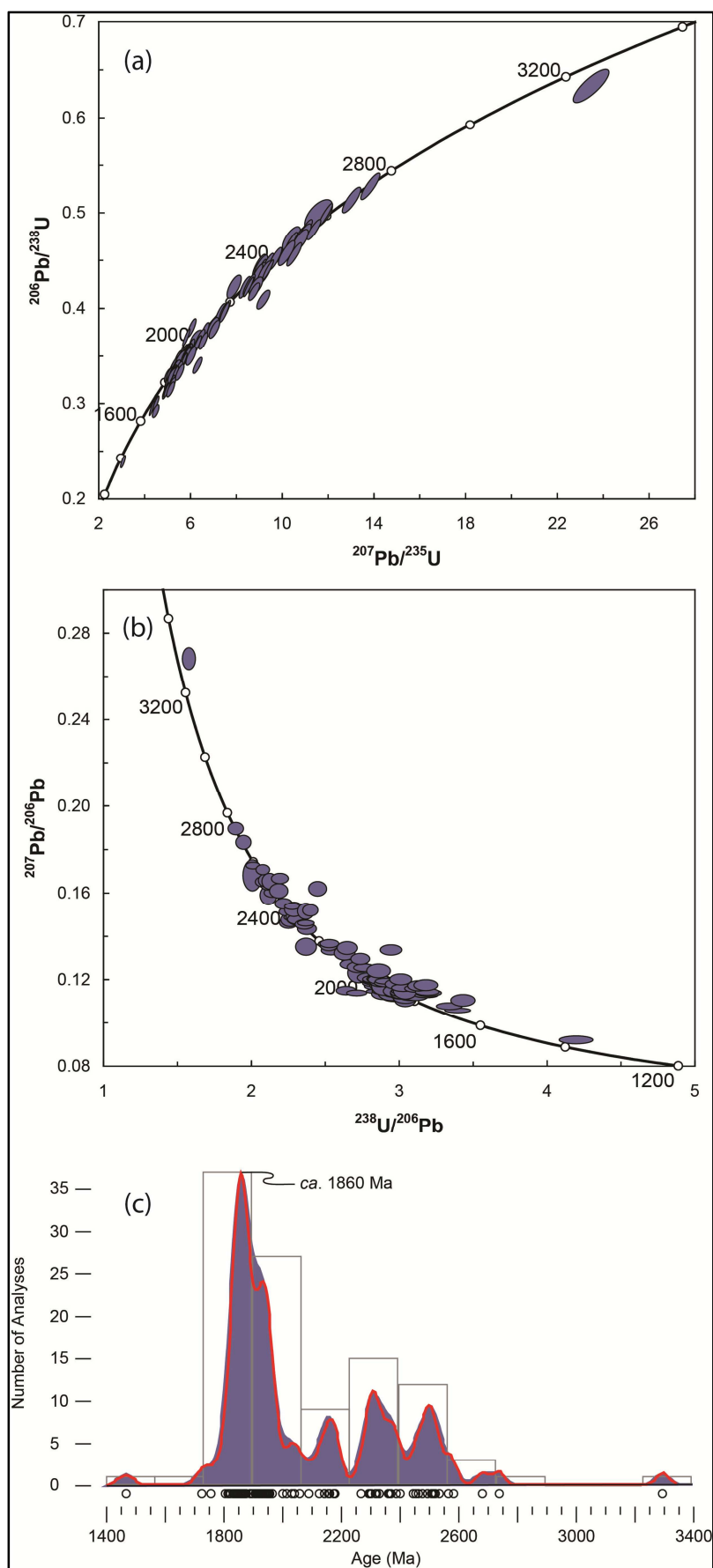


Figure 5.4 Caption continues onto following page.

Figure 5.4 All quartzite (MB003) analyses prior to age calculation; (a) Wetherill and (b) Terra–Wasserburg concordia diagrams, (c) and probability density distribution calculated using the KDE (filled curve) and PDP (red curve). Data point error ellipses are 2σ .

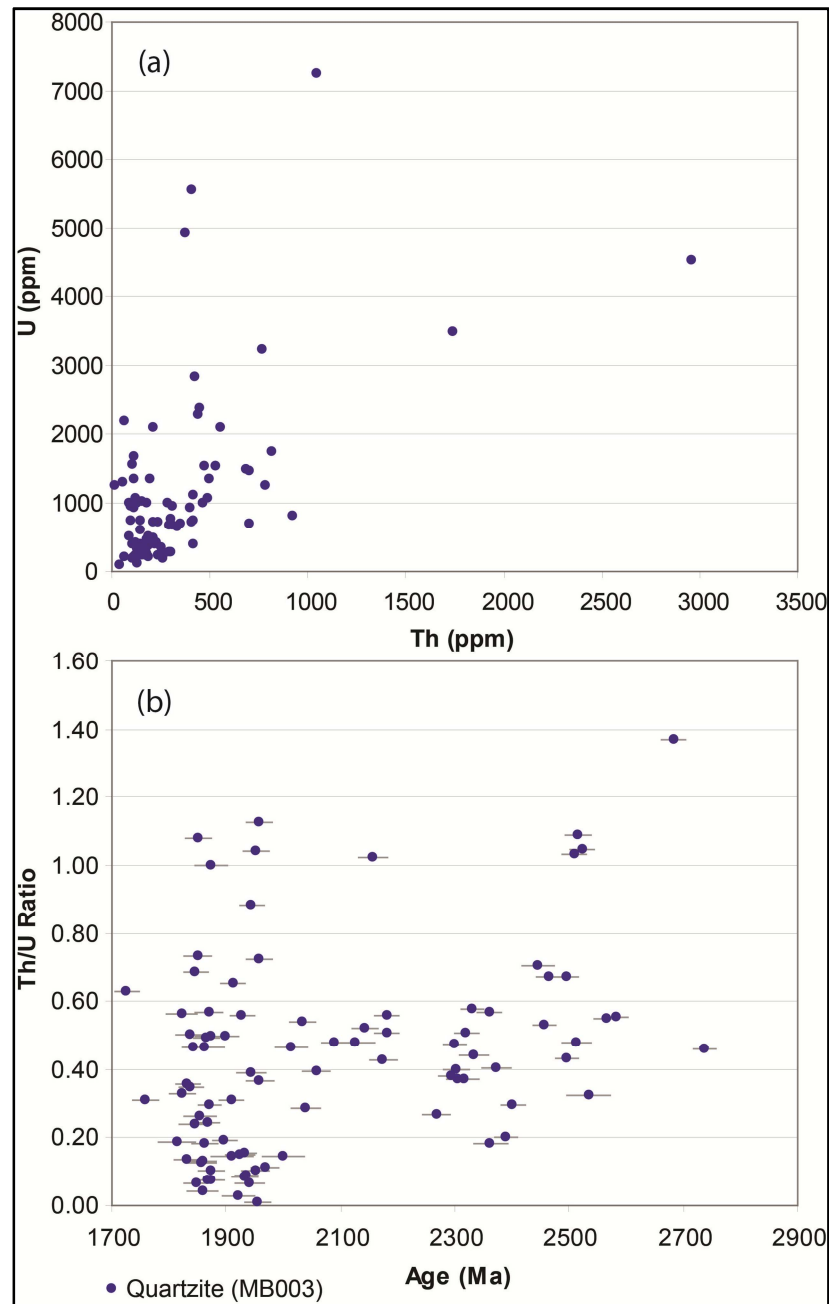


Figure 5.5 Bivariate plot of (a) U (ppm) versus Th (ppm) and (b) Th/U ratio versus age (Ma) of analyses from quartzite sample MB003. Error bars are 1σ .

Similarly, Figure 5.7b displays the combined probability density distribution of 2 Reynolds Package samples published by Worden *et al.* (2004) and Claoué-Long *et al.* (2008). As with the Lander Package samples, similar age populations are present throughout much of the Reynolds Package distribution. However, at the younger end of the distribution a prominent age population occurs at *ca.* 1795 Ma that is absent from the Lander Package and sample MB003 distributions. Figure 5.7a presents the combined probability density distribution of a further 2 Reynolds Package samples documented by Claoué-Long *et al.* (2008). Despite the strong similarities with the Reynolds Package distribution in Figure 5.7b, it is noted that the *ca.* 1795 Ma population is absent from the distribution in these two samples, indicating this population is common, but not diagnostic, of Reynolds Package detritus.

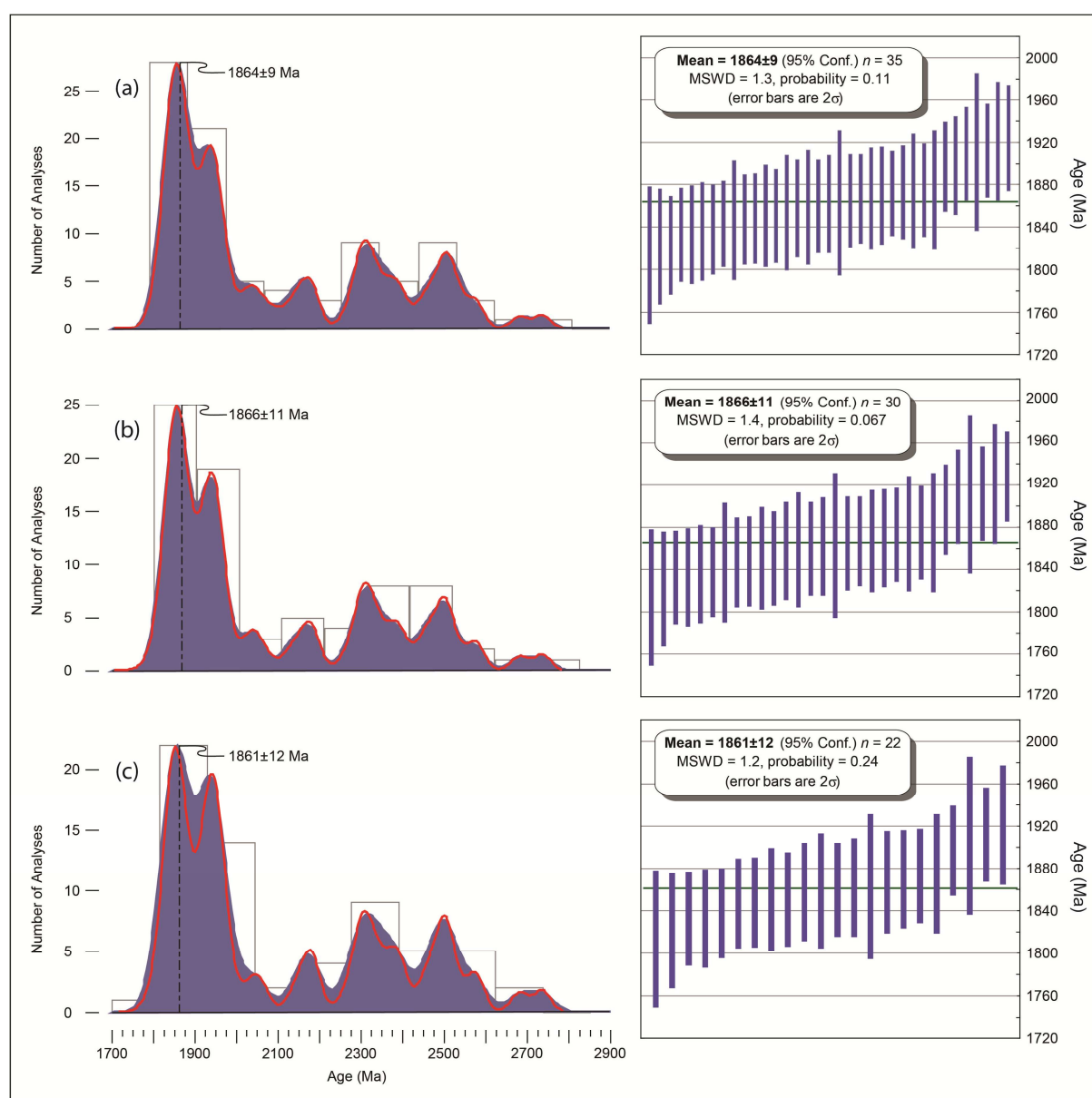


Figure 5.6 Caption continues onto following page.

Figure 5.6 Probability density distributions of quartzite sample MB003 calculated using the KDE (filled curve) and PDP (red curve) at (a) $\leq 5\%$ discordance (b) $\leq 3\%$ discordance (c) $\leq 2\%$ discordance. Detail to the right of each probability density distribution shows the youngest coherent population at each discordance level.

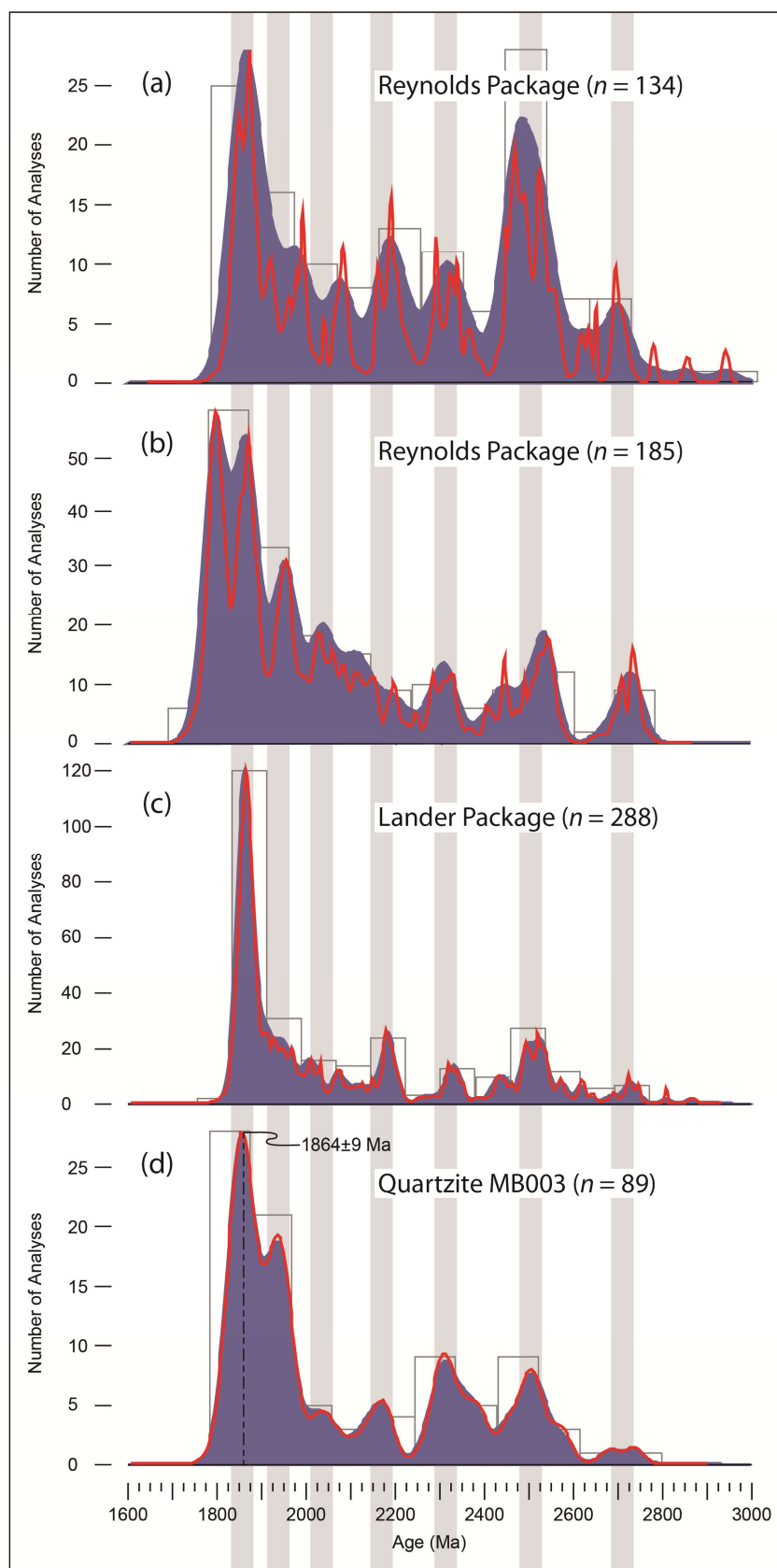


Figure 5.7 Caption continues onto following page.

Figure 5.7 Comparison of Reynolds Package (a) GA 2002082517^a, 2001082052^c (b) GA 2003089509^a, 2001082050^c and Lander Package (c) GA 2001082041^b, 2001082054^c, 99096006^c, 99096013^c, 99096014^c probability density distributions with (d) quartzite MB003. calculated using the KDE (filled curve) and PDP (red curve). Vertical columns are 50 Ma. Data from Worden *et al.* (2004)^a, Claoué-Long & Edgoose (2008)^b and Claoué-Long *et al.* (2008)^c.

5.4.2 Magmatic Zircon Geochronology—Boothby Orthogneiss (MB007)

In total, 60 grains were analysed targeting oscillatory zoned domains identified during CL imaging. The dataset shows a low incidence of common-Pb (1 analysis displaying >2% common-Pb) and a high level of concordance with 88% of analyses displaying $\leq 5\%$ discordance. Individual ages range between 2456 ± 24 Ma and 1635 ± 26 Ma with the majority of analyses clustering about concordia from *ca.* 1950–1800 Ma (Figure 5.8a, b). Within this main cluster, the KDE in Figure 5.8c resolves a prominent age population at *ca.* 1800 Ma, with a subordinate population occurring at *ca.* 1865 Ma—coinciding with the youngest coherent population present in sample MB003 and wider Lander Package detritus.

Approximately half of grains composing the 1800 Ma population show U concentrations >1400 ppm, distinctly higher than those found in the 1865 Ma population and older inheritance (Figure 5.9a). However, when compared with Th–U values from sample MB003 this distinction is less apparent. The main cluster of analyses generally show Th/U ratios <0.40, with no obvious distinction between Th/U ratio and age (Figure 5.9b).

The discontinuous spread of older ages, along with the *ca.* 1865 Ma population, indicates inherited grains have been analysed. Excluding the older inherited grains is relatively simple given they pre-date the earliest rocks in the Aileron Province. However, excluding inherited zircon of the *ca.* 1865 Ma population is more complicated as they are morphologically and chemically similar to those composing the dominant *ca.* 1800 Ma population. As such, the only criterion available to exclude inheritance from the dataset is age, which becomes statistically ambiguous given the close temporal relationship between near-crystallisation age inheritance and neocrystalline igneous zircon.

In an attempt to address this issue, the dataset was evaluated using the maximum depositional age constraints defined by sample MB003 (the likely source of inheritance), which besides constraining the age of sediment deposition, also constrains the minimum age of inheritance likely to have been assimilated into the intruding granite from surrounding country rock. This approach provided two criteria for excluding inheritance in sample MB007 based on (1) the youngest coherent population of ages (1873 Ma 95% confidence maximum); and (2) the youngest individual age (1846 Ma 95% confidence maximum). Taking a conservative approach, only analyses with lower limit uncertainties greater than or equal to the 95% confidence maximum were excluded. Crystallisation age estimates based on each of these criteria are now considered in turn.

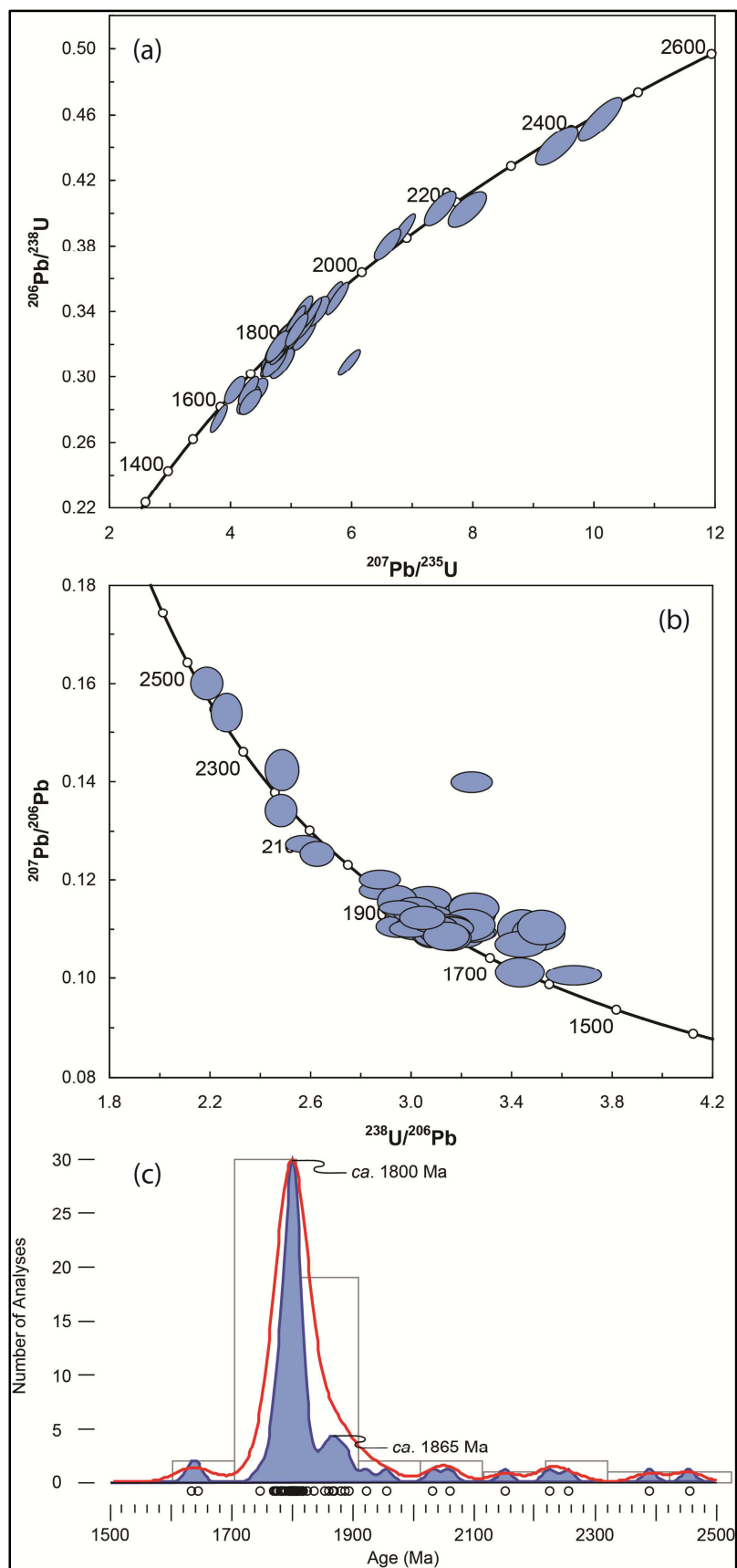


Figure 5.8 Caption continues onto following page.

Figure 5.8 All orthogneiss (MB007) analyses prior to age calculation; (a) Wetherill and (b) Terra–Wasserburg concordia diagrams, (c) and probability density distribution calculated using the KDE (filled curve) and PDP (red curve). Data point error ellipses are 2σ .

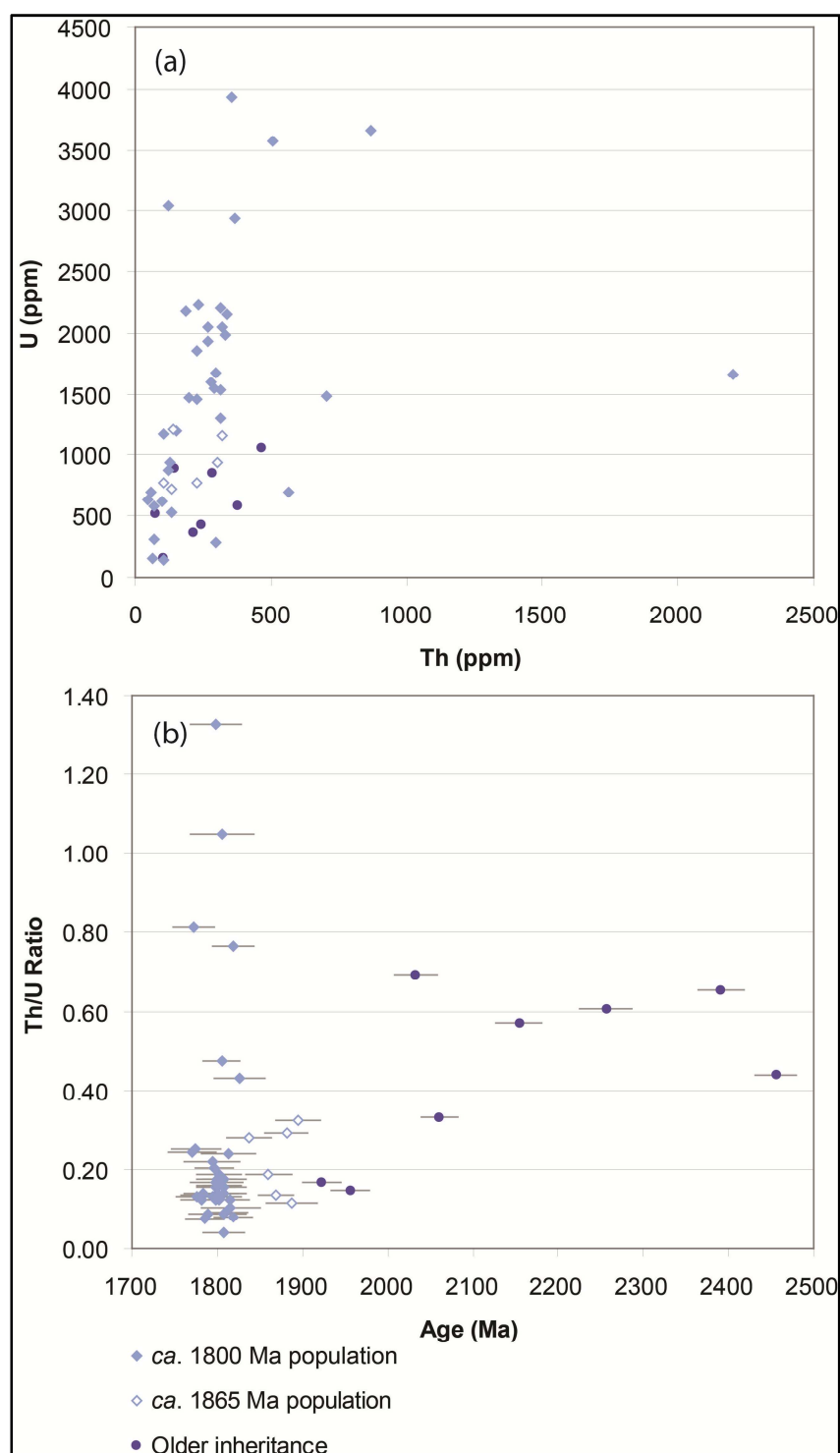


Figure 5.9 Bivariate plot of (a) U (ppm) versus Th (ppm) and (b) Th/U ratio versus age (Ma) of analyses from orthogneiss sample MB007. Error bars are 1σ .

EXCLUSION OF INHERITANCE ≥ 1873 Ma

One analysis was excluded with $>2\%$ common-Pb. Three outlying ages of 1645 ± 39 Ma, 1635 ± 26 Ma and 1747 ± 37 Ma were excluded on account of Pb-loss. Nine analyses with lower limit uncertainties ≥ 1873 Ma were excluded on the basis of inheritance. A further 5 grains were excluded featuring $>5\%$ discordance, leaving $n = 43$ analyses suitable for age calculation at the $\leq 5\%$ discordance level. The resultant dataset produced a mean age of 1809 ± 8.8 Ma ($n = 43$, MSWD = 1.3; Figure 5.10a). Refining the dataset at the $\leq 3\%$ and $\leq 2\%$ discordance levels, produced mean ages of 1808 ± 9 Ma ($n = 36$, MSWD = 1.2) and 1809 ± 10 Ma ($n = 33$, MSWD = 1.3) respectively (Table 5.8; Figure 5.10b, c).

Table 5.8 Summary of mean age calculations for orthogneiss sample MB007 based on a ≥ 1873 Ma cut-off to characterise inheritance.

Rejection Criteria	n	Weighted Average Age (Ma)	MSWD %	Probability of Fit
Analyses ≤ 1873 Ma	49	1809 ± 9	1.3	0.08
$< 2\%$ Common Pb	48	1808 ± 8	1.3	0.11
$\leq 5\%$ Discordance	43	1809 ± 9	1.3	0.09
$\leq 3\%$ Discordance	36	1808 ± 9	1.2	0.17
$\leq 2\%$ Discordance	33	1809 ± 10	1.3	0.12

Kernel density estimates in Figure 5.10 show that by using a ≥ 1873 Ma cut-off to characterise inheritance, nearly half of the *ca.* 1865 Ma population is included in the age calculation, almost certainly biasing the age towards an older estimate. It is also noted that 31% of detrital ages in the quartzite sample would have been included in the age calculation based on the ≥ 1873 Ma cut-off, confirming the likelihood that near crystallisation age inheritance is a problem in this calculation.

To further investigate the influence of inheritance on age calculation, concordant analyses from MB003 with lower limit uncertainties < 1873 Ma were combined with those from MB007 used for age calculation. The mixture modelling algorithm of Galbraith (2005) was then used to resolve multiple age components within this hybrid population without predefining the number of age components present. Figure 5.11 shows that at the $\leq 5\%$ and $\leq 3\%$ discordance levels, the hybrid population is bimodal, with statistically resolved components that closely equate to the calculated detrital and inferred-magmatic populations (Table 5.9). However, at the $\leq 2\%$ discordance level a single intermediate age component is resolved, which is geologically meaningless (Table 5.9).

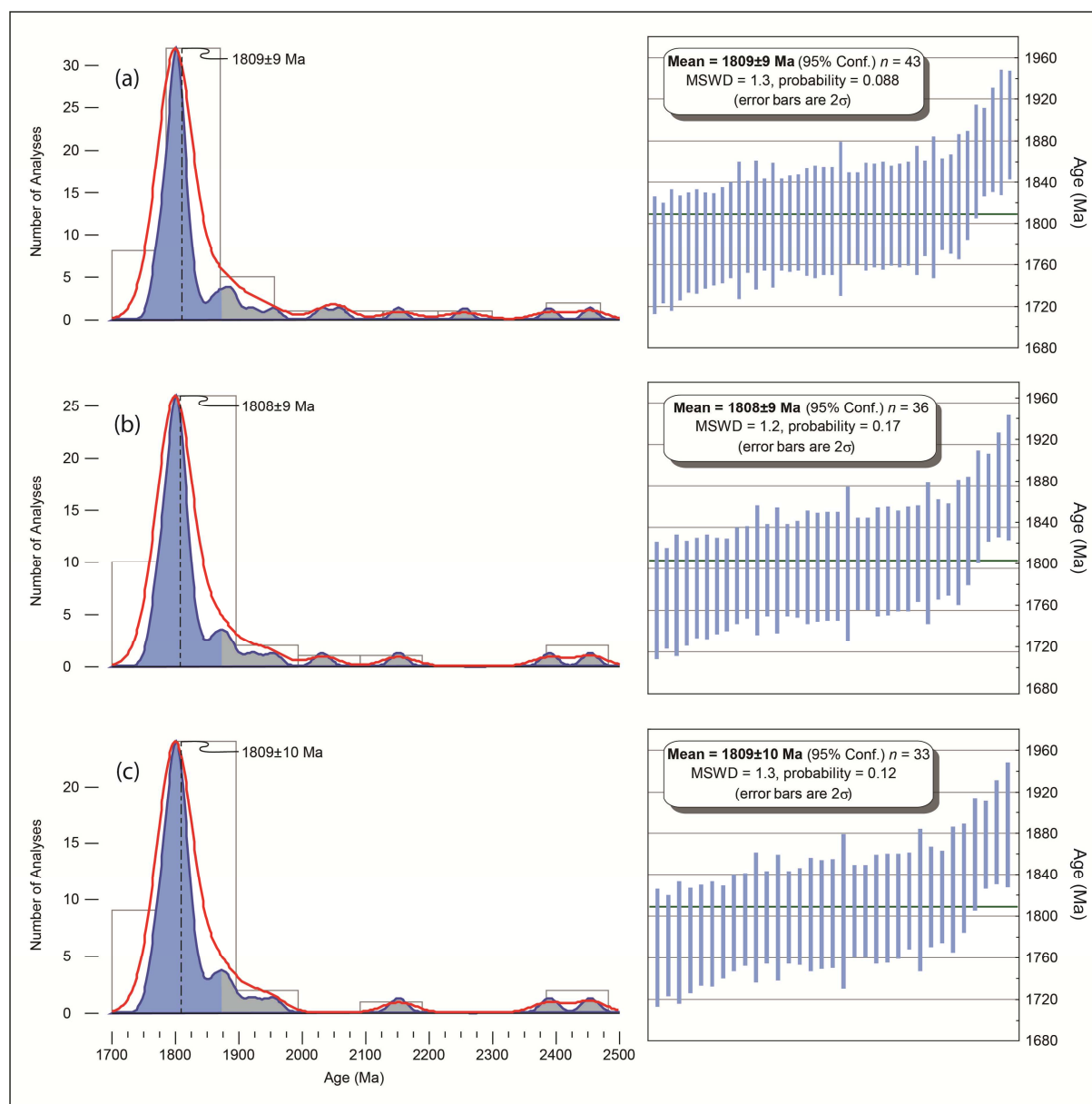


Figure 5.10 Probability density distributions of orthogneiss sample MB007 calculated using the KDE (filled curve) and PDP (red curve) at (a) $\leq 5\%$ discordance (b) $\leq 3\%$ discordance (c) $\leq 2\%$ discordance. Detail to the right of each probability density distribution shows the mean age at each discordance level using an 1873 Ma cut-off.

Table 5.9 Summary of mixture modelling for hybrid dataset based on a ≥ 1873 Ma cut-off to characterise inheritance.

Discordance Level	Modelled Components (Ma)	Proportions (%)
$\leq 5\%$ Discordance	1806 \pm 6	57 \pm 10
	1856 \pm 6	43 \pm 10
$\leq 3\%$ Discordance	1804 \pm 6	55 \pm 10
	1854 \pm 7	45 \pm 10
$\leq 2\%$ Discordance	1825 \pm 3	100

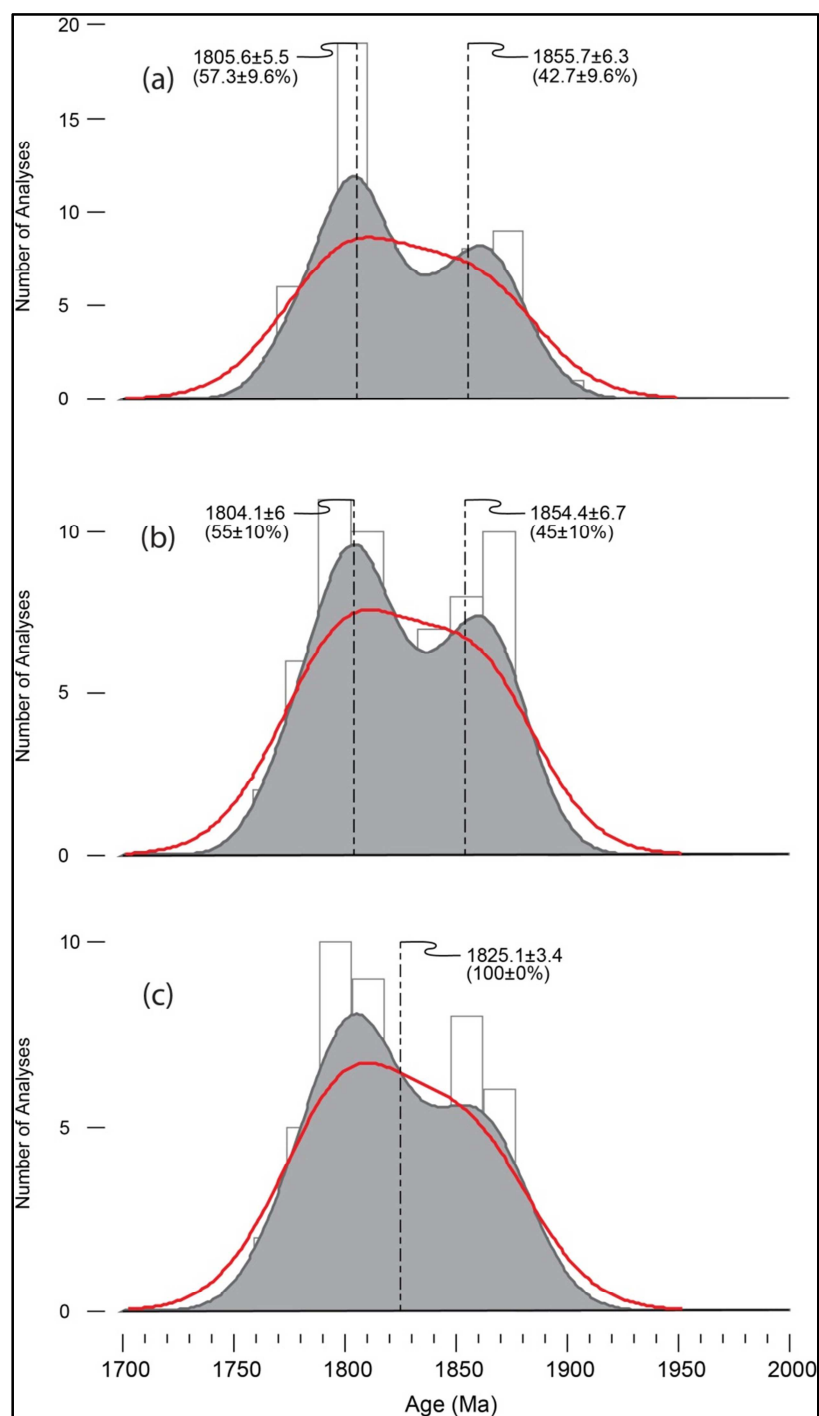


Figure 5.11 Probability density distributions of hybrid dataset calculated using an 1873 Ma cut-off to define inheritance. Filled and red curves calculated using the KDE and PDP respectively. Indicated age components and their relative proportions modelled using the mixture modelling algorithm of Galbraith (2005).

EXCLUSION OF INHERITANCE ≥ 1846 Ma

By evaluating the dataset in terms of the youngest individual age, a further 4 analyses with lower limit uncertainties ≥ 1846 Ma were excluded from the age calculation at the $\leq 5\%$ discordance level. The resultant dataset produced a mean age of 1801 ± 8 Ma ($n = 39$, MSWD = 0.45; Figure 5.12). Refining the dataset at the $\leq 3\%$ and $\leq 2\%$ discordance levels, produced near identical mean ages of 1801 ± 9 Ma ($n = 33$, MSWD = 0.51) and 1802 ± 9 Ma ($n = 30$, MSWD = 0.54) respectively (Figure 5.12; Table 5.10).

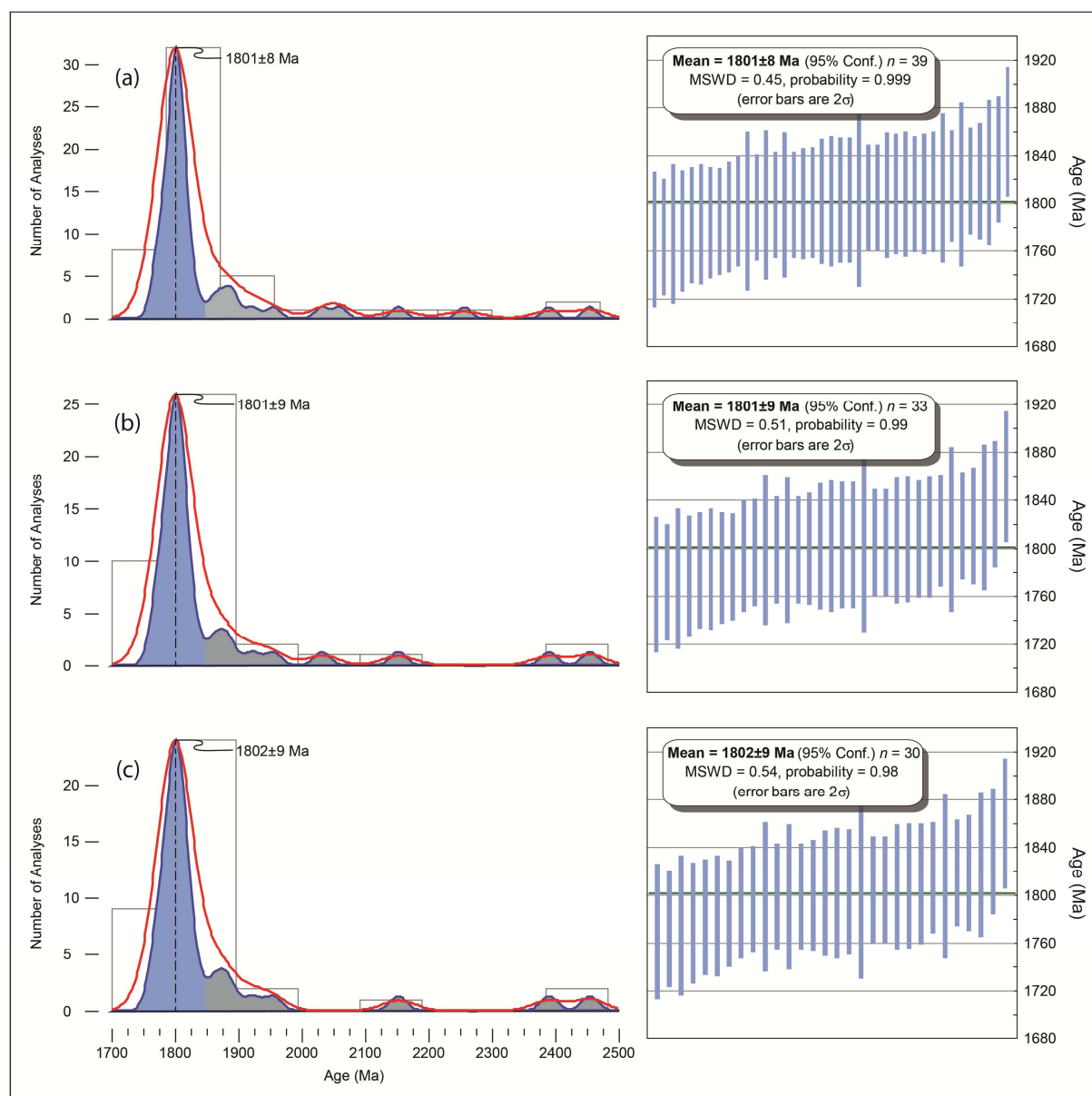


Figure 5.12 Probability density distributions of orthogneiss sample MB007 calculated using the KDE (filled curve) and PDP (red curve) at (a) $\leq 5\%$ discordance (b) $\leq 3\%$ discordance (c) $\leq 2\%$ discordance. Detail to the right of each probability density distribution shows the mean age at each discordance level using an 1846 Ma cut-off.

Table 5.10 Summary of mean age calculations for orthogneiss sample MB007 based on a ≥ 1846 Ma cut-off to characterise inheritance. Age estimate in red text indicates the preferred age estimate of this study.

Rejection Criteria	<i>n</i>	Weighted Average Age (Ma)	MSWD %	Probability of Fit
Analyses ≤ 1846 Ma	45	1802 \pm 8	0.59	0.99
$\leq 2\%$ Common Pb	44	1801 \pm 8	0.49	0.99
$\leq 5\%$ Discordance	39	1801 \pm 8	0.45	0.99
$\leq 3\%$ Discordance	33	1801 \pm 9	0.51	0.99
$\leq 2\%$ Discordance	30	1802 \pm 9	0.54	0.98

Kernel density estimates in Figure 5.12 show this approach has effectively excluded the *ca.* 1865 Ma age population from age calculation and shifted the mean age to the centre of the *ca.* 1800 Ma population peak. Despite this, 25% of detrital ages in sample MB003 would still have been included in the magmatic age calculation based on the ≥ 1846 Ma cut-off.

As with the previous approach, concordant analyses from MB003 with lower limit uncertainties < 1846 Ma were combined with those from MB007 used for age calculation and the age components modelled. Figure 5.13 shows that at each level of refinement a single age component is resolved (Table 5.11); each significantly older than the inferred magmatic population calculated at 1801 \pm 8 Ma.

Table 5.11 Summary of mixture modelling for hybrid dataset based on a ≥ 1846 Ma cut-off to characterise inheritance.

Discordance Level	Modelled Components (Ma)	Proportions (%)
$\leq 5\%$ Discordance	1820 \pm 3	100
$\leq 3\%$ Discordance	1820 \pm 3	100
$\leq 2\%$ Discordance	1818 \pm 4	100

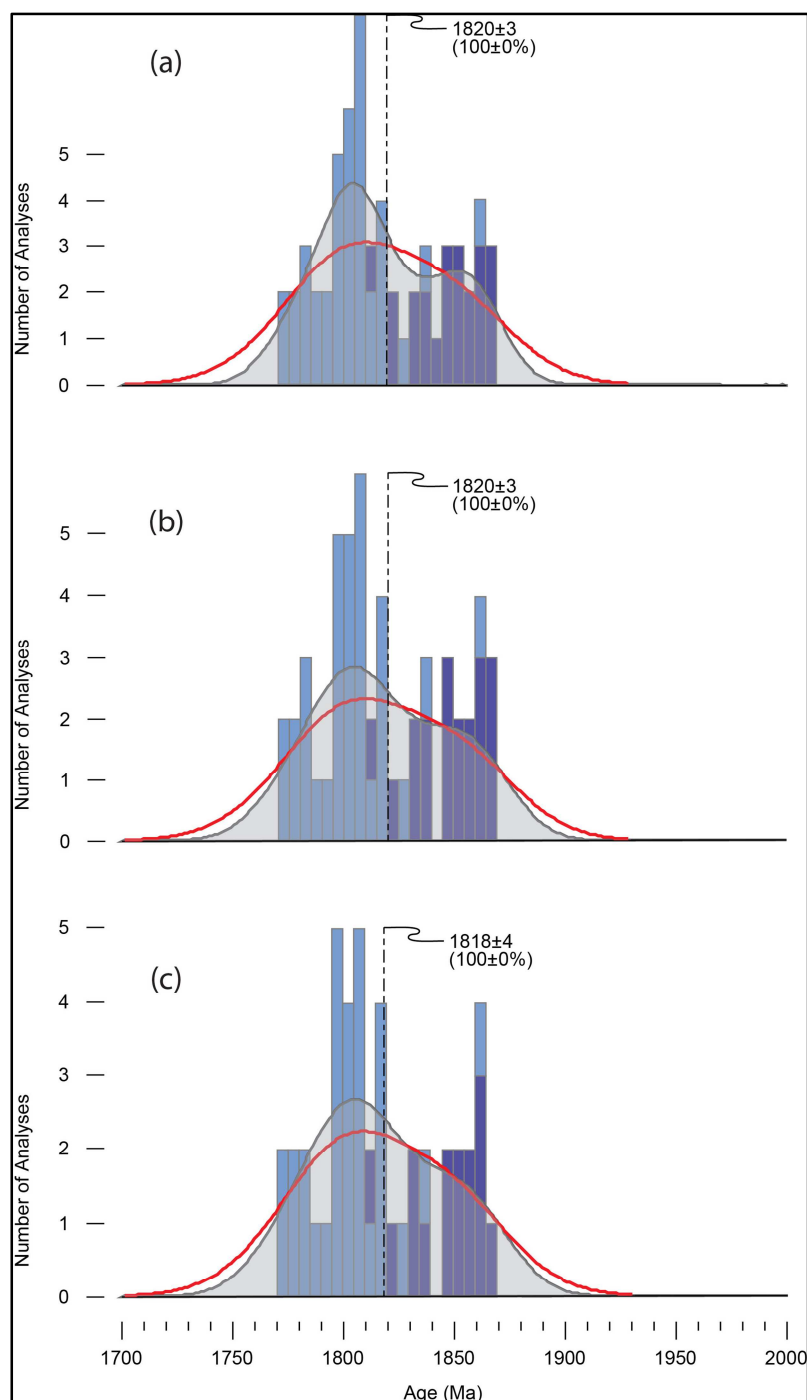


Figure 5.13 Probability density distributions of hybrid dataset calculated using an 1846 Ma cut-off to define inheritance. Filled and red curves calculated using the KDE and PDP respectively. Blue (MB007) and violet (MB003) bins shown in the cumulative frequency histogram illustrate the distribution of magmatic and detrital components within the hybrid dataset. Indicated age components and their relative proportions modelled using the mixture modelling algorithm of Galbraith (2005).

5.4.3 Metamorphic Zircon Geochronology—Diatexite (MB033)

Forty-eight analyses were conducted on 47 grains including low-response rim ($n = 35$) and core ($n = 13$) domains identified during CL imaging. The combined analyses produce a spread of ages ranging from 2676 ± 22 Ma to 1521 ± 25 Ma (Figure 5.14a, b). Core analyses occur intermittently from 2669 ± 23 Ma to 1716 ± 41 Ma, with minor populations present at 1833 ± 21 Ma ($n=6$) and 2666 ± 31 Ma ($n=2$). With the exception of three outlying analyses (2036 ± 21 Ma, 1838 ± 23 Ma and 1774 ± 25 Ma), low-response rim domain analyses lie in the range *ca.* 1600–1520 Ma. Within this range, the KDE shown in Figure 5.14c resolves two prominent age populations at *ca.* 1575 Ma ($n = 21$) and 1530 Ma ($n = 11$). When plotted using the Tera-Wasserburg concordia diagram (Figure 5.14b), analyses composing the *ca.* 1575 Ma population extend horizontally from concordia towards younger ages with discordance ranging from 2.3–9.4%. In contrast, analyses composing the *ca.* 1530 Ma population lie on concordia with negligible discordance (0.0–0.7%). Investigating the relationship between apparent age and discordance, it was found that discordance is the only distinguishing characteristic between these two populations, which are otherwise identical in CL pattern and Th–U composition (documented below).

A strong trend exists between apparent age, zircon domain, and Th–U composition as shown in Figure 5.15a. Core domains display Th concentrations >200 ppm, U concentrations <3000 ppm, and Th/U ratios generally >0.2 . Further, Th/U ratio and apparent age progressively decrease together. In comparison, low-response rim domains are characterised by low Th concentrations (generally <200 ppm), high U concentrations (generally >3000 ppm), and Th/U ratios <0.05 (Figure 5.15). It is noted that the three outlying low-response rim domain analyses show distinctly higher Th/U ratios than the main grouping and more closely approximate the Th–U compositions of core domains (Figure 5.15b). Therefore, these grains are interpreted as recording a geochemical ‘memory’ of older inherited material and are excluded from further age calculations.

When considered together, an error weighted regression of all low-response rim domain analyses ($n = 32$) produced a single concordia intercept at 1540 ± 12 Ma (MSWD = 2.6, Prob. 0.000; Figure 5.16a). By applying an equal-error regression, the data define a discordia (MSWD = 2.6, Prob. = 0.000) with an upper concordia intercept at 1578 ± 37 Ma and an imprecise lower intercept at 397 ± 780 Ma (Figure 5.16c). The low probability of fit and high MSWD ($>>1$) calculated for both of these methods indicates non-statistical variation within the population.

Low-response rim domains were subsequently divided, on the basis of discordance, into two populations; grains with $>2\%$ discordance (discordant low-response rim domains) and grains with $\leq 2\%$ discordance (concordant low-response rim domains). Applying an error weighted regression, discordant low-response rim domains define a discordia (MSWD = 0.40, Prob. = 0.98) with an upper concordia intercept at 1594 ± 22 Ma and an imprecise lower intercept at 350 ± 360 Ma (Figure

5.16c). Concordant low-response rim domains ($n = 11$) produce a precise concordia age at 1531 ± 3 Ma (MSWD = 0.00072, Prob. = 0.98; Figure 5.16c).

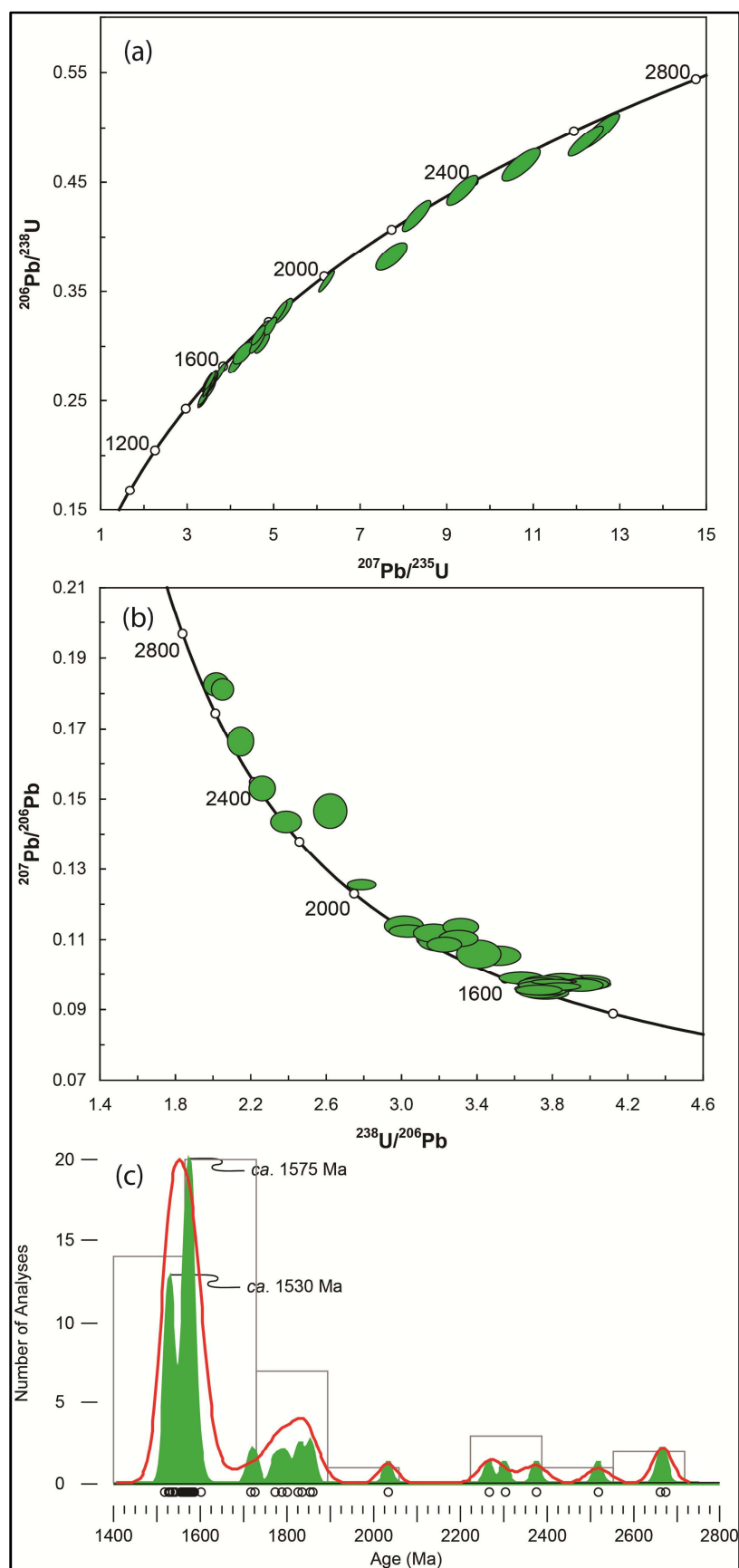


Figure 5.14 Caption continues onto following page.

Figure 5.14 All diatexite (MB033) analyses prior to age calculation; (a) Wetherill and (b) Terra–Wasserburg concordia diagrams, (c) and probability density distribution calculated using the KDE (filled curve) and PDP (red curve). Data point error ellipses are 2σ .

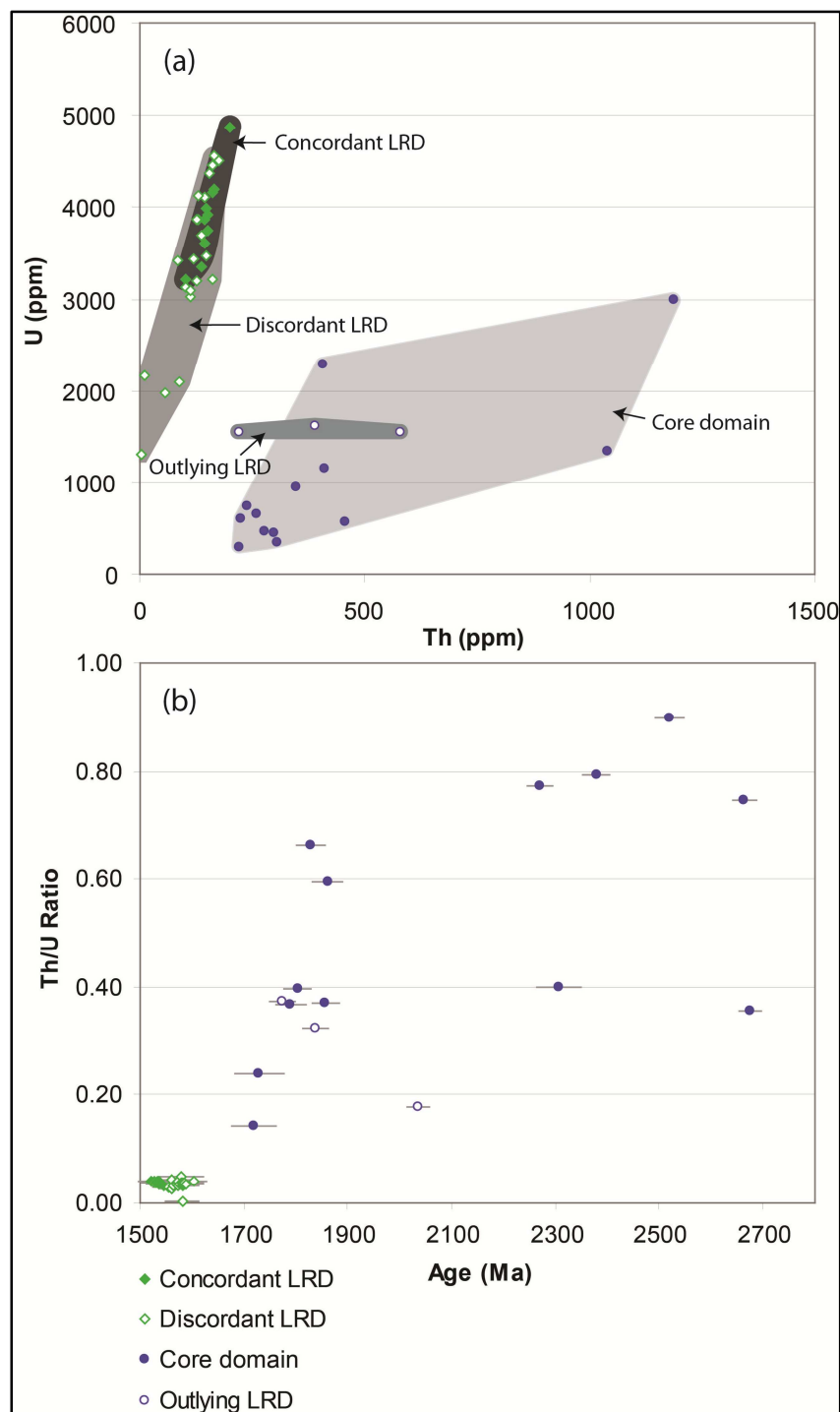


Figure 5.15 Bivariate plot of (a) U (ppm) versus Th (ppm) and (b) Th/U ratio versus age (Ma) of low-response rim (LRD) and core domains analysed from diatexite sample MB033. Note the strong correlation between Th–U composition, domain analysed, and age. Error bars are 1σ .

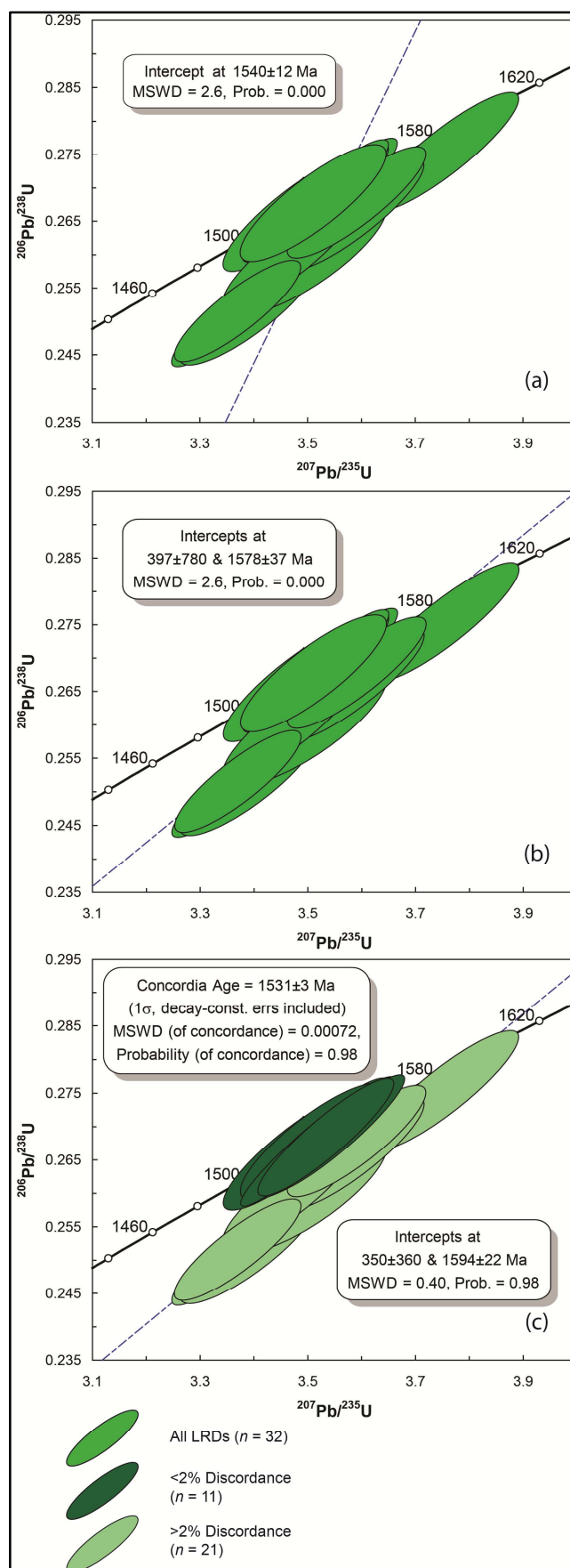


Figure 5.16 Caption continues onto following page.

Figure 5.16 Low-response rim domains (LRDs) considered as a single population by (a) error-weighted and (b) equal-error regression. (c) Low-response rim domains divided on the basis of discordance and evaluated by error weighted regression and concordia age calculation. Data point error ellipses are 2σ .

5.5 DISCUSSION

5.5.1 Detrital Zircon Geochronology—Quartzite (MB003)

The high degree of textural, chemical and geochronological variation observed in zircon from sample MB003 is consistent with their inferred detrital origin. CL imaging identifies rare grains with core-rim structures. However, the rim domains are interpreted as igneous overgrowths on the basis of oscillatory zoning and prismatic shape. Therefore, these primary zoned rims surrounding xenocrystic cores suggest a history of long-lived crustal recycling. Very narrow rim domains may represent metamorphic overgrowths, but these were too narrow to analyse.

Employing the maximum depositional age approach of Claoué-Long and Edgoose (2008), two estimates are produced for the quartzite from the Aileron Metamorphics. The unit was deposited by 1846 Ma (at the 95% confidence limit) on the basis of the youngest individual age (1814 ± 32 Ma). Alternatively, the youngest coherent group of ages has a mean age of 1864 ± 9 Ma, and so a 95% confidence maximum deposition age of 1873 Ma; this closely approximates the youngest population peak observed in the MB003 probability density distribution. Source rocks of this age are not known in the Arunta Region. The nearest potential source rocks include the granites and volcanic rocks of the Tennant Creek Supersuite Event (Cawood & Korsch, 2008). Otherwise, the detrital zircons may represent continental crust since eroded or hidden beneath the extensive basins that separate the Proterozoic orogenic zones. A more distal alternative source region within the North Australia Craton includes felsic rocks of the Kalkadoon Supersuite in the Mt Isa Orogen to the ESE (Cawood & Korsch, 2008).

The detrital zircon probability density distribution of quartzite sample MB003 shows a strong correlation with that of the Lander Package. Though some Reynolds package units contain a younger age peak in the detrital zircon probability density distribution (*ca.* 1795 Ma, Claoué-Long *et al.*, 2008; 1785 ± 15 Ma, Collins & Williams, 1995), the older age populations in Reynolds package detrital age distributions closely match the Lander Package. This is interpreted to represent derivation from the same protosource or recycling of Lander package to form Reynolds package (Claoué-Long *et al.*, 2008). Regardless, the similarity of detrital zircon probability density distributions in both the Lander and Reynolds packages makes the confident correlation of the Aileron Metamorphics with either of these packages difficult. However, the emplacement of the Boothby Orthogneiss around the same time as the *ca.* 1795 Ma peak in some Reynolds Package rocks dictates that the Aileron Metamorphics correlate with the Lander Package (see section 6.5.2).

5.5.2 Magmatic Zircon Geochronology—Boothby Orthogneiss (MB007)

Zircon analysed from sample MB007 is characterised by oscillatory zoned, euhedral grains shapes with well-defined terminations consistent with an igneous crystallisation origin (Corfu *et al.*, 2003; Halpin *et al.*, 2012). Modification of these primary structures along grain margins is interpreted as incipient metamorphic recrystallisation occurring in the solid-state post-emplacement (outlined in section 5.5.3).

In general, the interpretation of S-type granites sourced from metasedimentary rocks deposited only a few tens of millions of years prior is fraught, as the Gaussian distribution of ages in the neocrystallised population of igneous grains overlap the youngest grains in the source crust. The results documented above indicate inherited grains are present in the Boothby Orthogneiss, the youngest of which are within error of the igneous crystallisation age making them impossible to identify on the basis of age. In this case study, the size, shape, CL imagery and minor element chemistry of the inherited grains are also not distinct from the igneous ones, compounding the problem. Mixture modelling of the hybrid quartzite/orthogneiss dataset demonstrated that using the 1873 Ma cut off to characterise inherited grains statistically resolved two populations, suggesting this cut off was inadequate, including too many inherited grains in the “igneous” population. Mixture modelling of the hybrid dataset using the 1846 Ma cut off encouragingly resolved only one population. However, 24% of the concordant grains from quartzite sample MB003 were included in this single population. Additionally, the modelled peak was *ca.* 20 million years older than the preferred age estimate of 1801 ± 8 Ma, confirming the likelihood that near crystallisation age inheritance is a significant problem for the age calculation of the orthogneiss. As such, the age presented in this study is likely a slight over-estimate of the true crystallisation age of the Boothby Orthogneiss protolith. The youngest 17 of 24 detrital grains included in the hybrid dataset from the quartzite overlap with the oldest 7 of 39 grains included from the orthogneiss. It is in this region of overlap between the two samples that the near crystallisation age inheritance in the orthogneiss likely influences age calculations. As discussed, no criteria so far have distinguished the near crystallisation age inheritance. To gain an indication of the maximum possible influence of this problem on the age calculation, and using the overlap in the hybrid data set mixture model as a guide to estimate which of the older grains in the orthogneiss may be inherited, a further 7 may be excluded from the age calculation resulting in 1796 ± 9 Ma for the orthogneiss. A more conservative reduction of the orthogneiss dataset (excluding the oldest 3 of these 7 grains) results in 1799 ± 8 Ma. These approximations demonstrate that the 1801 ± 8 Ma age is at most *ca.* 5 million years too old. This would be reduced if any of the youngest grains in the orthogneiss were affected by very minor Pb-loss. The Hf-isotopic composition of the zircon grains is explored in the next chapter to further evaluate distinction of inherited from magmatic grains.

The 1801 ± 8 Ma crystallisation age of the Boothby Orthogneiss calculated in this study closely equates the reported SHRIMP age of 1806.1 ± 3.7 Ma (unpublished GA/NTGS report Worden *et al.*, 2008). However, this study has demonstrated the difficulty in discriminating near-crystallisation age inheritance from new magmatic growth, and so this age is also likely to be an over estimate of the true crystallisation age of the protolith granitoid. Similar difficulties in identifying inheritance were encountered by Collins & Williams (1995) in their study of the Mount Stafford and Warimbi granites, NW of the study area. They suggested the lack of morphological discriminant of near-crystallisation age inheritance was the result of thin melt-precipitated overgrowths giving euhedral form to inherited grains.

The low MSWD (< 1) of the 1801 ± 8 Ma age calculation suggests the internal errors of each age measurement are excessive. This is a result of the conservative uncertainty adopted for the external calibration standard GJ by the GAU, which is then propagated through the unknowns in the GLITTER software (Pearson N.J. pers. comm.).

Importantly, the preferred age (1801 ± 8 Ma) presented in this study places the thermal process generating the protolith granitoid within the 1810–1800 Ma Stafford Event. This relationship determines that protolith sedimentary rocks of the Aileron Metamorphics are time equivalents of the Lander Package. The D1 deformation event is limited by the maximum deposition age using the youngest individual age (1846 Ma) and the emplacement age of the cross cutting Boothby Orthogneiss protolith (1801 ± 8 Ma).

5.5.3 Metamorphic Zircon Geochronology—Diatextite (MB033)

Textural relationships between low-response rim domain and core domains may be explained in two ways: (i) the low-response rim domains are consistent with a process of metamorphic zircon formation by solid-state recrystallisation of protolith zircon proposed by Hoskin & Black (2000) or (ii) the low-response rim domains are neocrystallised overgrowths from the crystallising diatextite. Option one is supported by progressive changes in Th/U ratio and age observed in core domains that are consistent with the expulsion of Th accompanying Pb-loss during recrystallisation of protolith zircon grains. Hoskin & Black (2000) interpret this relationship as preferential expulsion of Th cations from the recrystallising zircon lattice on account of its larger radii (Th^{4+} is *ca.* 4% larger than the U^{4+} cation). These authors also interpret the apparent enrichment of U, with progressive recrystallisation, as reflecting heterogeneous primary trace element distribution and incomplete cation expulsion during metamorphic recrystallisation. Alternatively, this relationship may reflect recrystallisation in the presence of a U enriched partial melt, promoting diffusion of U^{4+} cations into the recrystallising lattice or growth of new zircon from crystallisation of the U enriched melt. Similarities in grain size distribution and apparent age between partially recrystallised core domains

from sample MB033 and detrital zircon from sample MB003 suggest the source of protolith zircon was likely local or lower level Lander Package entrained as selvages into the intruding partial melt.

Consistent CL patterns and Th–U chemistry observed in low-response rim domains form a single population. However, the high MSWD and low probability of fit observed in regressions of a single population do not support this interpretation, both of which suggest non-statistical (i.e. geological) variation within the population. Dividing low-response rim domains into two populations on the basis of discordance substantially improves the statistical adequacy of the dataset, so it is on the assumption of two populations that low-response rim domains are interpreted.

Discordant low-response rim domains define a discordia with no excess scatter projecting from 1594 ± 22 Ma and intersecting concordia at 350 ± 360 Ma. Both of these ages have geological significance given the known tectonic events that have affected the Aileron Province. The upper intercept coincides with the Chewings Orogeny (*ca.* 1580 Ma), and is consistent with previous interpretations that the southeast Reynolds Range underwent regional LPHT metamorphism during this time (Vry *et al.*, 1996; Williams *et al.*, 1996; Rubatto *et al.*, 2001). The lower intercept coincides with the Alice Springs Orogeny (450–300 Ma). However, the statistical uncertainty of the lower intercept dictates that (at best) this age can be interpreted as recent isotopic disturbance.

Concordant low-response rim domains define a concordia age of 1531 ± 3 Ma, but are more difficult to interpret, as this age is younger than published ages for the Chewings Orogeny (1600–1562 Ma taking the oldest and youngest zircon ages determined to date) and this group are younger than the upper intercept of the discordia defined by the discordant grains. Williams *et al.* (1996) reported metamorphic zircon from leucosome segregations in Reynolds Package metasedimentary rocks *ca.* 15 km west northwest of the study area. In this study they found that deformed segregations were 26 ± 3 million years older than the discordant ones, and suggest that metamorphism was long-lived and outlasted pervasive deformation. The *ca.* 1530 Ma age determined here suggest that the Chewings Orogeny may have lasted up to 63 ± 7 million years. This is consistent with a slowly changing thermal event as proposed by Hand & Buick (2001). In that study, the heat source is from abnormally high levels of crustal heat production from both Stafford and Yambah event granites. Williams *et al.* (1996) estimate slow cooling toward solidus on the order of 3°C Ma^{-1} that is consistent with a protracted period of high-T.

One scenario to explain the presence of two age populations in low-response rim domains involves the discordant population being inherited in the diatextite, having formed early in the Chewings Orogeny. These grains must also have been vulnerable to the recent isotopic disturbance indicated by the discordia. In contrast, concordant low-response rim domains must have formed via a different process, possibly including growth during crystallisation of the diatextite, as these were not susceptible to the recent isotopic disturbance recorded by the other group.

Similar mineral minor element and textural observations as those presented here have been documented in Chewings Orogeny zircon elsewhere in the Reynolds–Anmatjira ranges, suggesting these characteristics are a common feature of LPHT metamorphic processes in this region (Collins & Williams, 1995; Vry *et al.*, 1996; Williams *et al.*, 1996; Rubatto *et al.*, 2001).

6. LU–HF ISOTOPE ANALYSIS OF ZIRCON BY LA–MC–ICPMS

6.1 INTRODUCTION

Lutetium-176 is an unstable radionuclide that undergoes spontaneous β -decay to ^{176}Hf , with a half-life of *ca.* 37Ga (Kinny & Maas, 2003; Scherer *et al.* 2007). This decay scheme forms the basis of the Lu–Hf isotopic system, which is conventionally considered with respect to ^{177}Hf whose natural abundance is constant (Kinny & Maas, 2003). During mantle melting, the daughter element Hf fractionates more strongly than the parent element Lu into the melt fraction. Over time, the enrichment of Hf relative to Lu in the continental crust results in relatively less radiogenic (i.e. $\epsilon\text{Hf} < 0$) and more radiogenic (i.e. $\epsilon\text{Hf} > 0$) $^{176}\text{Hf}/^{177}\text{Hf}$ ratios in crustal and depleted mantle reservoirs respectively (Hawkesworth & Kemp, 2006).

As a phase enriched in Hf (*ca.* 1 wt% HfO_2) and with negligible radiogenic Lu, zircon records the Hf-isotopic character of the sources of the magmatic rocks in which it crystallises (Harley & Kelly, 2007). Consequently, detrital zircon preserves the Hf isotopic signature of their protosource region, thus presenting another tool that may be used to correlate sedimentary packages.

This chapter documents Hf-isotope analysis of selected zircon grains analysed during U–Pb geochronology to complement observations made during Chapter 5.

6.2 METHODS

Hafnium isotope analysis was conducted using a Nu Plasma 034 Multi Collector–ICPMS attached to a New Wave Research UP-213 LA system. Data acquisition parameters used during analysis are summarised in Table 6.1. Analysis included 30 seconds of background signal prior to ablation, followed by *ca.* 150 seconds (5 Hz) of signal acquisition. Samples were ablated using a spot size of 40–50 μm .

A typical run included one analysis of the reference standard Mud Tank, one analysis of the reference standard Temora II, analysis of 10 unknowns, followed by a further analysis of the reference standard Mud Tank. Initial interrogation of raw scan-by-scan data was conducted using Nu Plasma time-resolved analysis software (version 1.3.7024). Further refinement of the dataset was done using Microsoft *EXCEL* data worksheets developed for Terranechron® analysis (Belousova pers. comm.).

Analytical accuracy was monitored using internal reference standards Mud Tank (Griffin *et al.*, 2007) and Temora II (Woodhead & Hergt, 2005). Values obtained during this study are within statistical error of published values for these reference materials as shown in Table 6.2.

Table 6.1 Summary of operating conditions and data acquisition parameters used during Hf-isotope analysis by LA-MC-ICPMS.

LA system	
Make	New Wave Research
Model	UP-213
Type	Nd: YAG (solid-state)
Wavelength	213 nm
Beam diameter (spot size)	40-55 μm
Repetition rate	5 Hz
Fluence	$\sim 6.16 \text{ J/cm}^2$
MC-ICPMS system	
Make	Nu Plasma
Model	034
Type	Multi-collector
Gas flows:	
Plasma (Ar)	13 L/min
Carrier (He)	0.80 L/min
Make-up (Ar)	0.81 L/min
Data Acquisition Parameters	
Data acquisition protocol	Time-resolved analysis
Standards	
Primary reference standard	Mud Tank
Secondary reference standard	Temora II
Background signal time	30 seconds
Data acquisition signal time	~ 150 seconds
Isotopes determined	^{176}Hf , ^{177}Hf , ^{178}Hf , ^{179}Hf , ^{180}Hf , Yb, Lu
Data reduction software	Nu Plasma time-resolved analysis software (version 1.3.7024)

Table 6.2 Summary of published and observed values for reference standards obtained during LA-MC-ICPMS analysis of samples documented in this study.

Standard	Reported Value (Ma)		Measured Value (Ma)		
	Mean Ratio	1σ	Mean Ratio	1σ	<i>n</i>
Mud Tank (Griffin <i>et al.</i> , 2007)	0.282522	0.000042	0.282529	0.000013	20
Temora II (Woodhead & Hergt, 2005)	0.282686	0.000008	0.282722	0.000036	5

Initial $^{177}\text{Hf}/^{176}\text{Hf}$ (Hf_i) ratios and epsilon Hf (ϵHf) values were calculated using the ^{176}Lu decay constant of Scherer *et al.* (2001) of 1.865×10^{-11} . This decay constant was also used to calculate Depleted Mantle (DM) and CHondrite Uniform Reservoir (CHUR) growth-curves.

6.3 ZIRCON HF-ISOTOPE ANALYSIS

Hafnium-isotope analysis was conducted on grains identified during U–Pb geochronology displaying $\leq 2\%$ common-Pb and $\leq 5\%$ discordance. Isotope values measured in this study are presented in Appendix 4.

6.3.1 Detrital Zircon Hf Isotopes—Quartzite (MB003)

Hafnium-isotope compositions were measured for 69 grains from sample MB003. Initial $^{176}\text{Hf}/^{177}\text{Hf}$ ratios range from 0.281139 to 0.281757 showing significant variation between crustal and depleted mantle affinities across the range of crystallisation ages (Figure 6.1a). Analyses with crystallisation ages in the range *ca.* 2000–2200 Ma trend toward more depleted mantle affinities, although this may be an artefact of the small number of analyses in this age range ($n = 9$) with respect to analyses < 2000 Ma ($n = 37$) and > 2200 Ma ($n = 23$).

In Figure 6.1b, ϵHf values show a similar degree of variation from CHUR, ranging from -7.54 (less radiogenic) to 6.43 (more radiogenic). The number of ϵHf values plotting below CHUR generally increases with decreasing age. In contrast, positive ϵHf values remain somewhat stable across the spread of ages, following the trend of CHUR. As with Hf_i , ϵHf values are predominately positive in the range *ca.* 2000–2200 Ma.

To further examine whether the age correlation between detrital zircon in the Aileron Metamorphics and Lander Package is significant in terms of identifying a common protosource region to the metasedimentary rocks, Hf isotopic data from the quartzite was plotted with that of detrital zircon grains from the Mount Stafford Member (Lander Package equivalent; unpublished data provided by E. Dunkley, 2013). Initial hafnium and ϵHf values in the Mount Stafford Member show a similar distribution to the quartzite, although more extreme depleted mantle and crustal values are present. As with the quartzite, the Mount Stafford Member shows an increase in crustal Hf compositions with decreasing age. Interestingly, Hf_i and ϵHf values in the range *ca.* 2000–2200 Ma are similarly of a more radiogenic nature. Unfortunately, there is currently no Hf-isotope data available from Reynolds Package detrital zircon grains for comparison with the Aileron Metamorphics.

Bivariate plots of $^{176}(\text{Lu}, \text{Yb})/^{177}\text{Hf}$ versus age are shown in Figure 6.2. In both instances the $^{176}(\text{Lu}, \text{Yb})/^{177}\text{Hf}$ ratio shows a steadily increasing range of values with decreasing age. These data do not refine the discrimination of sub-populations in the data.

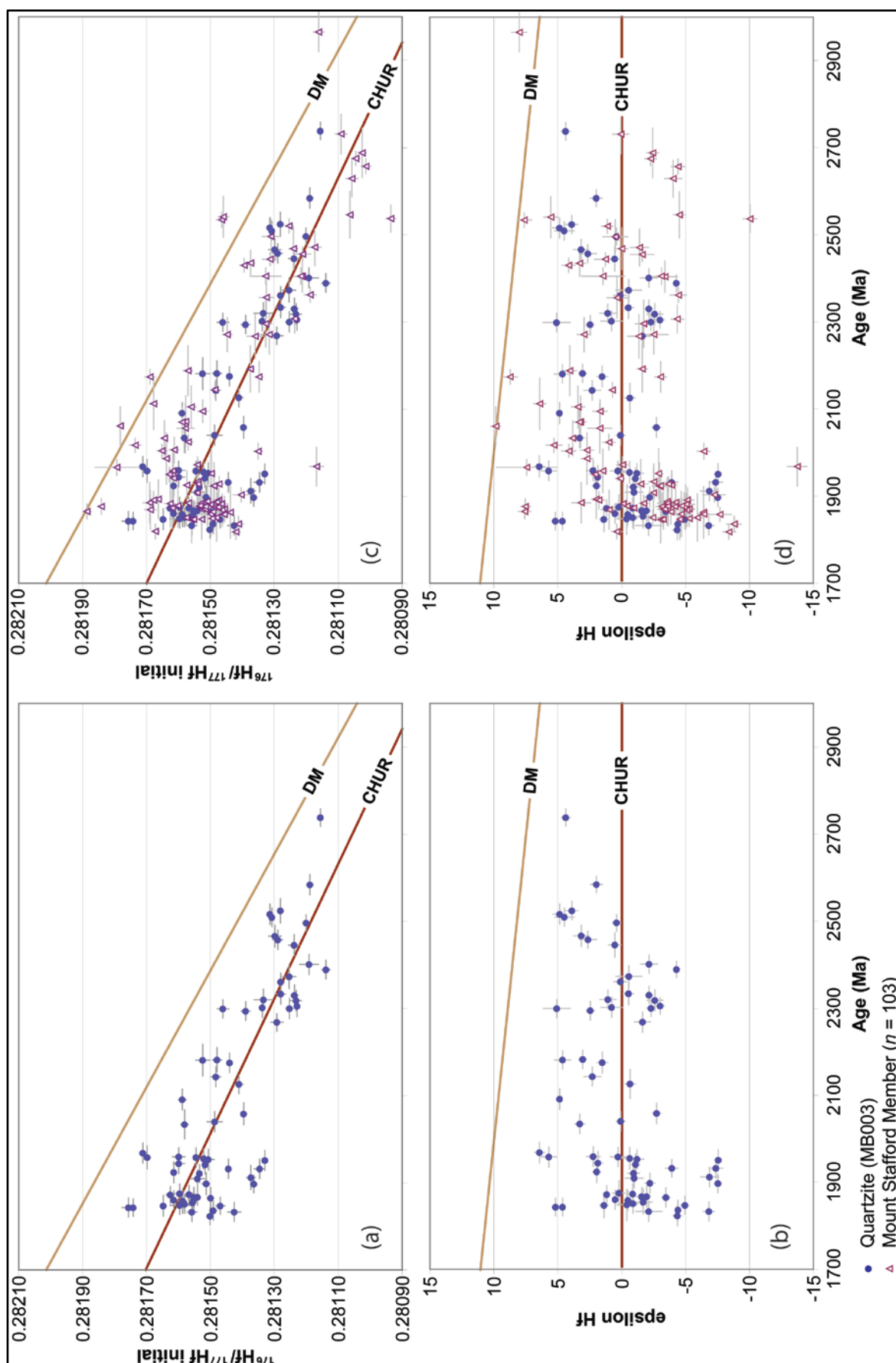


Figure 6.1 Caption continues onto following page.

Figure 6.1 Initial Hf (a) and epsilon Hf (b) values measured in sample MB003 versus age. Shown again with initial Hf (c) and epsilon Hf (d) values measured in detrital zircon from the Mount Stafford Member (Lander Package equivalent; unpublished data provided by E. Dunkley, 2013). Error bars are 1σ .

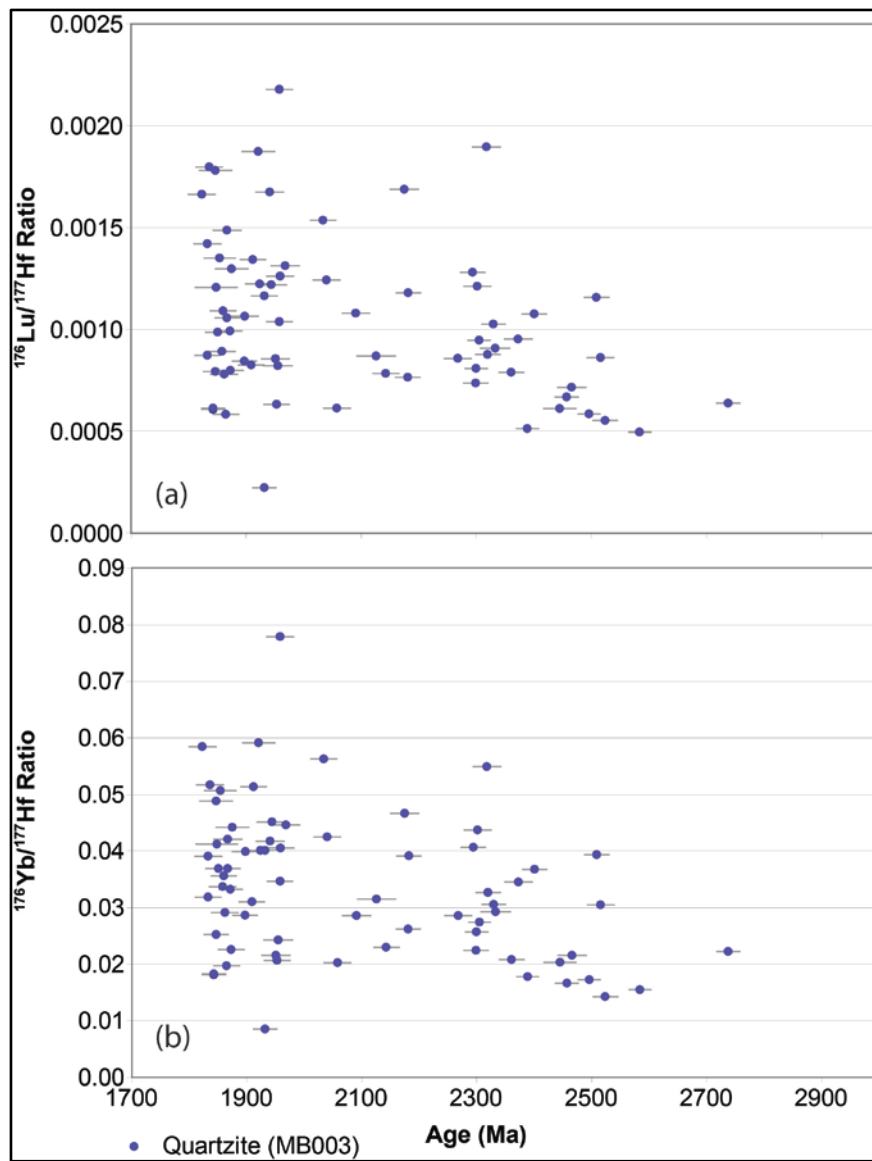


Figure 6.2 Bivariate plot of (a) $^{176}\text{Lu}/^{177}\text{Hf}$ and (b) $^{176}\text{Yb}/^{177}\text{Hf}$ versus age for sample MB003 zircon grains. Error bars are 1σ .

6.3.2 Magmatic Zircon Hf Isotopes—Boothby Orthogneiss (MB007)

A total of 51 analyses were conducted on 48 zircon grains from orthogneiss sample MB007. Three analyses with short ablations were re-analysed on similarly zoned domains within the crystal to acquire a satisfactory signal. Analyses with lower limit uncertainties <1846 Ma (inferred magmatic; $n = 36$) produce a continuum of Hf_i values from 0.281416 to 0.281720. Most extend from CHUR towards crustal values, although a minor component extends towards the DM evolution line. Analyses with lower limit uncertainties <1873 Ma plot within the range of magmatic Hf_i values, although one plots away from the main population at 0.281356 where it overlaps Hf_i values of the quartzite sample (Figure 6.3c). Inherited grains with lower limit uncertainties ≥ 1873 Ma ($n = 8$) show the greatest spread in Hf_i values and generally plot above CHUR (Figure 6.3). A model evolution curve typical of continental crust ($^{176}\text{Lu}/^{177}\text{Hf}$ ratio of 0.015), fitted through the middle of the inferred magmatic population, intersects the depleted mantle growth curve at 2.6 Ga.

Epsilon Hf values range from -8.91 to 8.15 (Figure 6.3b). Magmatic zircon grains range from -7.60 to 2.95, with analyses <1873 Ma showing negative ϵHf values within this range. Older inherited grains ($n = 8$) record a wider range of ϵHf values from -8.91 to 8.15, though generally plotting above CHUR (Figure 6.3b).

In Figure 6.3c and d, Hf-isotope compositions from sample MB007 are shown with those measured in the quartzite sample as well as magmatic zircon grains from the eastern Mount Stafford Granite (eastern granite); the type locality for Stafford Event magmatism in the Reynolds–Anmatjira ranges (unpublished data; Farrow, 2012). The eastern granite produces Hf_i values from 0.281420 to 0.281691 that are indistinguishable from those observed in the Boothby Orthogneiss (Figure 6.3c). It is also apparent that near crystallisation age detrital zircon grains from the quartzite sample share similar Hf-isotopic compositions with both the eastern granite and Boothby Orthogneiss. Considering $^{176}(\text{Lu}, \text{Yb})/^{177}\text{Hf}$ versus age provides no distinction between magmatic zircon grains and detrital zircon grains from the quartzite, with both showing a similar range in values (Figure 6.4)

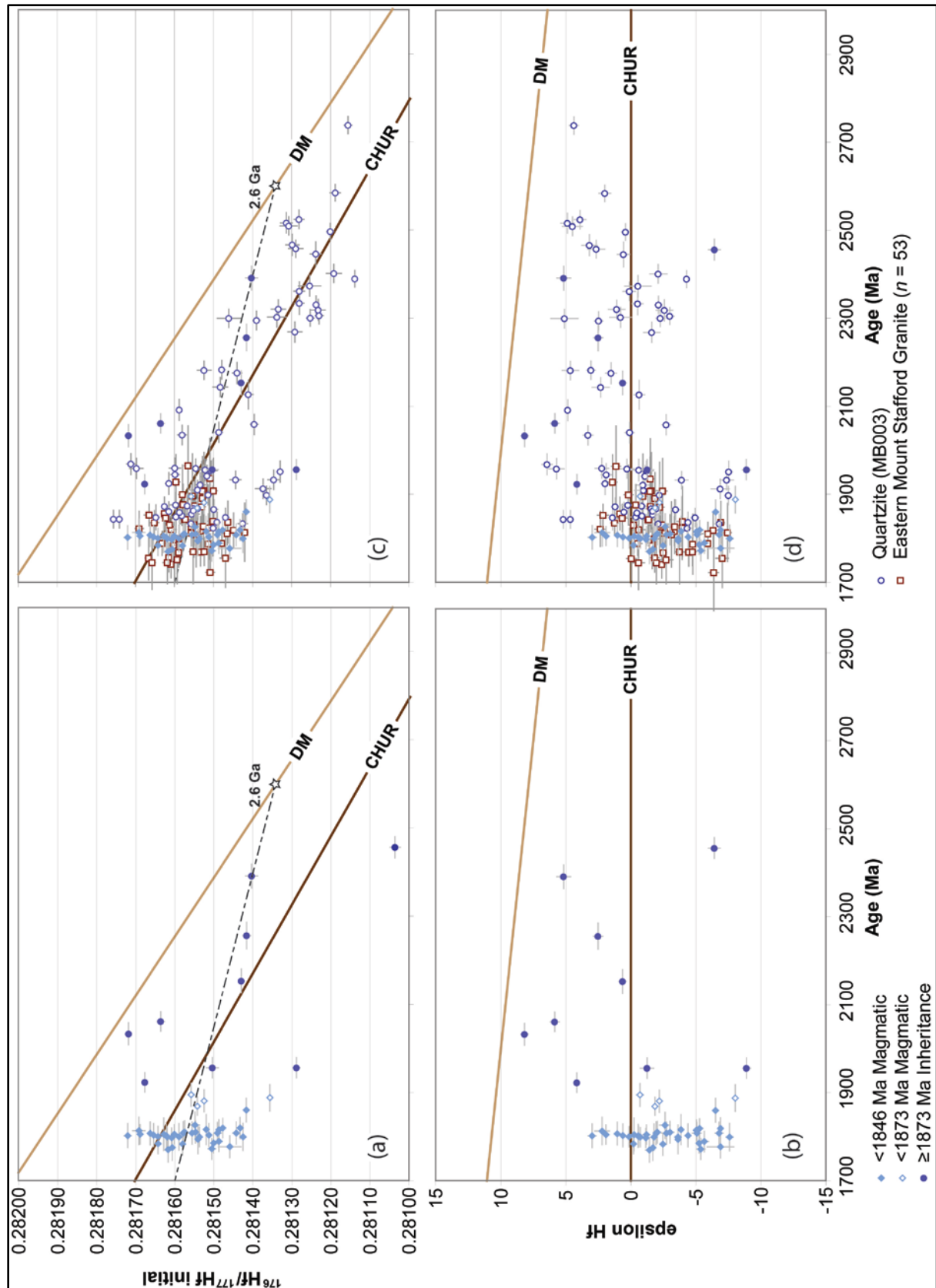


Figure 6.3 Initial Hf (a) and epsilon Hf (b) values measured in sample MB007 versus age. Shown again with initial Hf (c) and epsilon Hf (d) values measured in detrital zircon from sample MB003. Dashed line depicts the modelled evolution of typical continental crust using a $^{176}\text{Lu}/^{177}\text{Hf}$ ratio of 0.015. Error bars are 1σ .

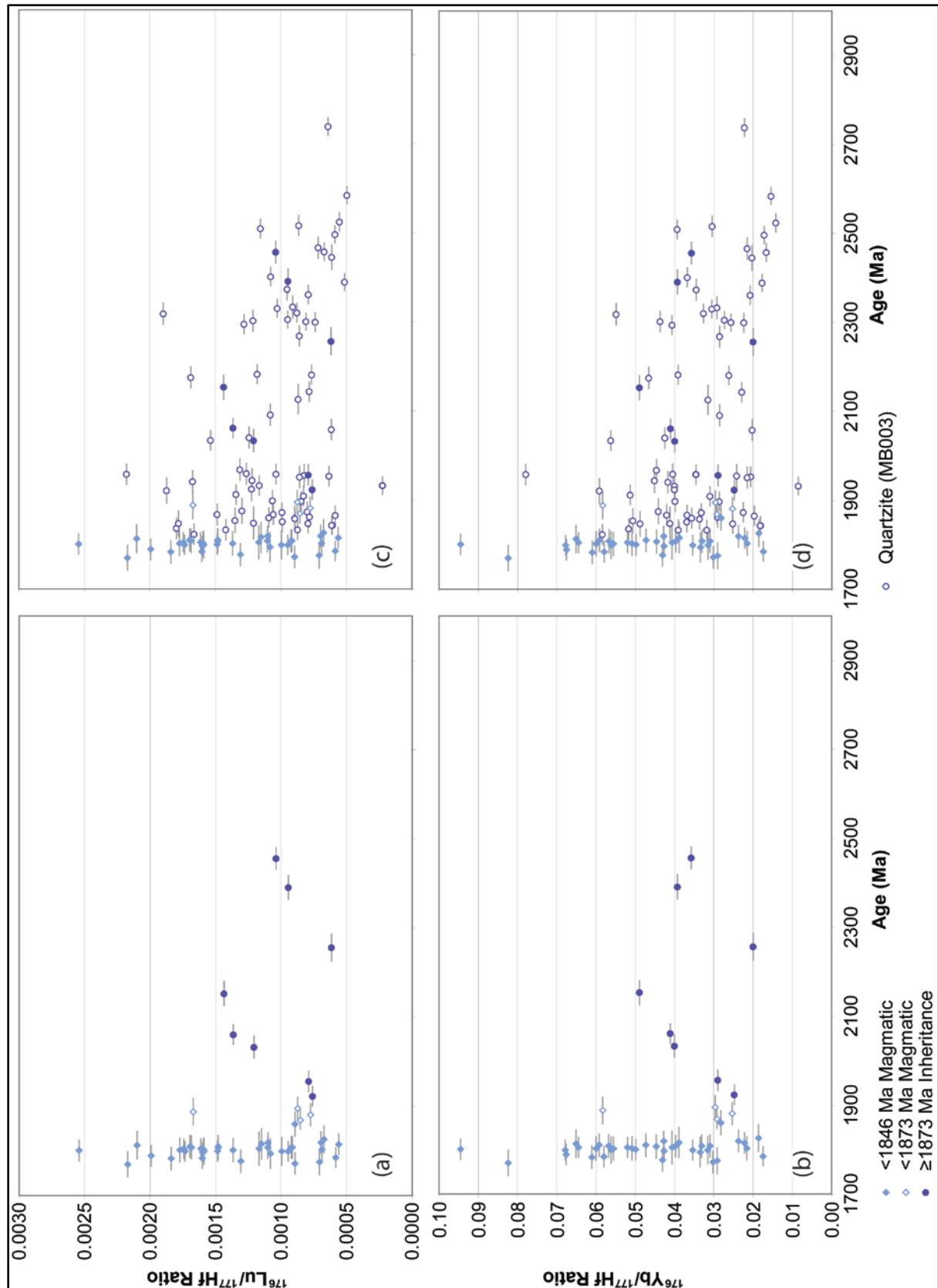


Figure 6.4 Bivariate plot of (a) $^{176}\text{Lu}/^{177}\text{Hf}$ and (b) $^{176}\text{Yb}/^{177}\text{Hf}$ versus age for sample MB007 zircon. Shown again with (c) $^{176}\text{Lu}/^{177}\text{Hf}$ and (d) $^{176}\text{Yb}/^{177}\text{Hf}$ values measured in detrital zircon from sample MB003. Error bars are 1σ .

6.3.3 Metamorphic Zircon Hf Isotopes—Diatexite (MB033)

Due to instrument operational error, only a small sample size (15 analyses) was confidently acquired from sample MB033. Low-response rim domains ($n = 9$) produce Hf_i values plotting below CHUR in the range 0.281755 to 0.281570, with concordant and discordant subpopulations showing some overlap within this range (Figure 6.5a, b). Analyses of core domains ($n = 6$) produce scattered Hf_i values between 0.281198 and 0.281591 and generally falling below CHUR (Figure 6.5a, b).

When a best-fit model evolution curve typical of continental crust ($^{176}\text{Lu}/^{177}\text{Hf}$ ratio of 0.015) is positioned through the data, low-response rim domains lie along evolution from core domains (Figure 6.5a). This relationship is further demonstrated when considered with the Hf_i values from quartzite sample MB003 (Figure 6.5c). However, Hf_i values observed in low-response rim domains similarly lie along the predicted path of detrital zircon grains experiencing Pb-loss (Figure 6.5c).

Considering $^{176}(\text{Lu}, \text{Yb})/^{177}\text{Hf}$ versus age, low-response rim domains are varied with no obvious trends between concordant and discordant sub-populations. Low-response rim domains generally sit slightly higher than the majority of core domains (Figure 6.6a, b), although when these data are considered with values from the quartzite sample this distinction is less apparent (Figure 6.6c, d). A strong correlation exists between core domains and the quartzite sample.

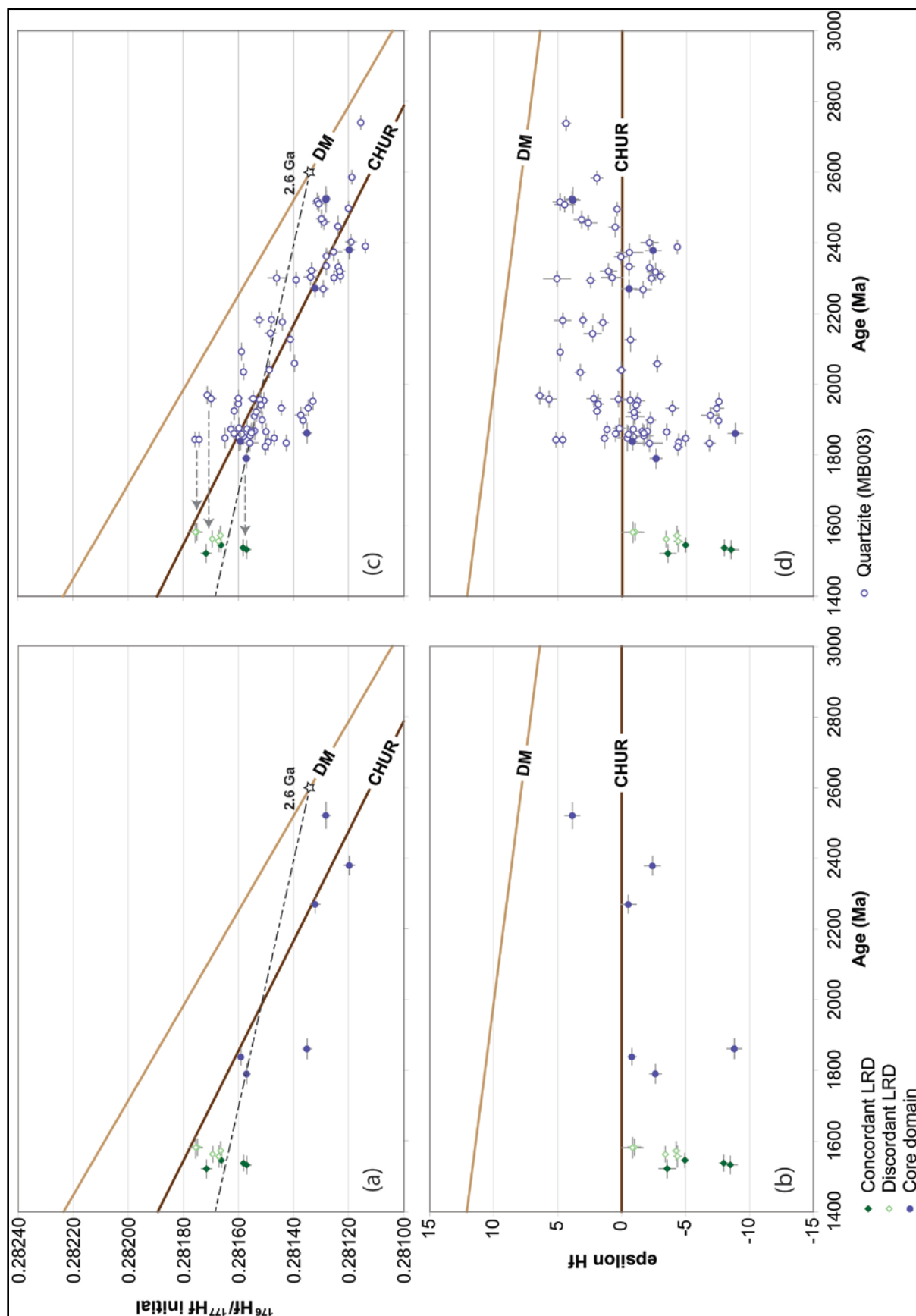


Figure 6.5 Caption continues onto following page.

Figure 6.5 Initial Hf (a) and epsilon Hf (b) values measured in sample MB033 versus age. Shown again with initial Hf (c) and epsilon Hf (d) values measured in detrital zircon from sample MB003. Black dashed line depicts the modelled evolution of typical continental crust using a $^{176}\text{Lu}/^{177}\text{Hf}$ ratio of 0.015. Grey dashed lines indicate the expected paths of detrital zircon grains experiencing Pb-loss during the Chewings Orogeny. Error bars are 1σ .

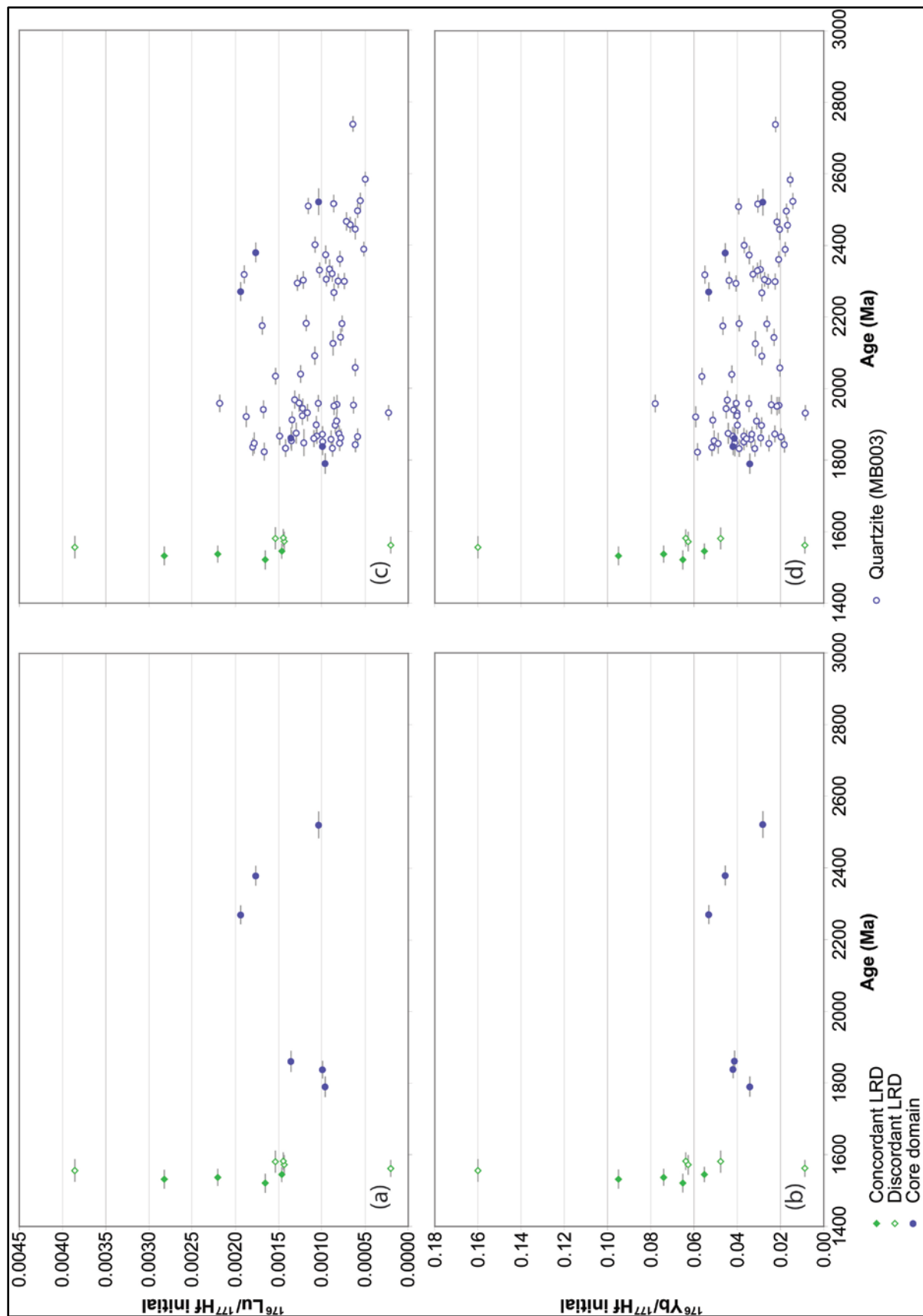


Figure 6.6 Caption continues onto following page.

Figure 6.6 Bivariate plot of (a) $^{176}\text{Lu}/^{177}\text{Hf}$ and (b) $^{176}\text{Yb}/^{177}\text{Hf}$ versus age for sample MB033 zircon. Shown again with (c) $^{176}\text{Lu}/^{177}\text{Hf}$ and (d) $^{176}\text{Yb}/^{177}\text{Hf}$ values measured in detrital zircon from sample MB003. Error bars are 1σ .

6.7 DISCUSSION

6.7.1 Detrital Zircon Hf Isotopes—Quartzite (MB003)

Detrital zircon grains from sample MB003 have diverse Hf-isotopic compositions, consistent with derivation from varied crystalline rocks. The distribution of Hf-isotope versus age data in the quartzite closely equates to the Lander Package equivalents at Mount Stafford. These data are consistent with both units receiving detritus from the same ultimate protosources. The detrital zircon grains from the Mount Stafford Member comprise some extreme values that may be an artefact of relative sample size (Mount Stafford Member $n = 103$; Aileron Metamorphics $n = 69$). Alternatively, this could represent subtle geological variation within the wider depositional system. The latter interpretation is not unreasonable given these samples are geographically separated by some 90 km and their relative stratigraphic levels within the Lander Package is unknown.

A common feature of the Lander Package is the predominance of radiogenic Hf-isotope compositions in the range 2000 to 2200 Ma, consistent with a greater proportion of depleted mantle sources being involved in crustal production at this time. However, the dominant age population in the Lander Package (*ca.* 1864 Ma) comprises zircon grains with very diverse Hf-isotope compositions.

6.7.2 Magmatic Zircon Hf Isotopes—Boothby Orthogneiss (MB007)

Chapter 5 concluded that near crystallisation age inheritance is indistinguishable from magmatic zircon growth on the basis of size, shape, CL imagery, minor element composition and age. Hf-isotope compositions also do not distinguish these two components.

The easily distinguished inherited zircon grains (>1873 Ma) have Hf-isotope compositions that correlate with the quartzite sample. This is consistent with inheritance of Lander Package detrital zircon during (i) assimilation at the source or (ii) emplacement level contamination.

Magmatic zircon analysed from the orthogneiss sample show significant variation of ϵ_{Hf} values from -7.7 to 2.95, suggesting they crystallised from a heterogeneous Hf reservoir around the same time. Although this was dominated by crustal-derived material, positive ϵ_{Hf} values indicate lesser contributions of mantle-derived components in local granitoid production. However, given the difficulties in distinguishing near-crystallisation age inheritance from magmatic zircon growth (Chapter 5), it is plausible that some, or possibly all positive ϵ_{Hf} values observed in sample MB007 are in fact inherited detrital zircon incorporated into the ascending magma. This interpretation would invoke a dominantly crustal origin for the Boothby Orthogneiss, possibly reflecting partial

melting of deeper Lander Package sedimentary rocks. This interpretation conforms to the model proposed by Collins & Vernon (1991) in which Stafford Event granitoid magmas are generated by partial melting of the lower crust in response to mantle perturbations. Regardless of how positive ϵ_{Hf} values are interpreted, the predominance of negative ϵ_{Hf} values indicates significant contributions of recycled crustal material in local magma production, which is consistent with the strongly S-type character of Stafford Event granitoids in the Reynolds–Anmatjira ranges (Collins & Williams, 1995).

Magmatic zircon from the Boothby Orthogneiss show a near-identical range of Hf-isotopic compositions to the eastern Mount Stafford Granite suggesting both granites were generated from partial melting of similar source rocks. This provides further support for correlation of the Boothby Orthogneiss with the Stafford Event and suggests the Hf-isotopic composition of these granitoids may be characteristic of Stafford Event magmatism in the region.

$^{176}\text{Hf}/^{177}\text{Hf}$ ratio analysis provides no further resolution between near-crystallisation age inheritance and magmatic zircon in the Boothby Orthogneiss, with detrital grains from the quartzite covering a similar range of values.

6.7.3 Metamorphic Zircon Hf Isotopes—Diatexite (MB033)

Although relatively few grains were confidently analysed, geologically significant trends are discernable in both low-response rim, and core domains from sample MB033 zircon. Core domains share near-identical Hf-isotope compositions with detrital grains from the quartzite. This complements observations made in Chapter 5 regarding grain size and geochronological similarities between these populations and is consistent with inheritance of Lander Package detrital zircon during diatexite production, migration and/or emplacement.

Though low-response rim domain zircon in sample MB033 has (within both concordant and discordant populations) Hf_i values following a typical continental crust Lu/Hf evolution curve, these data may also be explained by recrystallization of detrital grains as suggested by the ghost zoning observed in some grains (Chapter 5). Hoskin & Black (2000) showed that there is differential exsolution of the REE from the crystal lattice during solid-state recrystallisation. Light rare earth elements are preferentially expelled over the smaller HREEs, which renders the Lu–Hf isotopic system undisturbed, preserving the original Hf_i composition of the protolith zircon (Hoskin & Black, 2000). This phenomenon would explain the variation in Hf_i values observed in low-response rim domains. However, a mix of both new zircon growth and recrystallization of detrital zircon can not be ruled out as many low-response rim domains do not preserve ghost zoning and the less radiogenic values seen in detrital grains are not represented. A larger data set may favour one mechanism as dominant over the other.

7. DISCUSSION & CONCLUSIONS

The combination of structural and petrographic observation with isotopic analysis of zircon has determined a complex evolution of the Aileron Metamorphics. This chapter is a synthesis of the preceding chapters. It will discuss the relationships between the individual data sets and build toward the conclusions. The discussion is built around topics related to the aims set out in the introductory chapter (section 1.4).

7.1 TIMING RELATIONSHIPS & FABRIC DEVELOPMENT

On the basis of field observations including a lack of S1 in the Boothby Orthogneiss, the D1 deformation event is interpreted to have occurred prior to emplacement of the Stafford Event granites. This relationship suggests a significant lapse in time between D1, and D2–D3 (*ca.* 200 million years). Despite the significant implied temporal distinction between these events a strong coincidence of metamorphic grade exists between them. High-strain tectonic fabric development is not pervasively associated with the Stafford Event in the Mount Stafford area (Hand & Buick, 2001). It is plausible that strain was not homogeneous during the Stafford Event, explaining the difference between the interpretation made here and the low strain nature of the Stafford Event at Mount Stafford. However, these relationships question the initial interpretation which hinges on the comparison of fabrics developed in rheologically heterogeneous (bedded) paragneiss with those developed in a rheologically homogeneous body of orthogneiss. Rheological contrasts considered in chapter 3 may be important in resolving the timing of D1. In light of the petrographic observations indicating igneous microstructures are preserved in orthogneiss, alternative interpretations need to be considered. It is possible that rheological contrasts between the two primary rock-types in the field may have inhibited, development of S1 in the orthogneiss, in which case D1–D3 belong to the Chewings Orogeny. Alternatively, the orientations of the D1 and D2 deformation mechanisms are essentially the same, so it is possible that the homogeneous nature of the orthogneiss outcrop has allowed S1 to be concealed by S2, which is only evident in the paragneiss outcrop due to the heterogeneous nature (*i.e.* bedded). Further research is warranted into the absolute timing of high fabric development. This might be achieved via *in-situ* dating of monazite or zircon in high-grade paragneiss.

7.2 MAXIMUM AGE OF SEDIMENT DEPOSITION & CORRELATIONS

The maximum age of deposition determined in this study used two approaches. The youngest coherent population of detrital zircon ages limits the maximum age of deposition to after 1873 Ma, whereas the youngest individual detrital grain reduces this to 1846 Ma. However, chapter 5 shows that the detrital zircon age spectra is not always distinct when comparing Lander and Reynolds package rocks. The additional information provided by the Hf-isotope analysis of zircon did not help resolve the correlation of the Aileron Metamorphics with either Lander or Reynolds package, as no data currently exist for Reynolds Package rocks and the similar proto-source of the two packages or recycling of Lander into Reynolds sediment makes the correlation of metasedimentary rocks fraught. The data do confirm that the Aileron Metamorphics are not an exotic block.

7.3 GRANITOID EMPLACEMENT

The Boothby Orthogneiss contains zircon younger than the detrital grains in the Aileron Metamorphics consistent with magmatic zircon growth. However, the age range of the detrital grains in the country rock spread down to and overlap the age estimate of the granitoid, indicating magmatism shortly followed deposition of the protolith to the Aileron Metamorphics. The inferred inherited grains share many similarities with the detrital grains characterised from the Aileron Metamorphics, consistent with emplacement level contamination or similar age rocks in the source region. The characteristics of the magmatic and inherited zircon overlap, including morphology, colour, CL-intensity and pattern, trace element composition, U–Pb age and Hf-isotope character. None of the data sets presented in chapters 5 or 6 could distinguish the near crystallisation age inheritance in the Boothby Orthogneiss. The preferred age determination of 1801 ± 8 Ma possibly includes minor inheritance suggesting this age is a maximum. Regardless of the inability to exclude all inherited grains, the orthogneiss is Stafford Event. In comparison, U–Pb and Hf-isotope characteristics of the zircon in the Boothby Orthogneiss are remarkably similar to those determined for granitoids at Mount Stafford (Chapter 6).

7.4 TIMING OF METAMORPHISM

Several lines of evidence documented in this thesis indicate a prolonged thermal perturbation outlasting pervasive deformation in the Mount Boothby area. In the field, partial melting of both sedimentary and igneous protoliths produced leucosome that cuts the main structural gneissosity. Similarly, petrographic analysis has shown that D1–D3 structures are commonly overprinted by a high-grade static recrystallisation event and in one instance was accompanied by partial melting and diatextite development.

U–Pb geochronology of low-response rim domains of zircon separated from diatextite produces two metamorphic age populations. The high concordance of the younger population may reflect the static conditions inferred during recrystallisation, which is likely to be in contrast to the dynamothermal regime prevailing during the early stages of the Chewings Orogeny. Pb-loss in the older population may be a function of the strain of these grains during D1–D3 deformation.

The duration of LPHT metamorphic conditions accompanying the Chewings Orogeny is currently estimated at 26 ± 3 million years (Williams *et al.*, 1996). However metamorphic zircon dating from tectonically late diatextite leucosome in this study suggests high temperature conditions associated with this event continued for up to 63 ± 7 million years. Such extended periods of high temperature metamorphism are uncommon and a mechanism capable of producing such a phenomenon is unlikely to exist under a solely crustal heat regime as suggested by Hand *et al.* (1995) and Hand & Buick (2001). Input from mantle heating is likely however this would invoke a thinning of the crust which is not recorded in the structural style of the terrane (dominated by compressional tectonics).

7.5 CONCLUSIONS

In response to the aims outlined at the beginning of this thesis, the following conclusions are made:

- Establish a relative timing of events using field relationships complimented by microstructural analysis of overprinting tectonic fabrics.
 - *Protolith sedimentary rocks of the Aileron Metamorphics were deposited in a turbidite-style depositional system. Following lithification, the sedimentary pile was deformed in response to N–S directed shortening (D1) before emplacement of the Boothby Orthogneiss protolith granitoid. Both rock types subsequently underwent deformation in response to NNE–SSW and NW–SE directed compression during D2 and D3. D4 deformation overprints all earlier fabrics in both sedimentary and igneous protoliths.*
- Determine the metamorphic grade of each tectonic fabric.
 - *D1–D3 deformation occurred above the sillimanite isograd under granulite facies conditions. D4 deformation occurred at upper greenschist–amphibolite facies conditions.*
- Compare and contrast the detrital zircon age distributions and (where possible) the Hf isotope geochemistry of the Aileron Metamorphics with those of the Lander and Reynolds packages.
 - *Similar detrital zircon age populations observed in the Aileron Metamorphics are present in both Lander and Reynolds Package probability density distributions. Available Hf-isotope data shows detritus of the Aileron Metamorphics and Lander Package share isotopically similar*

source regions. The detrital zircon age spectra alone do not distinguish Lander from Reynolds packages.

- Establish the emplacement age of the Boothby Orthogneiss, which envelopes the Aileron Metamorphics in the Mount Boothby area.
 - *The granitoid precursor of the Boothby Orthogneiss intruded the Aileron Metamorphics at 1801 ± 8 Ma during the 1810–1800 Ma Stafford Event. This intrusive relationship of the Boothby Orthogneiss with the Aileron Metamorphics dictates they are high-grade Lander Package equivalents.*
- Constrain the timing of granulite facies metamorphism in the area and the implications this has for the relative timing of fabric development.
 - *LPHT metamorphism coeval with the onset of the intra-cratonic Chewings Orogeny at ca. 1590 Ma. Geochronological evidence in this study indicates these conditions persisted for 63 ± 7 million years, some 37 ± 7 million years longer than previous estimates, finally cooling below the solidus at 1531 ± 3 Ma on the basis of the crystallisation age of the post-D3 diatexite. D2 and D3 are post- 1801 ± 8 Ma and pre- 1531 ± 3 Ma, most likely Chewings Orogeny (1590–1530 Ma).*

Due to the discontinuous geographical distribution of outcrops mapped as Aileron Metamorphics (Figure 1.1), the findings of this study are restricted to outcrops in the Mount Boothby area.

8. LIMITATIONS & FUTURE RESEARCH OPPORTUNITIES

As with many detrital zircon studies, the single most limiting factor is the number of zircon grains analysed. In this study the number of zircon grains analysed was restricted by the number of grains mounted with sufficient surface area and continuous internal zoning for analysis, given the minimum spot size the laser beam (30 μm). Furthermore, wider sampling may have provided a more comprehensive and more statistically reliable probability density distribution of the Aileron Metamorphics (again improving sample size).

This study has demonstrated the difficulty in distinguishing near-crystallisation age inheritance from new magmatic growth in S-type granites and the challenge this presents to accurate age estimation. Jeon *et al.* (2012) have shown *in-situ* O-isotope fingerprinting of zircon populations to be an effective tool for discriminating inheritance from similarly aged magmatic zircon in S-type monzogranites of the Bundarra Supersuite, New England Orogen, eastern Australia. Due to financial and logistical constraints this technique was not employed in this study. Applying this technique to zircon from the Boothby Orthogneiss may allow inherited zircon grains to be identified and ultimately provide greater resolution of the crystallisation age. This technique may also prove beneficial to geochronological investigations of granitoid rocks occurring elsewhere in the Reynolds–Anmatjira ranges.

Perhaps the most significant outcome of the study has been the re-evaluation of the duration of LPHT metamorphic conditions during the Chewings Orogeny in the SE Reynolds Range. Further research is required to define the mechanisms responsible for sustaining high-grade metamorphic conditions in the region under largely compressional tectonics and in the apparent absence of Chewings Orogeny aged mantle input to the thermal regime.

Boothby Orthogneiss in the study area locally preserves evidence of partial melting in the way of garnet-bearing leucosome overprinting the regional S2 gneissosity. Garnet-bearing dykes also cut the S2 gneissosity. An avenue of further study could involve investigation of the distribution of rare-earth elements between the garnet-bearing leucosome and proximal foliation assemblage to better understand the melting process. In addition, rare earth patterns of garnet in the orthogneiss could be compared to those of garnet in the dykes.

Finally, the relationship of the Nolans Dam Metamorphics to the regional stratigraphic framework remains unconstrained by modern geochronological methods. Successful correlation of the Aileron Metamorphics as high-grade Lander Package equivalents in this study suggests a similar approach may be equally successful when applied to this unit.

REFERENCES

- ANDERSEN T. 2002. Correction of common lead in U–Pb analyses that do not report ^{204}Pb . *Chemical Geology*. **192**, 59–79.
- BLACK L.P. & GULSON B.L. 1978. The age of the Mud Tank Carbonatite, Strangways Range, Northern Territory. *BMR Journal of Australian Geology & Geophysics*. **3**, 227–232.
- BUICK I.S., CARTWRIGHT I., HAND M. & POWELL R. 1994. Evidence for pre-regional metamorphic fluid infiltration of the Lower Calcsilicate Unit, Reynolds Range Group (central Australia). *Journal of Metamorphic Geology*. **12**, 789–810.
- BUICK I.S., HAND M., VRY J.K., CARTWRIGHT I. & READ C.M. 1999. Polymetamorphism and reactivation of the Reynolds Range area, northern Arunta Inlier, central Australia: petrological, geochronological, geochemical and structural constraints. *SGGMP Fieldguide No 2*, Geological Society of Australia.
- BUICK I.S., MILLER J.A., WILLIAMS I.S. & CARTWRIGHT I. 2001. Ordovician high-grade metamorphism of a newly recognized late Neoproterozoic terrane in the northern Harts Range, central Australia. *Journal of Metamorphic Geology*. **19**(4), 373–394.
- BURKHARD M. 1993. Calcite twins, their geometry, appearance and significance as stress–strain markers and indicators of tectonic regime: a review. *Journal of Structural Geology*. **15**, 351–368.
- CAWOOD P.A. & KORSCH R.J. 2008. Assembling Australia: Proterozoic building of a continent. *Precambrian Research*. **116**, 1–38.
- CARTWRIGHT I., BUICK I.S., FOSTER D.A. & LAMBERT D.D. 1999. Alice Springs age shear zones from the southeastern Reynolds Range, central Australia. *Australian Journal of Earth Sciences*. **46**, 355–363.
- CLAOUÉ-LONG J. & EDGOOSE C. 2008. The age and significance of the Ngadarunga Granite in Proterozoic central Australia. *Precambrian Research*. **166**, 219–229.
- CLAOUÉ-LONG J., EDGOOSE C. & WORDEN K. 2008. A correlation of Aileron Province stratigraphy in central Australia. *Precambrian Research*. **166**, 230–245.
- CLAOUÉ-LONG J. & HOATSON D.M. 2005. Proterozoic mafic–ultramafic intrusions in the Arunta Region, central Australia. *Precambrian Research*. **142**, 134–158.
- CLARKE G.L. & POWELL R. 1991. Proterozoic granulite facies metamorphism in the southeastern Reynolds Range, central Australia: geological context, P–T path and overprinting relationships. *Journal of Metamorphic Geology*. **9**, 267–281.
- CLOSE D., SCRIMGEOUR I., EDGOOSE C., CROSS A., CLAOUÉ-LONG J., KINNY P. & MEIXNER T. 2003.

- Redefining the Warumpi Province. Annual Geoscience Exploration Seminar (AGES) 2003, Record of Abstracts. *Northern Territory Geological Survey Record*, **2003-001**.
- COLLINS W.J. & TEYSSIER C. 1989. Crustal scale ductile fault systems in the Arunta inlier, central Australia. *Tectonophysics*. **158**, 49–66.
- COLLINS W.J. & VERNON R.H. 1991. Orogeny associated with anticlockwise P - T - t paths: Evidence from low- P , high- T metamorphic terranes in the Arunta inlier, central Australia. *GEOLOGY*. **19**, 835–838.
- COLLINS W.J. & SHAW R.D. 1995. Geochronological constraints on orogenic events in the Arunta Inlier: a review. *Precambrian Research*. **71**, 315–346.
- COLLINS W.J. & WILLIAMS I.S. 1995. SHRIMP ionprobe dating of short-lived Proterozoic tectonic cycles in the northern Arunta Inlier, central Australia. *Precambrian Research*. **71**, 69–89.
- COLLINS W.J., VERNON R.H. & CLARKE G.L. 1991. Discrete Proterozoic structural terranes associated with low- P , high- T metamorphism, Anmatjira Range, Arunta Inlier, central Australia: tectonic implications. *Journal of Structural Geology*. **13**, 1157–1171.
- CORFU F., HANCHAR J.M., HOSKIN P.W.O. & KINNY P.D. 2003. Atlas of Zircon Textures. In: HANCHAR J.M. & HOSKIN P.W.O. (eds), *Zircon. Reviews in Mineralogy & Geochemistry*. **53**, 469–500.
- DAVIS D.W., WILLIAMS I.S. & KROGH T.E. 2003. Historical development of zircon geochronology. In: HANCHAR J.M. & HOSKIN P.W.O. (eds), *Zircon. Reviews in Mineralogy & Geochemistry*. **53**, 145–181.
- DICKINSON W.R. & GEHRELS G.E. 2009. Use of U–Pb ages of detrital zircons to infer maximum depositional ages of strata: A test against a Colorado Plateau Mesozoic database. *Earth and Planetary Science Letters*. **288**, 115–125.
- DIRKS P.H.G.M. 1990. Intertidal and subtidal sedimentation during a mid-Proterozoic marine transgression, Reynolds Range Group, Arunta Block, central Australia. *Australian Journal of Earth Sciences*. **37**, 409–422.
- DIRKS P.H.G.M. & WILSON C.J.L. 1990. The geological evolution of the Reynolds Range, central Australia: evidence for three distinct structural–metamorphic cycles. *Journal of Structural Geology*. **12(5/6)**, 651–665.
- DIRKS P.H.G.M., HAND M. & POWELL R. 1991. The P - T -deformation path for a mid-Proterozoic, low-pressure terrane: the Reynolds Range, central Australia. *Journal of Metamorphic Geology*. **9**, 641–661.
- FARROW K. 2012. *Petrographic & Geochronological Investigation of S-Type Granites from a Low-Pressure High-Temperature Regional Aureole: Mt Stafford, Central Australia*. Hons thesis. Macquarie University, Sydney (unpublished).

- FAURE G. & MENSING T.M. 2005. *Isotopes: principals and applications – 3rd Edition*. John Wiley & Sons, Inc. New Jersey.
- FEDO C.M., SIRCOMBE K.N. & RAINBIRD R.H. 2003. Detrital Zircon Analysis of the Sedimentary Record. In: HANCHAR J.M. & HOSKIN P.W.O. (eds), *Zircon. Reviews in Mineralogy & Geochemistry*. **53**, 277–303.
- GALBRAITH R.F. 2005. *Statistics for fission track analysis*. Chapman and Hall/CRC. Interdisciplinary Statistics Series. 224pp.
- GRIFFIN W.L., BELOUSOV E.A. & O'REILLY S.Y. 2007. Crustal history and metallogenic fertility: terrane-scale assessment with detrital zircons. In: MILKEREIT B. (ed), *Proceedings of Exploration 07: Fifth Decennial International Conference on Mineral Exploration*. 311–315. (GEMOC pub **491**).
- GRIFFIN W.L., POWELL W.J., PEARSON N.J., O'REILLY S.Y. 2008. GLITTER: Data reduction software for laser ablation ICP-MS. In SYLVESTER P. (ed.) *Laser Ablation ICP-MS in the Earth Sciences: Current practices and outstanding issues*. Mineralogical Association of Canada, Short Course Series. **40**, 307–311.
- HAND M., BUICK I.S. 2001. Tectonic evolution of the Reynolds–Anmatjira Ranges: a case study in terrane reworking from the Arunta Inlier, central Australia. In MILLER J.A., HOLDSWORTH R.E., BUICK I.S. & HAND M. (eds) *Continental Reactivation and Reworking*. Geological Society, London, Special Publications. **184**, 237–260.
- HAND M., FANNING M. & SANDIFORD M. 1995. Low-P high-T metamorphism and the role of high-heat producing granites in the northern Arunta Inlier. *Geological Society of Australia, Abstracts* **40**, 60–61.
- HALPIN J.A., DACZKO N.R., MILAN L.A. & CLARKE G.L. 2012. Decoding near-concordant U–Pb ages spanning several hundred million years: recrystallisation, metamictisation or diffusion. *Contributions to Mineralogy and Petrology*. **163**, 67–85.
- HARLEY S.L. & KELLY N.M. 2007. Zircon, tiny but timely. *ELEMENTS*. **3**, 13–18.
- HAWKESWORTH C.J. & KEMP A.I.S. 2006. Using hafnium and oxygen isotopes in zircons to unravel the record of crustal evolution. *Chemical Geology*. **226**, 144–162.
- HOSKIN P.W.O. & BLACK L.P. 2000. Metamorphic zircon formation by solid-state recrystallisation of protolith igneous zircon. *Journal of Metamorphic Geology*. **18**, 423–439.
- JACKSON S.E., PEARSON N.J., GRIFFIN W.L. & BELOUSOVA E.A. 2004. The application of laser ablation-inductively coupled plasma-mass spectrometry to in situ U–Pb zircon geochronology. *Chemical Geology*. **211**, 47–69.

- JEON H., WILLIAMS I.S. & CHAPPELL B.W. 2012. Magma to mud to magma: Rapid crustal recycling by Permian granite magmatism near the eastern Gondwana margin. *Earth and Planetary Science Letters*. **319–320**, 104–117.
- JONES III J.V., CONNELLY J.N., KARLSTROM K.E., WILLIAMS M.L. & DOE M.F. 2009. Age, provenance, and tectonic setting of Paleoproterozoic quartzite successions in the southwestern United States. *Geological Society of America Bulletin*. **121(1–2)**, 247–264.
- KINNY P.D. & MAAS R. 2003. Lu–Hf and Sm–Nd isotope systems in zircon. In: HANCHAR J.M. & HOSKIN P.W.O. (eds), *Zircon. Reviews in Mineralogy & Geochemistry*. **53**, 327–342.
- LUDWIG K.R. 2012. Isoplot 3.75, A geochronological toolkit for Microsoft Excel. Berkeley Geochronology Center, Special Publication **No. 5**.
- MAIDMENT D.W., HAND M. & WILLIAMS I. 2002. The extent of Cambrian metasediments and the Ordovician Larapinta Event, eastern Arunta Province, central Australia. In PREISS V.P. (ed) *Expanding Horizons—16th Australian Geological Convention, Adelaide Convention Centre, Adelaide*. Geological Society of Australia Abstracts **67**, p. 180.
- NELSON D.R. 2001. An assessment of the determination of depositional ages for Precambrian clastic sedimentary rocks by U–Pb dating of detrital zircons. *Sedimentary Geology*. **141–142**, 37–60.
- PASSCHIER C.W. & TROUW A.J. 2005. *Microtectonics*. Springer-Verlag, Berlin.
- PIETSCH B. 2001. Towards an Arunta Framework. Annual Geoscience Exploration Seminar (AGES) 2001, Record of Abstracts. *Northern Territory Geological Survey Record*, **2001-006**.
- PHILLIPS G., WILSON C.J.L., CAMPBELL I.H. & ALLEN C.M. 2006. U–Th–Pb detrital geochronology from the southern Prince Charles Mountains, East Antarctica—Defining the Archaean to Neoproterozoic Ruker Province. *Precambrian Research*. **148**, 292–306.
- QIAN Y., SU W., LI Z. & PENG S. 2012. Textural Characterization of Sedimentary Zircon and Its Implication. In YAMAMOTO N. (ed) *Cathodoluminescence*. InTech.
- RUBATTO D., WILLIAMS I.S. & BUICK I.S. 2001. Zircon and monazite response to prograde metamorphism in the Reynolds Range, central Australia. *Contributions to Mineralogy and Petrology*. **140**, 458–468.
- SCRIMGEOUR I. 2003. Developing a revised framework for the Arunta Region. Annual Geoscience Exploration Seminar (AGES) 2003, Record of Abstracts. *Northern Territory Geological Survey Record*, **2003-001**.
- SCRIMGEOUR I. 2004. A revised province definition and Palaeoproterozoic framework for the Arunta Region, central Australia. In MCPHIE J. & MCGOLDRICK P. (eds) *Dynamic Earth: Past, Present and*

- Future—17th Australian Geological Convention, Hobart*. Geological Society of Australia Abstracts **73**, p. 185.
- SCRIMGEOUR I.R., KINNY P.D., CLOSE D.F. & EDGOOSE C.J. 2005. High-T granulites and polymetamorphism in the southern Arunta Region, central Australia: Evidence for a 1.64 Ga accretional event. *Precambrian Research*. **142**, 1–27.
- SCHERER E., MÜNKER C. & MEZGER K. 2001. Calibration of the Lutetium-Hafnium clock. *Science*. **293**, 19–24.
- SCHERER E.E., WHITEHOUSE M.J. & MÜNKER C. 2007. Zircon as a monitor of crustal growth. *ELEMENTS*. **3**, 19–24.
- SHAW R.D., STEWART A.J. & BLACK L.P. 1984. The Arunta Inlier: a complex ensialic mobile belt in central Australia. Part 2: tectonic history. *Australian Journal of Earth Sciences*. **31**, 457–484.
- SHAW R.D. & BLACK L.P. 1991. The history and tectonic implications of the Redbank Thrust Zone, central Australia, based on structural, metamorphic and Rb–Sr isotopic evidence. *Australian Journal of Earth Sciences*. **38**, 307–332.
- SIRCOMBE K.N. & STERN R.A. 2002. An investigation of artificial biasing in detrital zircon U–Pb geochronology due to magnetic separation in sample preparation. *Geochimica et Cosmochimica Acta*. **66(13)**, 2379–2397.
- STEWART A.J., OFFE L.A., GLIKSON A.Y., WARREN R.G. & BLACK L.P. 1980. Geology of the northern Arunta Block, Northern Territory. *BMR Record*. **1980/63**.
- STEWART A.J., OFFE L.A., GLIKSON A.J. & WARREN R.G. 1981. *Geology of the Reynolds Range Region, Northern Territory, Australia. 1:100 000 Special Sheet*. Bureau of Mineral Resources, Geology and Geophysics, Canberra.
- STEWART A.J., SHAW R.D. & BLACK L.P. 1984. The Arunta Inlier: a complex ensialic mobile belt in central Australia. Part 1: stratigraphy, correlations and origin. *Australian Journal of Earth Sciences*. **31**, 445–455.
- SKWARNECKI M. 2004. *Winnecke goldfield, Northern Territory*. CRC LEME, CSIRO Land and Water. Glen Osmond.
- VERMEESCH P. 2004. How many grains are needed for a provenance study? *Earth and Planetary Science Letters*. **224**, 441–451.
- VERMEESCH P. 2012. On the visualisation of detrital age distributions. *Chemical Geology*. **312–313**, 190–194.
- VERNON R.H., CLARKE G.L. & COLLINS W.J. 1990. Mid-crustal granulite facies metamorphism: low-

- pressuremetamorphism and melting, Mount Stafford, central Australia. In ASHWORTH J.R. & BROWN M. (eds) *High temperature Metamorphism and Crustal Anatexis*. Special Publication of the Mineralogical Society. **2**, 272–319.
- VRY J., COMPSTON W. & CARTWRIGHT I. 1996. SHRIMP II dating of zircons and monazites: reassessing the timing of high-grade metamorphism and fluid flow in the Reynolds Range, northern Arunta Block, Australia. *Journal of Metamorphic Geology*. **14**, 335–350.
- WALTER M.R., VEEVERS J.J., CALVER C.R. & GREY K. 1995. Neoproterozoic stratigraphy of the Centralian Superbasin, Australia. *Precambrian Research*. **73**, 173–195.
- WIEDENBECK M., ALLÉ P., CORFU F., GRIFFIN W.L., MEIER M., OBERLI F., VON QUADT A., RODDICK J.C. & SPEILGEL W. 1995. Three natural zircon standards for U-Th-Pb, Lu-Hf, trace element and REE analyses. *Geostandards Newsletter*. **19(1)**, 1–23.
- WILLIAMS I.S., BUICK I.S. & CARTWRIGHT I. 1996. An extended episode of early Mesoproterozoic metamorphic fluid flow in the Reynolds Range, central Australia. *Journal of Metamorphic Geology*. **14**, 29–47.
- WHITNEY D.L. & EVANS B.W. 2010. Abbreviations for names of rock-forming minerals. *American Mineralogist*. **95**, 185–187.
- WOODHEAD, J.D. & HERGT, J.M. 2005. A preliminary appraisal of seven natural zircon reference materials for *in-situ* isotope determination. *Geostandards and Geoanalytical Research*, **29(2)**, 183–195.
- WORDEN K.E., CARSON C.J., CLOSE D.F., DONNELLAN N. & SCRIMGEOUR I.R. 2004. Summary of results. Joint NTGS-GA geochronology project: August 2003–December 2003. *Northern Territory Geological Survey Record*, **2004-004**.
- WORDEN K.E., CARSON C.J., CLOSE D.F., DONNELLAN N. & SCRIMGEOUR I.R. 2008. Summary of results. Joint NTGS-GA geochronology project: Tanami Region, Arunta Region, Pine Creek Orogen and Halls Creek Orogen correlatives, January 2005–March 2007. *Northern Territory Geological Survey Record*, **2008-003**.